

Digital Signal Processing Methods for Pixelated 3-D Position Sensitive Room-Temperature Semiconductor Detectors

by

Yuefeng Zhu

A dissertation submitted in partial fulfillment
of the requirements for the degree of
Doctor of Philosophy
(Nuclear Engineering and Radiological Sciences)
in The University of Michigan
2012

Doctoral Committee:

Professor Zhong He, Chair
Professor Ronald F. Fleming
Professor Thomas H. Zurbuchen
Assistant Research Scientist Feng Zhang

© Yuefeng Zhu 2012

All Rights Reserved

ACKNOWLEDGEMENTS

First, I would like to acknowledge my advisor, Prof. Zhong He, for his patient guidance, inspiring suggestions and continuous support. It's a great opportunity and a previous experience to join his group and learn knowledge from his brilliant mind. Especially, I want to thank him to give me the opportunity to go to the IEEE meeting every year, which is a really helpful way to expand my view of the academic society.

I would like to thank my committee member, Prof. Ronald Fleming, Prof. Thomas Zurbuchen and Dr. Feng Zhang for their instructions and guidance during my PhD research.

I would like to give my gratitude to my colleagues, Dr. Dan Xu, Dr. Steve Anderson, Willy Kaye, Dr. Weiyi Wang, Dr. Christopher Wahl, Miesher Rodrigues and Dr. Dan Lingenfelter for their numerous genius suggestions to my research and the enjoyable life we have experienced together. I want to specially thank Mr. James Berry for his technique support to my experiments.

Last but certainly not least, I would like to express my great appreciation to my parents for their countless sacrifices that make me step to this stage. Though they were not with me in person during the past 6 years of my PhD life, their spiritual support was always around.

TABLE OF CONTENTS

ACKNOWLEDGEMENTS	ii
LIST OF FIGURES	vi
LIST OF APPENDICES	xvi
ABSTRACT	xvii
CHAPTER	
I. Introduction	1
1.1 Room-temperature Semiconductor Detectors	1
1.2 Shockley-Ramo Theory and Weighting Potential	2
1.3 The Development of CdZnTe Detectors	4
1.3.1 Coplanar-grid CdZnTe Detectors	5
1.3.2 3-D Position-sensitive Pixellated CdZnTe Detectors	6
1.4 Summary	10
II. Electronic Noise and Digital Filters	11
2.1 Introduction	11
2.1.1 Electronic Noise	12
2.1.2 Filters	19
2.2 Optimal Filter	22
2.2.1 Optimal Filter for Charge Collecting Signals	22
2.2.2 Optimal Filter for Transient signals	26
2.3 Digital Filter Design	28
2.4 Electronic Noise Correlation and Waveform Fitting	32
2.5 Conclusion	38
III. System Simulation	41
3.1 Introduction	41

3.2	Simulation Software	41
3.2.1	Geant4	41
3.2.2	Maxwell	42
3.3	The Signal Induction	46
3.4	Electronic Noise Simulation	52
3.5	Conclusion	53
IV.	UM-VAD ASIC and its Readout System	54
4.1	Introduction	54
4.2	UM_VAD ASIC	55
4.2.1	Overview	55
4.2.2	Data Acquisition	57
4.2.3	Cell Pedestal Calibration	61
4.2.4	ASIC Performance	62
4.2.5	Special ASIC Functions	67
4.3	Readout System	70
4.3.1	GM-I Readout System	72
4.3.2	DGD-1 Readout System	74
4.4	Common Mode Noise	77
4.5	Conclusion	81
V.	Sub-pixel Position Resolution	82
5.1	Introduction	82
5.2	The Detector System	84
5.3	Sub-pixel Position Calculation Algorithm	84
5.4	Estimate of Sub-pixel Position Resolution by Simulation	88
5.5	Experimental Measurements and Analysis	90
5.5.1	Measured Sub-pixel Position Resolution with Colli- mator	90
5.5.2	Complete Charge Collection Boundary	94
5.6	Sub-pixel Resolution for Two-pixel Events	96
5.7	Performance Improvement with with Sub-pixel Resolution	99
5.7.1	Compton Imaging Improvement	99
5.7.2	Energy Resolution Improvement	102
5.8	Conclusion	109
VI.	Energy and Depth Reconstruction with UM-VAD System	112
6.1	Introduction	112
6.2	Signal Processing	112
6.2.1	Energy Determination	112
6.2.2	Timing Determination	113
6.3	Experimental Results	120

6.3.1	Single-pixel Events	120
6.3.2	Multi-pixel Events	125
6.4	Conclusion	126
VII.	System Response Function and its Applications	127
7.1	Introduction	127
7.2	Generation of System Response Function	129
7.2.1	Charge-collecting Pixels and Cathode	132
7.2.2	Neighboring Pixels	133
7.2.3	Charge Leak Correction and SRFSF Method	138
7.3	Numeric System Response Function Fitting	143
7.4	Application of System Response Function	143
7.4.1	Charge Leak Correction for single-pixel events	143
7.4.2	Electron De-trapping Time Measurement	145
7.5	Conclusion	148
VIII.	Electron Cloud Distribution	150
8.1	Introduction	150
8.2	Electron Cloud Distribution Calculation algorithm	151
8.2.1	Problem Model	151
8.2.2	Solution	152
8.3	Simulation Result	155
8.4	Conclusion	160
	APPENDICES	161
	BIBLIOGRAPHY	167

LIST OF FIGURES

Figure

1.1	An illustration of the signal induction in a planar semiconductor detector.	3
1.2	The pulse height spectra when the energy deposition is fixed. [12] .	3
1.3	Schematic of a ionization chamber with a Frisch grid.	5
1.4	Schematic of a simple coplanar-grid structure. [27]	6
1.5	An illustration of the pixelated CdZnTe detector used in this study.	7
1.6	The raw spectrum and corrected spectrum of ^{137}Cs collected using a Redlen 15-mm thick CdZnTe detector (detector # 4R169) at room temperature. The pixel pitch is 1.72 mm.	8
2.1	An illustration of the charge-sensitive pre-amplifier circuit for semiconductor detectors.	16
2.2	An illustration of noise sources in the charge-sensitive pre-amplifier circuit for semiconductor detectors. In this plot, di_{DL}^2 is detector leakage noise, di_{RD}^2 is detector thermal noise, di_{TL}^2 is FET leakage noise, dv_{TC}^2 is FET channel thermal noise, dv_{TF}^2 is FET 1/f noise and di_{Rf}^2 is the feedback resistor thermal noise, i_D is detector signal, R_D is detector resistance. C_D , C_s and C_A are detector capacitance, circuit distributed capacitance and amplifier input capacitance. C_i can be seen as the total input capacitance to the pre-amplifier. R_f and C_f are feedback resistor and capacitor respectively.	17
2.3	The equivalent circuit for (a) serial noise and (b) parallel noise. In these plots, $dv_s^2 = dv_{TC}^2 + dv_{TF}^2$ and $di_p^2 = di_{DL}^2 + di_{RD}^2 + di_{TL}^2 + di_{Rf}^2$. dv_{so}^2 and dv_{po}^2 are the equivalent output noise of the pre-amplifier. .	18

2.4	An illustration of a CRRC ⁿ filter circuit.	20
2.5	The measured noise amplitude as a function of shaping time using CR-RC ⁴ filter for channel 40 in detector # 3E2 (15×15×10 mm ³ pixlled detector with grid fabricated by eV Product) with the cathode bias at -2500V and the grid bias at -30V. The sampling frequency is 80 MHz and the sampling precision is 12 bit. The data is fitted with a function of $A/t + Bt + C$ to determine the contribution from serial, parallel and 1/f noise.	23
2.6	Serial, parallel and 1/f noise as a function of shaping time for various filters. Shaping time has different meaning for different filters. In this plot, we define shaping time as follows: for CRRC ⁴ filter the shaping time is its time constant; for triangle filter, shaping time is the peaking time; for Gaussian filter, shaping time is the variance of Gaussian function; for trapezoid filter, shaping time is its half width.	24
2.7	Figure of merit for various types of filters when the composition of noise is different. The contribution of 1/f noise is represented by the ratio $C^4/4a^2b^2$. The bigger the ratio is, the more important the 1/f noise component will be.	26
2.8	The signal-to-noise ratio of different shaping filters for: (a) the charge-collecting pixel signal, and (b) the non-collecting pixel transient signal.	28
2.9	The change of the variance suppression factor of the matched-model fitting as a function of the variance ratio α . The noise here is simulated through equation 2.47. The signal waveform is the average signal obtained on a charge collecting pixel in detector # 3E2, which has 160 sample points.	37
2.10	The change of the difference between the mean of two groups ($Var[M_2 - M_1]$) versus the length of the mean m and their spacing k . For different m , the slope of those curves are similar, which matches with the expectation of equation 2.58, indicating the model we used for the noise is correct.	38
2.11	Filter performance for charge-collecting pixel signals. The data is obtained on detector # 3E2 with cathode biased at -2500V and grid biased at -30V.	39
2.12	Filter performance for neighboring pixel transient signals. The data is obtained on detector # 3E2 with cathode biased at -2500V and grid biased at -30V.	39

3.1	This plot shows the Geant4 simulation of the 18-detector array irradiated by a parallel beam of 662 keV.	43
3.2	Accumulated tracks of 20 electrons, which are located in the same position and emitted toward the same direction in each case (perpendicularly downward). The blue lines are from gamma rays and the red lines are the electron track.	44
3.3	Electron cloud size distribution in the energy range from 0 to 3 MeV. This result is obtained from Geant4 simulations. The electron cloud size is defined as the largest distance between any two points in the electron track.	45
3.4	These plots shows the electric field change with the grid bias. The length of the arrow is proportional to the electric field strength and the arrowhead shows the opposite direction of the electric field to illustrate the electron drift path. The light blue rectangle-shaped electrode is the grid, and the green one is the pixel. This result is obtained with a 3-D Maxwell simulation for a $20 \times 20 \times 15 \text{ mm}^3$ CdZnTe detector. The cathode is biased at -3000 V and the grid at -40 V, -50 V, -60 V, -70 V, -80 V, -90 V respectively.	47
3.5	The weighting potential distribution for the center pixel (with a red dot on it). This result is obtained with a 3-D Maxwell simulation for a $20 \times 20 \times 15 \text{ mm}^3$ CdZnTe detector.	48
3.6	Signal induction for a collecting pixel (pixel 22) and its 8 neighbors. The responses correspond to a single simulated 662-keV point electron cloud collected by the center pixel. The transient signals of the neighbor pixels are shown for two events: one occurring underneath the center (thick line) and the other near the edge (dashed line) of the collecting pixel. They both originate in the middle depth of the detector.	50
4.1	The layout of the UM_VAD ASIC.	55

4.2	This figure is an illustration of the ASIC functionality. Each ASIC has 124 channels. Among them, channel 1 is a reference channel for baseline monitoring, channel 2 is grid channel, channel 3 is cathode and channel 4 to channel 124 are anode pixels. Each channel has its own pre-amplifier followed by an anti-aliasing filter and a block of 160 analog buffer cells for sampling and store pre-amplifier output. The output of the pre-amplifier is also routed to another path going through a fast shaper and a comparator to produce clean triggers. The ASIC main clock, which is also the sampling clock, is generated by an external system, which normally is a FPGA. This FPGA monitors the trigger signal from ASIC and determines if a readout sequence needs to be initiated. By assert the ACK control line, the FPGA can start a readout sequence at any time.	58
4.3	The timing diagram of UM_VAD ASIC. The external signals "Clock", "Tout", "ACK", and "DATAout" are shown for a typical operating sequence of the ASIC when an event happens. The acquisition of signals (or "aq"), data readout (or "RO"), and reset are marked. The number of clock cycles shown here is for an illustration. In real operation, it is difference and it changes with the different modes the ASIC is operating in.	60
4.4	Integral (black dots) and differential (blue dots) linearity (the difference between the linear fitting and the measurement) of the VAD_UM ASIC in the ASIC dynamic range measured with the internal test pulser. The linear fitting to the integral linearity is presented as the red line and the 2nd-order polynomial fitting to the differential linearity is presented by the magenta line.	65
4.5	Integral (black dots) and differential (blue dots) linearity (the difference between the linear fitting and the measurement) of the VAD_UM ASIC from 60 keV to 2.6 MeV measured with radiative sources. The linear fitting to the integral linearity is presented as the red line.	66
4.6	The fluctuation of measured baseline. The amplitude is obtained using subtraction method. The data is obtained for channel 40 of detector # 3E2, which is biased at -2500 V on the cathode and -30 V on the grid.	67
4.7	The measured electronic noise changing with the setup. The detector used here is detector # 3E2. V_c and V_g are cathode bias and grid bias respectively. HV board is the cathode bias board. Channel 83 is the pixel that has the best energy resolution. The leakage current on this pixel should be low.	68

4.8	A plot of the GM-I system. As can be seen, the FEC board has detector connectors on it and ASICs bonded on the other side. The espresso board is connected through a HDMI interface to cROB8s data acquisition card and then to a national instrument PCI-DIO-32HS card and finally to a host computer.	73
4.9	the diagram of the DGD-1 system.	76
4.10	The common mode noise measured in the 40 MHz system and the 80 MHz system.	79
4.11	The common mode noise measured in the 80 MHz system with the modification to reduce LFCM noise. The common mode noise is measured when the sampling frequency is set at 1, 1/2, 1/4 and 1/8 ASIC main clock frequency.	80
5.1	The relationship between the opposing-neighboring ratio R_x and real lateral x coordination calculated by simulation. The curve gives R_x as a function of x when the electron cloud is in the middle of a pixel ($y = 0$) and near the cathode surface ($z = 0$). The error bars mark the range of the R_x if the lateral y position and the depth z of the electron cloud change in the pixel volume. The dashed lines mark the boundary of a pixel.	87
5.2	Sub-pixel simulation performance results: (a) the offset difference between the mean calculated position and the true simulated position based on the linear assumption, and (b) the position variation in terms of FWHM due to 4 keV electronic noise. The offset and position variation is plotted for the x coordinate. The error bars mark the offset and FWHM range as the electron cloud position is shifted along y and z directions through the volume of the collecting-pixel column.	88
5.3	The collimator design for experimentally measuring sub-pixel position resolution.	90
5.4	Measured sub-pixel resolution at 662 keV: (a) the mean neighboring pixel ratio for each collimator position. This data is fitted by a linear function and the result shows the slope as $(9.2 \pm 0.5) \times 10^{-4}$ and the interception as 0.072 ± 0.009 with 95% confidence; (b) the FWHM of the position variance at each collimator position. The origin of x axis of these plots are the start location of the collimator instead of the center of the pixel.	91

5.5	The simulated distribution of the electron cloud centroid from a 662-keV gamma-ray source using a collimator. Distribution width is due to the collimator and electron cloud size.	94
5.6	The distribution of single-pixel photopeak events inside a pixel. . . .	95
5.7	Calculated position versus collimator position including a comparison between the simulation and experimental results. The dotted line marks the boundary of the complete charge collection region.	96
5.8	The two cases of the arrangement of the triggered pixels for neighboring pixel events.	98
5.9	Sub-pixel position for the two-pixel events in the collimator experiment. The energy deposition on the neighboring pixels is required to be greater than 100 keV.	100
5.10	The distribution of the displace between the original interaction location and the centroid of the electron cloud. The crossing point of the red lines marks the origin of the interaction. The electrons are emitted toward positive-x direction.	103
5.11	The mean and variance of the displace between the original interaction location and the centroid of the electron cloud. The variance is calculated for the displace spreading along x, y and z directions. The biggest variance among the three directions is shown in this plot. . .	104
5.12	Simulated improvement of Compton imaging quality using simple back-projection method after applying sub-pixel position calculation algorithm and displacement correction. The sub-pixel position resolution is assumed to be 300 μm . The gamma-ray source is 1460 keV.	105
5.13	The observed improvement of Compton imaging quality using simple back-projection method after applying sub-pixel position calculation algorithm and displacement correction on detector # 4E3. The sub-pixel position resolution is estimated to be about 300 μm . The gamma-ray source is Co-60 1332-keV line.	106
5.14	The measured energy resolution changing with depth for several channels. This data is obtained from detector # 4E3 with the cathode biased at -3000V and the grid biased at -40V. This detector is a $20 \times 20 \times 15 \text{ mm}^3$ CdZnTe detector made by eV product.	107

5.15	The 662keV photopeak centroid variation with sub-pixel position at two depths This plot is measured on 4E7 with the thickness about about 15 mm and the cross-section as $20 \times 20 \text{ mm}^3$. This detector is made by eV product.	108
5.16	The measured weighting potential crosstalk as a function of distance and depth. The blank region is because the distance is too close that no crosstalk data can be obtained. The unit of the crosstalk amplitude is keV. This data is obtained from detector # 4E3 with the cathode biased at -3000V and the grid biased at -40V. This detector is a $20 \times 20 \times 15 \text{ mm}^3$ CdZnTe detector made by eV product. . .	110
6.1	Filter performance for cathode signals. The noise and waveform profile is obtained on detector # 3E2 with cathode biased at -2500V and grid biased at -30V.	113
6.2	The timing resolution versus the percentage threshold. The different color represents different shaping time. The noise and waveform profile is obtained on detector # 3E2 with cathode biased at -2500V and grid biased at -30V. The energy deposition is assumed to be 662 keV.	115
6.3	The timing performance of various filters for anode signals. The percentage threshold is set to be 50%. The noise and waveform profile is obtained on detector # 3E2 with cathode biased at -2500V and grid biased at -30V. The energy deposition is assumed to be 662 keV. . .	116
6.4	The trigger time resolution obtained through various types of filters for cathode signals. Different lines of the same color are for those cathode waveforms from different depth. The noise and waveform profile is obtained on detector # 3E2 with cathode biased at -2500V and grid biased at -30V. The energy deposition is assumed to be 662 keV.	117
6.5	The depth resolution versus the percentage threshold. The noise and waveform profile is obtained on detector # 3E2 with cathode biased at -2500V and grid biased at -30V. The energy deposition is assumed to be 662 keV.	118
6.6	The performance of various types of filters for cathode signals. The noise and waveform profile is obtained on detector # 3E2 with cathode biased at -2500V and grid biased at -30V. The energy deposition is assumed to be 662 keV.	119

6.7	The energy limit of the fast shaper method using percentage threshold. The minimum percentage threshold is 3-times noise variance. The cathode side signals are used. The noise and waveform profile is obtained on detector # 3E2 with cathode biased at -2500V and grid biased at -30V. The energy deposition is assumed to be 662 keV. . .	119
6.8	The performance of detector # 3E2 measured with the UM_VAD ASIC. The energy resolution for each pixel is shown by the resolution map located above the spectrum. Energy resolution equal to 0 means bad pixel or poor photopeak. The detector has its cathode biased at -2500 V and its grid at -30 V.	121
6.9	The performance of detector # 4E3 measured with the UM_VAD ASIC. The detector has its cathode biased at -3000 V and grid at -40 V.	121
6.10	The performance of detector # 1C37 measured with the UM_VAD ASIC. The detector has its cathode biased at -4000 V and guard ring at 0 V. Instead of room-temperature, this result was obtained at 10°C.	122
6.11	Comparison of the detector performance measured with the VAS_TA ASIC and the UM_VAD ASIC. Detector # 3E2 has its cathode biased at -2500 V and grid at -30 V. Detector # 4E3 has its cathode biased at -3000 V and grid at -40 V.	123
6.12	the drift time distribution as a function of energy deposition for single-pixel events. The data is obtained with detector # 4E3 with its cathode biased at -3000 V and grid at -40 V. The detector thickness is 15 mm.	124
7.1	An example of the system response function measured for collecting pixel and cathode. Channel 40 is picked for this example. With the color changes from blue to yellow and then to red, the depth varies from the anode side to the cathode side.	133
7.2	The calculated weighting potential difference for various interaction locations. Each colored line is the weighting potential for the pixel of the same color. Each colored circle marks the interaction location of the pixel with the same color.	136
7.3	The influence of trapping on the neighboring pixels. The signal waveform is obtained from experimental data. The trapping is added artificially. The final waveforms are normalized to have the same maximum value.	137

7.4	Comparison of the normalized induced signal on the right side neighbor when the electron cloud is located at different collecting pixels.	137
7.5	The measured system response function of the neighboring pixels for 9×9 at depth 30, which is about 3.2 mm away from the cathode surface. The different colored lines are the induced signals from the neighboring pixel of the same color.	139
7.6	The measured system response function for 8 neighbors at depth 30, which is about 3.2 mm away from the cathode surface. The different colored lines are the induced signals from the neighboring pixel of the same color. The green dot marks the interaction location.	140
7.7	The measured system response function for 8 neighbors at depth 10, which is about 3.9 mm away from the anode surface. The different colored lines are the induced signals from the neighboring pixel of the same color. The green dot marks the interaction location.	140
7.8	The flow chart of the system response function fitting algorithm. .	144
7.9	An example of SRF fitting method applied to a single-pixel event. .	145
7.10	The single-pixel event spectrum before and after the charge leak correction. The data is obtained from detector # 4E3. The cathode is biased at -3000 V and the grid is at -40 V. The energy resolution is slightly improved from 0.81% to 0.80%.	146
7.11	An example of the SRFSF method for the system response of a neighboring pixel. The turning difference indicates fast electron trapping and de-trapping. Depth 5 is about 5 mm away from the anode surface.	147
7.12	The area of the turning difference as a function of the interaction depth.	147
7.13	An example of the SRFSF method. The turning difference indicates fast electron trapping and de-trapping. Depth 5 is about 5 mm away from the anode surface.	148
8.1	The convergence of the MLEM method for electron cloud distribution calculation.	156

8.2	fraction of the events whose electron cloud orientation separated less than 30 degree from the electron emitting direction. The isotropic line shows the case when the electron cloud orientation is totally irrelevant to the initial electron emitting direction. Each pixel is divided into 10×10 sub-pixels.	157
8.3	The calculated electron cloud distribution using MLEM method with different electronic noise. The electron used in this simulation is 1243 keV. Each pixel is divided into 10×10 sub-pixels. The depth is divided into totally 30 depths. This plot only shows 10 depths where the cloud is located.	158
8.4	The simulation result of the electron cloud distribution calculation algorithm using MLEM. The electronic noise is assumed to be 1 keV and the recoil electron energy is 1243 keV.	159
8.5	The separation angle between the original electron emitting direction and the electron cloud orientation. The electron cloud orientation is obtained from the real electron cloud distribution and the calculated distribution using MLEM method.	160

LIST OF APPENDICES

Appendix

A.	Model-matched Fitting	162
B.	Detector Symbols	166

ABSTRACT

Digital Signal Processing Methods for Pixelated 3-D Position Sensitive
Room-Temperature Semiconductor Detectors

by

Yuefeng Zhu

Chair: Zhong He

CdZnTe detectors have been developed since 1990s [8, 29, 44, 11, 27, 13]. They have shown great potential to be one of the room-temperature substitutes of traditional HPGe detectors. Many efforts have been made to make CdZnTe detectors to approach the theoretical 0.2 % FWHM energy resolution at 662 keV. The 3-D position-sensitive pixellated CdZnTe detectors have demonstrated 0.48 % energy when the electronic noise is low, which is close to the theoretical limit. However, current ASICs that only readout the signal amplitude and timing information have several limitations, which placed lots of obstacles on further improvement of the performance of CdZnTe detectors, especially for multi-pixel and high-energy events. In order to overcome those limitations, a new digital ASIC, which is capable of readout pre-amplifier pulse waveforms is developed. This thesis presents several signal processing techniques base on this digital ASIC. First, the electronic noise and its characteristics is studied and discussed. A new fitting method utilize the characteristics of noise is presented and its performance is demonstrated. Then, a new position sensing technique that presents sub-pixel lateral position resolution is discussed. The improvement of Compton imag-

ing after employing such an algorithm is demonstrated. The potential of using sub-pixel position sensing to further improve energy resolution is depicted. Finally, a new energy and position reconstruction algorithm based on the concept of system response function is described. The method to generate system response function is presented. Several benefits of the system response function fitting algorithm is demonstrated.

CHAPTER I

Introduction

1.1 Room-temperature Semiconductor Detectors

Semiconductor detectors have been introduced into the field of radiation detection for more than half a century. Their merits, especially the small ionization energy required to create the information carriers: electron-hole pairs and small values of Fano Factor, provide the best achievable spectroscopic performance among all types of detectors.

The earliest two types of semiconductor detectors are Ge and Si detectors. Si has very low Z , and they (mostly Li-Drifted Si detectors) are widely used in low energy X-rays or charged particle spectrometry. Ge has Higher Z and good stopping power for gamma rays. Although HPGe detectors still keep the record of the best energy resolution for gamma rays, their requirement of cooling to liquid nitrogen temperature (77K) is an obstacle for many applications, such as hand-held radiation detection devices. Recently, there are many efforts to develop new types of semiconductor detectors that can be operated at room temperature and at the same time can provide high energy resolution close to HPGe detectors. These new materials include CdTe [31, 43], HgI₂ [31, 38], CdZnTe [31, 13, 51], TlBr [18] etc.

Great efforts have been done for past several decades and CdZnTe has been proven to be a very promising candidate for future room-temperature semiconductor detec-

tors. Prof. Zhong He and his group have demonstrated that CdZnTe can achieve as good as 0.48 % FWHM energy resolution at 662 keV using BNL ASIC with 2-keV electronic noise [52] and 0.39 % FWHM with a lower 1.5 keV FWHM electronic noise, showing the excellent potential of CdZnTe material. Recently, Redlen Corp. has completed a contract supplying more than 130 $20 \times 20 \times 15$ mm³ CdZnTe detectors to Prof. Zhong He's group, which average better than 1 % FWHM energy resolution at 662 keV [23]. This significant progress has ensured the bright future of CdZnTe as a room-temperature alternate to HPGe detectors.

1.2 Shockley-Ramo Theory and Weighting Potential

Shockley-Ramo theory [12] is the most important basis behind the development of modern CdZnTe detectors. It presents a method to calculate the induced signals of moving charges on any electrodes inside a detector. With this tool, people can design various types of electrodes to provide desired signals.

According to Shockley-Ramo theory, the total induced charge on an electrode can be calculated by

$$Q = -q [\phi_0(\vec{x}_1) - \phi_0(\vec{x}_2)] \quad (1.1)$$

Here, $\phi_0(\vec{x}_1)$ and $\phi_0(\vec{x}_2)$ is the weighting potential of the electrode at position \vec{x}_1 and \vec{x}_2 respectively. Q is the induced charge on the electrode when the charge q moves from \vec{x}_1 to \vec{x}_2 .

Weighting potential is a virtual potential used to describe the charge induction on an electrode. It is computed by artificially setting the electrode of interest to be 1 and all others to at 0. The potential obtained under this artificial boundary condition is the weighting potential. For example, in a traditional planar semiconductor detector as shown in figure 1.1, the weighting potential for the planar anode is the red line, a linear function. Using equation 1.1, one can calculate the induced signals on the

anode. Assuming an interaction happens at depth Z_0 , electrons and holes would be generated and drift to anode and cathode respectively. If both of them can drift all the way through the detector, as what they do in HPGe, and reach cathode and anode respectively, one can obtain their induced signals as marked as the violet and green lines. Obviously, the amount of signal individually induced by electrons and holes is a function of interaction depth. However, the total signal adding electron signal and hole signal together becomes a constant as illustrated by the blue line, which is why the signal output from HPGe detectors is only a function of the number of ionized electron-hole pairs and there is no dependence on the interaction location.

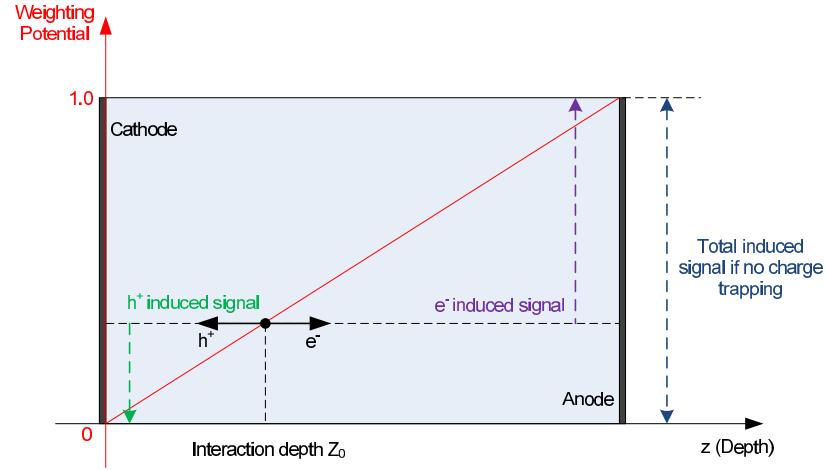


Figure 1.1: An illustration of the signal induction in a planar semiconductor detector.

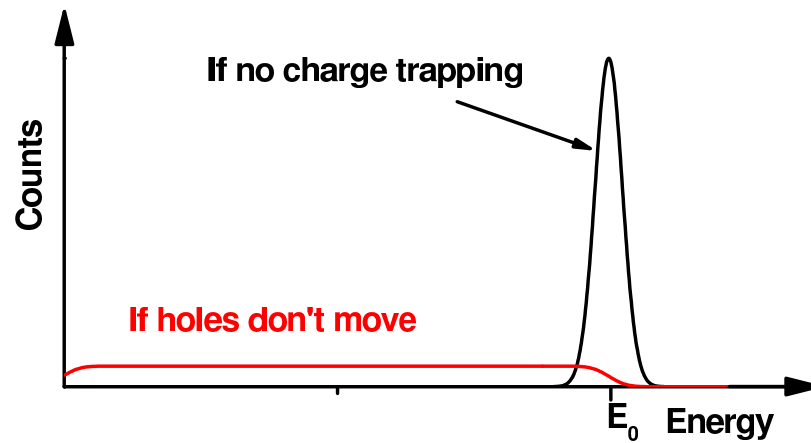


Figure 1.2: The pulse height spectra when the energy deposition is fixed. [12]

However, in compound semiconductors such as CdZnTe, charges can be trapped when travel through the material. The slower the charge moves, the more severe charge trapping can happen. Electrons in CdZnTe drift faster and therefore electron trapping is smaller. However, holes in CdZnTe travel very slow and almost all holes are trapped shortly after they are generated. As a result, the hole induced signal will be lost and only electron signals can be readout out. Apparently, in this case, the induced signal on the anode is a function of interaction depth and isn't uniquely determined by the number of ionized electron-hole pairs. Figure 1.2 presents an illustration of the pulse height spectra when the energy deposition is fixed. The black line shows the expected peak when both holes and electrons can move fast while the red line shows a continuum when only electrons are collected. Therefore, the configuration of planar detector can't be used to build CdZnTe gamma-ray spectrometers.

People have encountered similar problem in gas ion chambers. Ions have similar slow-drift properties as holes. Therefore, in gas detector electrons are also the major contributor to the signal induction. To remove the dependence of the output signal on the interaction position, a special electrode called Frisch grid [26] was invented. As shown in figure 1.3, Frisch grid is a grid electrode that is typically placed close to the anode in ionization chambers. Frisch grid can block any signal induction on the anode when electrons drift in the sensitive region. The anode induced signal of any interaction happened in the sensitive region is proportional to the number of ionized electrons and the weighting potential change from the Frisch grid to the anode, which is a constant value 1. Therefore, Frisch-grid detectors make interaction position no longer affect the amplitude of the anode induced signal.

1.3 The Development of CdZnTe Detectors

Single-polarity charge sensing, which is to collect signals from the drift of only one type of charge carriers, electrons in this case, has to be applied in CdZnTe to

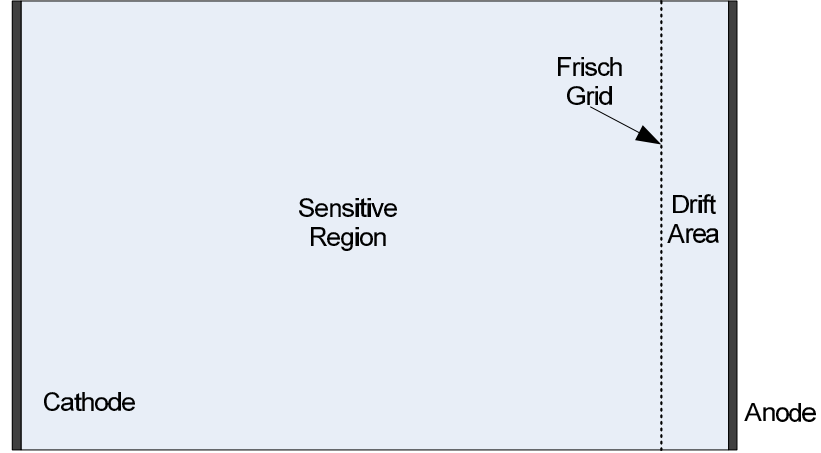


Figure 1.3: Schematic of a ionization chamber with a Frisch grid.

solve the problem of the dependence of signal induction on interaction location. Two effective techniques have been invented: coplanar grid anode and pixellated anode.

1.3.1 Coplanar-grid CdZnTe Detectors

To imitate the Frisch grid in semiconductor detectors, a creative design of anode was invented by Luke which is called coplanar grid [27] as shown in figure 1.4. Stripe electrodes have been used in position-sensitive Si detectors. It is consisted of many thin stripe electrodes placed in parallel to provide position information of interactions. Coplanar grid anode employs the similar strip electrodes but those strips are connected in an alternate manner to create two groups. One group is kept grounded to collect electrons and it is called collecting grid. The other is biased at a negative voltage to drive the electrons away and it is called non-collecting grid. The weighting potential of the collecting and the non-collecting grid is found to be similar in the detector bulk and it starts to differ only in the anode vicinity. Therefore, the signal difference of position dependence can be removed by subtraction the induced signal on the collecting grid from that on the non-collecting grid when the interaction happens in the detector bulk. With coplanar grid, good energy resolution of about 2 % FWHM at 662 keV has been achieved at room temperatures [16] and 1 % at -20 °C

[1].

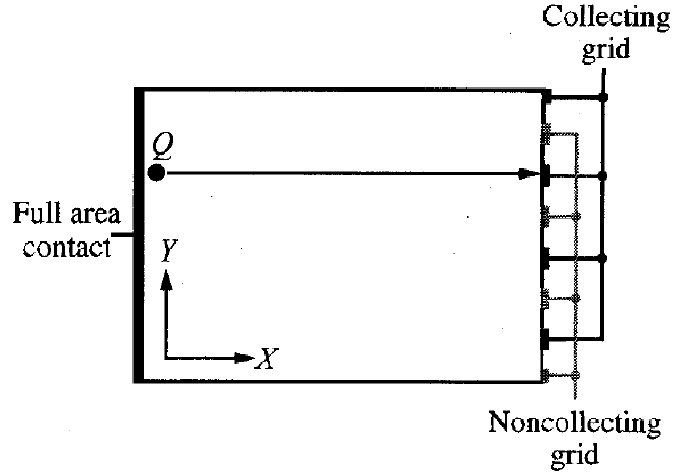


Figure 1.4: Schematic of a simple coplanar-grid structure. [27]

1.3.2 3-D Position-sensitive Pixellated CdZnTe Detectors

However, the theoretical limit of CdZnTe is estimated as 0.2 % FWHM at 662 keV [15] (if we consider the Fano Factor to be 0.1 [37, 2, 33, 28]), which is much better than the experimental result. In order to further improve the energy resolution of CdZnTe detectors, Prof. Zhong He introduced the 3-dimensional position sensing technique [14]. Figure 1.5 shows the configuration of a pixellated CdZnTe detector. The anode is divided into 11 by 11 pixels and the cathode is made as a planar electrode. In addition, there is an extra electrode called steering grid placed between the pixels. Steering grid is biased at a lower voltage than the pixels so that electrons that fall in the gap of pixels can be driven toward the adjacent pixels to help increasing the charge collection efficiency.

There are generally three benefits to make anode pixllated: (1) small pixel effect can weaken the dependence of induced signal on interaction position; (2) pixellated anode make it possible to sense interaction depth and then perform correction of the induced signals based on the interaction depth; (3) the multiple-site-interaction

events can be identified and their energy can be reconstructed.

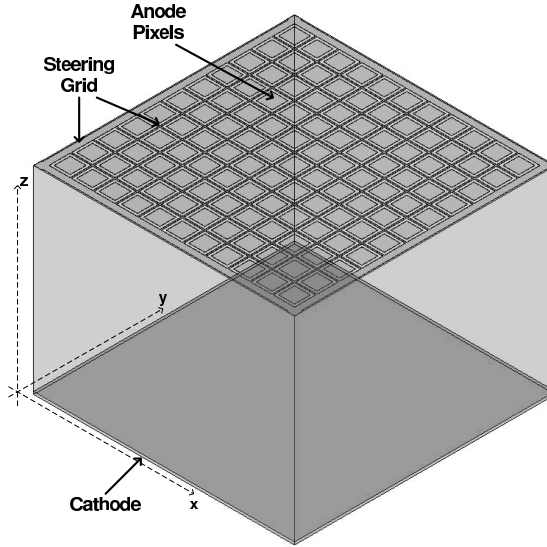


Figure 1.5: An illustration of the pixelated CdZnTe detector used in this study.

1.3.2.1 Small Pixel Effect

Based on the Shockley-Remo theory, the weighting potential of a pixel anode can be calculated and it is found that the induced signal of a pixel anode has very weakly dependence on the interaction depth when the interaction happens in the detector bulk. The smaller the pixel is, the weaker the dependence is. Therefore, this phenomenon is called small pixel effect [4]. Because of this effect, without any sophisticated correction algorithm to the anode signal, the raw anode energy spectra can show a similar peak as figure 1.2. The sharpness or the resolution of the peak can be quite good comparing to the energy resolution of 2 % FWHM at room temperature in coplanar grid detectors, especially for those detectors with low electron trappings such as the one illustrated in figure 1.6.

1.3.2.2 Depth Sensing technique and Energy Reconstruction

The electrode configuration on the anode and the cathode of the pixellated CdZnTe detectors is not the same, so that the induced signals on the cathode and anode are

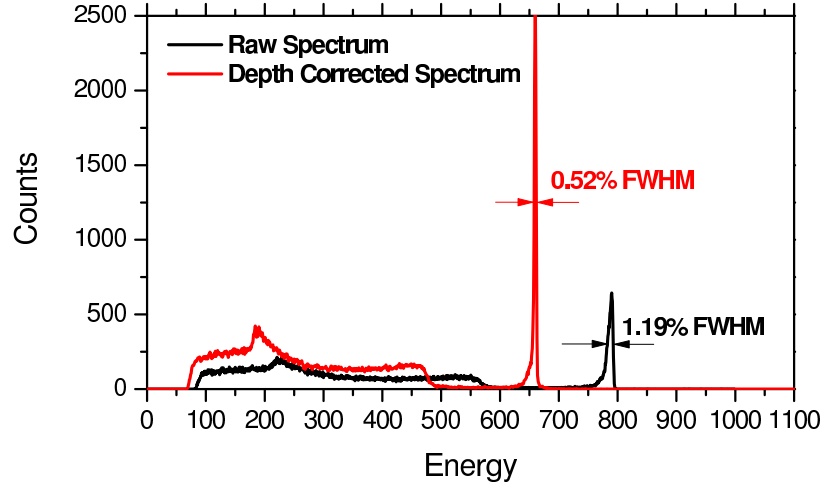


Figure 1.6: The raw spectrum and corrected spectrum of ^{137}Cs collected using a Redlen 15-mm thick CdZnTe detector (detector # 4R169) at room temperature. The pixel pitch is 1.72 mm.

in fact different. Since the cathode is a planar electrode, its weighting potential is a linear function of interaction depth as depicted in figure 1.1. As a result, the induced signal on the cathode is proportional to the interaction depth and also proportional to the energy deposition. For the anode, because of the small pixel effect, the induced signal is approximately proportional only to the energy deposition. Therefore, the ratio between the cathode signal and the anode signal for each event can be used to determine the interaction depth [14].

In addition, Based on interaction depth, a correction can be made to compensate the change of induced signal on the anode because of electron trapping and weighting potential variation. Optimal energy resolution can be achieved after this so-called depth correction as shown in figure 1.6. As mentioned above, we have achieved 0.48 % FWHM energy resolution at 662 keV on BNL ASICs [52], which is close to the theoretical limit of CdZnTe.

1.3.2.3 Multi-pixel Events Energy reconstruction and Cross Talk Correction

One significance of pixellated detector is its capability of identify 3-D position of individual interaction of a multiple-site-interaction event if each interaction triggers one pixel. Because of the small pixel effect, the anode signal rises only when the electrons reach anode vicinity, which makes it possible to obtain the drift time of electrons from their origin to the anode surface and therefore the interaction depth of each interaction can be given. The depth correction can be performed pixel by pixel to those multiple-site-interaction events. The 3-D position of individual interaction can be used for Compton Imaging [49]. In addition, there is crosstalk between pixels when multiple pixels are triggered [50]. In fact, when charges are collected by a pixel, not only the collecting pixel has signal, but all the pixels in the detector would have signal induced. If multiple pixels get triggered, the total induced signal on one collecting pixel includes the induced signals from the charges that are not collected by this pixel. Those induced signals on the non-collecting pixels are small but they are big enough to degrade the energy resolution if they are left uncorrected.

Apparently, because of the existence of charge sharing among several pixels, multi-pixel events don't necessarily mean multiple-site-interaction events. In addition, it is also possible that a multiple-site-interaction event only triggers one pixel. Therefore, event classification needs to be performed for those multiple pixel triggered events or multi-pixel events as we call before energy correction or imaging algorithm is applied.

There are also several other benefits of pixellated anode, which are

1. Pixels have smaller input capacitance and weaker leakage current, and thus lower electronic noise.
2. Pixellation make the detector much less sensitive to material non-uniformity

which is still common in recent CdZnTe crystals.

1.4 Summary

This chapter presents a brief introduction to the development of CdZnTe detectors. The energy reconstruction and position determination method used for 3-D position-sensitive pixellated detector is briefly discussed. This thesis discusses several new energy and position reconstruction algorithms based on a newly developed pre-amplifier waveform digitalizing ASIC. Chapter II introduces the attributes of electronic noise and presents a new fitting method based on accurately modeling the electronic noise. Chapter III gives the simulation method for the whole detector system. Chapter IV describes the new pre-amplifier waveform digitalizing ASIC - the UM_VAD ASIC. Chapter V to chapter VIII presents the new algorithms developed based on the UM_VAD ASIC, including sub-pixel position calculating algorithm, system response function fitting algorithm and electron cloud distribution calculation algorithm.

CHAPTER II

Electronic Noise and Digital Filters

2.1 Introduction

Electronic noise is a critical role in a detector system that has significant contribution to energy resolution. Traditionally, a noise filter is employed to suppress the impact of electronic noise. In theory, there is an optimal filter that can provide the best signal-to-noise ratio. However, the optimal filter is too complicated to be realized in most practical systems. Therefore, in most systems, some simple but reasonably good filters such as CR-RC or CR-RCⁿ filters are utilized as the filter circuit or shaper sometimes as we also call. With the development of detector technology, now it is possible to readout the whole waveform of pre-amplifier signal. In this circumstance, digital filters rather than a fixed filter circuit can be applied. The advantage of using digital filters is many categories of filters with various parameters can be tested and as a result better performances can be achieved. Apparently, employment of digital filters demands more calculation time during data processing, which is, however, acceptable with the advance of computer technology.

This section presents a detailed introduction of electronic noise and filters, including the different types of noise, noise composition in a detector system, CR-RCⁿ filter and optimal filter, and the optimal signal-to-noise ratio. The purpose of this section is to provide a knowledge base to the following discussion as well as a reference for

potential readers who are interested in the traditional signal processing techniques used for nuclear measurement instruments.

2.1.1 Electronic Noise

Electronic noise includes several categories, such as shot noise [19], thermal noise [21, 35], and 1/f noise etc [10]. Based on the role noise plays in a pre-amplifier circuit, noise can also be categorized into parallel noise and serial noise. This section gives an introduction of the noise from various origins and then it presents a detailed discussion of electronics noise in a charge-sensitive per-amplifier circuit with semiconductor detectors.

2.1.1.1 Shot Noise, Thermal Noise and 1/f Noise

To quantify the amplitude of noise, we usually use the average power

$$\bar{p} = \lim_{T \rightarrow \infty} \frac{1}{T} \int_{T/2}^{T/2} v_T^2(t) dt = \int_{-\infty}^{\infty} \lim_{T \rightarrow \infty} \frac{|V_T(\omega)|^2}{T} d\omega \quad (2.1)$$

T is a selected time window and $v_T(t)$ is the truncated noise signal within this window. $V_T(\omega)$ is the Fourier transform of $v_T(t)$. The second equal is because of the Parseval theorem [36]. The power spectrum density function of noise is defined as

$$S(\omega) \triangleq \lim_{T \rightarrow \infty} \frac{|V_T(\omega)|^2}{T} \quad (2.2)$$

In a time-invariant system, the average power of noise is equivalent to the variance of noise at any time. Therefore, when we do noise analysis, the integration of the power spectrum density function is usually employed.

It should be noticed that the power spectral density functions includes one-sided power spectrum function with frequency forced to be above 0 and double-sided power

spectral density function with frequency from negative infinity to positive infinity. Both functions are meaningful in noise analysis. In this article "power spectral density functions" always means one-sided power spectrum function. If double-sided power spectral density function is used, it will be pointed out explicitly. Double-sided power spectral density function $S(\omega)$ are related to one-sided power spectrum function $s(\omega)$ through the following equation:

$$s(\omega) = \begin{cases} S(\omega)/\pi & 0 \leq \omega < \infty \\ 0 & \omega < 0 \end{cases} \quad (2.3)$$

Shot noise originated from the fluctuation of charge carriers they are generated. For example, in vacuum diode, the generation of electrons on thermal cathode follows Poisson distribution. As a result, the induced current by those electrons varies along an average current. Such variation is shot noise. In semiconductors, such as CdZnTe detectors, Schottky contacts blocks most current so that radiation caused charge flow can be sensed. However, there are still some electrons that can penetrate the Schottky barrier to form leakage current. The amplitude of this leakage current is determined by how many electrons can penetrate the barrier, which is also a statistical process. Therefore, the leakage caused electronic noise in CdZnTe detectors is in fact shot noise. Pre-amplifier is also a source of shot noise.

The amplitude or power spectral density function of shot noise depends on bandwidth of the system. However, for most practical electronic systems, their bandwidth is far lower than the bandwidth where the power density of shot noise starts to change. Therefore, shot noise can just be approximately modeled as white noise [21, 35]. Its mean current noise power spectral density function can be expressed as

$$\overline{di_s^2} = 2Ie \cdot df \quad (2.4)$$

Here I is the mean current and e is the charge of an electron.

Thermal noise is generated by thermal motion or Brownian motion of charge carriers. For example, in conductors or resistors, electrons not only drift along the direction of applied voltage, but also move randomly as thermal motion. The random movement of electrons causes the charge distribution to change and as a result, the macroscopic current varies accordingly. similar to shot noise, thermal noise can also be modeled approximately as white noise in most real electronic systems. In a resistor, the mean current power spectral density of thermal noise can be presented as

$$\overline{di_T^2} = \frac{4kT}{R} \cdot df \quad (2.5)$$

Here k is Boltzmann's constant, T is temperature and R is resistance.

1/f or flicker noise is a type of noise whose amplitude varies with a relation of $1/f^\alpha$. In most cases, α is close to 1. Obviously, the amplitude of this noise at high frequency is very small. Therefore 1/f noise is also called low frequency noise. The physical origin of 1/f noise can be generally considered as low frequency variation of material properties in the devices. Those properties include fluctuating configurations of defects in metals, fluctuating occupancies of traps in semiconductors, and fluctuating domain structures in magnetic materials [10]. In most electronic devices, 1/f usually exists. However, in most circumstances, their amplitude is much smaller than shot noise and thermal noise and they can be neglected. The power spectral density of 1/f noise can be generally written as

$$\overline{dv_F^2} = \frac{A_F}{f} \cdot df \quad (2.6)$$

Here A_F is a constant related to device properties.

There is also 1/f noise originated from the detector itself as voltage oscillation across the detector. It contributes to the electronic noise of the pre-amplifier signal

in the form of current variation flowing out from the detector. Usually, the resistance of radiation detectors is very large. Therefore, the $1/f$ current noise from detector itself can be ignored.

It should be mentioned that $1/f$ noise not only exists in electronics but also is commonly observed in the natural world, such as channel noise in neurons. In fact, $1/f$ noise is one of the three general categories of noise in the physical world. The other two categories of noise are white noise, including shot noise and thermal noise, and Brown noise which can be seen as an integration of white noise. Brown noise has a $1/f^2$ spectrum. In the next section, we will see how white noise can be transferred into Brown noise after passing through the feedback resistor in the pre-amplifier circuit.

2.1.1.2 Parallel and Serial Noise

In a semiconductor detector system with charge-sensitive pre-amplifier, there are lots of noise sources. Before discussing those noise sources individually, let's first have a simple review of the pre-amplifier circuit. Figure 2.1 illustrates the pre-amplifier circuit for semiconductor detectors. The current signal generated in the detector integrates on the feedback capacitor C_f to form a voltage output. It represents the induced charge on the corresponding electrode connected with the pre-amplifier. The feedback resistor R_f discharges the feedback capacitor and resets the pre-amplifier after each event.

The electronic noise in the system originates from every component of the circuit. To be specific, it includes the detector leakage current shot noise, the detector thermal noise, the leakage current shot noise, channel thermal noise and $1/f$ noise inside the FET of the operational amplifier and the feedback resistor thermal noise. The channel thermal noise [9] differs from resistor thermal noise, but it still belongs to thermal noise and its amplitude is proportional to temperature. The expressions of those noise

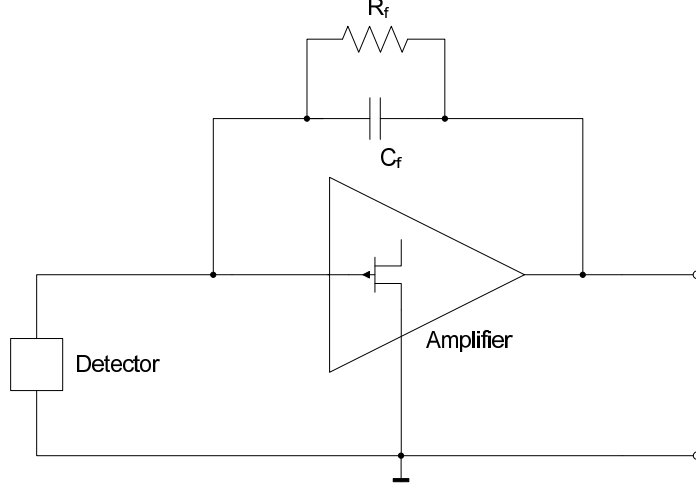


Figure 2.1: An illustration of the charge-sensitive pre-amplifier circuit for semiconductor detectors.

sources are listed below,

$$di_{DL}^2 = 2eI_D \cdot df \quad (2.7)$$

$$di_{RD}^2 = \frac{4kT}{R_D} \cdot df \quad (2.8)$$

$$di_{TL}^2 = 2eI_g \cdot df \quad (2.9)$$

$$dv_{TC}^2 = \frac{8kT}{3g_m} \cdot df \quad (2.10)$$

$$dv_{TF}^2 = \frac{A_f}{f} \cdot df \quad (2.11)$$

$$di_{Rf}^2 = \frac{4kT}{R_f} \cdot df \quad (2.12)$$

Here, di_{DL}^2 is detector leakage noise, di_{RD}^2 is detector thermal noise, di_{TL}^2 is FET leakage noise, dv_{TC}^2 is FET channel thermal noise, dv_{TF}^2 is FET 1/f noise and di_{Rf}^2 is the feedback resistor thermal noise.

All those noise sources are illustrated in figure 2.2. Generally speaking, there are two categories of noise: (1) di_{DL}^2 , di_{RD}^2 and di_{TL}^2 are in parallel with the detector signal and they are called parallel noise. di_{Rf}^2 can be also considered approximately parallel to the detector signal since the output impedance of the operational amplifier

is very small; (2) dv_{TC}^2 and dv_{TF}^2 appear as voltage signals and they are in serial with the detector signal, so that we call them serial noise. Obviously, those two categories of noise have different type of contribution to the output of the pre-amplifier circuit.

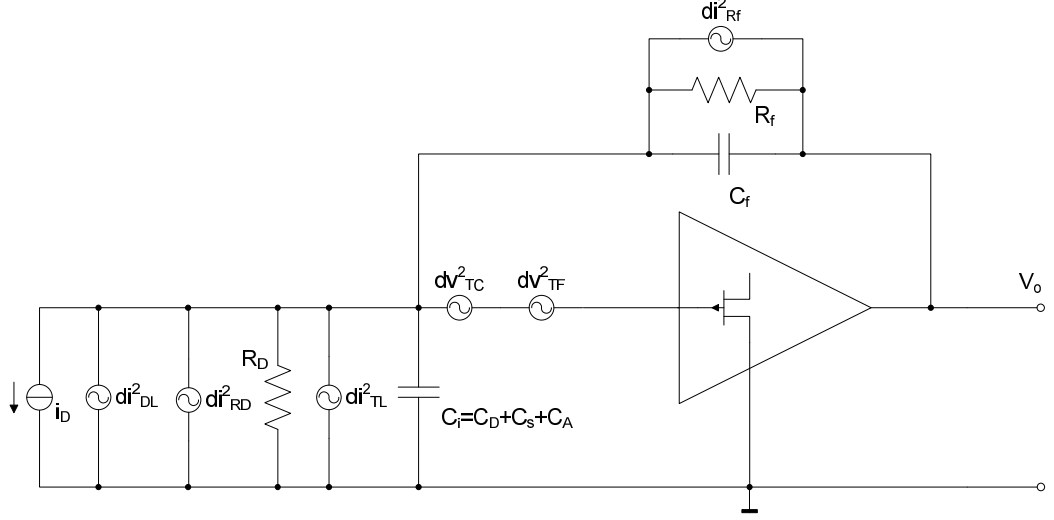


Figure 2.2: An illustration of noise sources in the charge-sensitive pre-amplifier circuit for semiconductor detectors. In this plot, di_{DL}^2 is detector leakage noise, di_{RD}^2 is detector thermal noise, di_{TL}^2 is FET leakage noise, dv_{TC}^2 is FET channel thermal noise, dv_{TF}^2 is FET 1/f noise and di_{Rf}^2 is the feedback resistor thermal noise, i_D is detector signal, R_D is detector resistance. C_D , C_s and C_A are detector capacitance, circuit distributed capacitance and amplifier input capacitance. C_i can be seen as the total input capacitance to the pre-amplifier. R_f and C_f are feedback resistor and capacitor respectively.

Figure 2.3 depicts the equivalent circuits for serial noise and parallel noise. The detector resistor and feedback resistor usually have much larger impedance than the input capacitors and the feedback capacitor and they are in parallel with those capacitors, so that those resistors can be neglected in the equivalent circuits. The equivalent

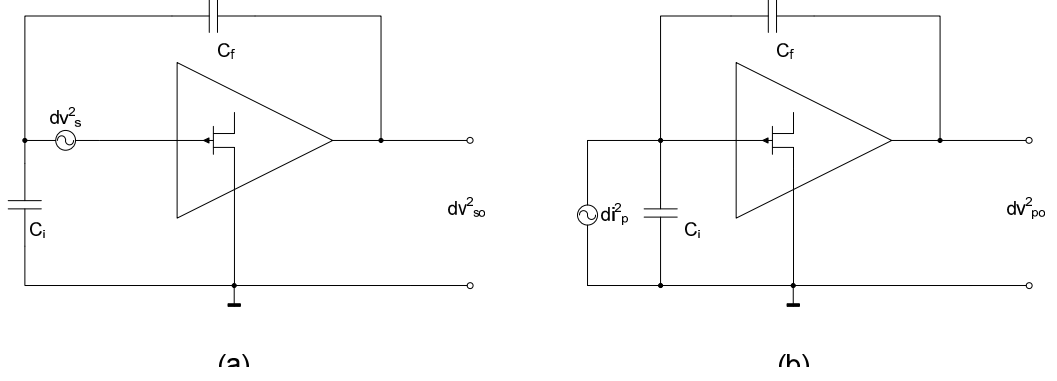


Figure 2.3: The equivalent circuit for (a) serial noise and (b) parallel noise. In these plots, $dv_s^2 = dv_{TC}^2 + dv_{TF}^2$ and $di_p^2 = di_{DL}^2 + di_{RD}^2 + di_{TL}^2 + di_{Rf}^2$. dv_{so}^2 and dv_{po}^2 are the equivalent output noise of the pre-amplifier.

output noise of parallel noise and serial noise can be simply derived as,

$$\begin{aligned}
 dv_{so}^2 &= \frac{(C_i + C_f)^2}{C_f^2} \cdot dv_s^2 \\
 &= \frac{(C_i + C_f)^2}{C_f^2} \cdot \left(\frac{4kT}{3\pi g_m} \cdot d\omega + A_f \cdot \frac{d\omega}{\omega} \right)
 \end{aligned} \tag{2.13}$$

$$\begin{aligned}
 dv_{po}^2 &= \left(\frac{1}{2\pi f C_f} \right)^2 \cdot di_p^2 \\
 &= \frac{1}{2\pi C_f^2} \cdot \left[2e(I_D + I_g) + 4kT \left(\frac{1}{R_D} + \frac{1}{R_f} \right) \right] \cdot \frac{d\omega}{\omega^2}
 \end{aligned} \tag{2.14}$$

Usually, circular frequency ω is more commonly used, so that we substitute f by ω with the relation $\omega = 2\pi f$ in the above equations.

Denote

$$a^2 = \frac{(C_i + C_f)^2}{C_f^2} \cdot \frac{4kT}{3\pi g_m} \tag{2.15}$$

$$b^2 = \frac{1}{2\pi C_f^2} \cdot \left[2e(I_D + I_g) + 4kT \left(\frac{1}{R_D} + \frac{1}{R_f} \right) \right] \tag{2.16}$$

$$c^2 = \frac{(C_i + C_f)^2}{C_f^2} \cdot A_f \tag{2.17}$$

The total equivalent output noise can be expressed as

$$dv_n^2 = dv_{so}^2 + dv_{po}^2 = \left(a^2 + \frac{b^2}{\omega^2} + \frac{c^2}{\omega} \right) d\omega \quad (2.18)$$

There are three terms in the expression. Each term has different dependence on frequency. Obviously, term b represents parallel noise. Term a and term c are both parts of serial noise. However, usually $1/f$ noise is small and term c can be neglected. Therefore, for convenience, in the following discussion we will just call term a as serial noise term and call term c as $1/f$ noise term.

2.1.2 Filters

This section introduces the basic concept of filters. The mathematical expression of CR-RCⁿ filter and optimal filter will be discussed. The noise amplitude after the pre-amplifier signal having passed the filter will be presented.

If we assume there is a signal $v(t)$ and it will pass a filter with the impulse response as $h(t)$, the output $r(t)$ will be

$$r(t) = v(t) * h(t) \quad (2.19)$$

In frequency domain the output would be

$$R(\omega) = V(\omega) \cdot H(\omega) \quad (2.20)$$

CR-RCⁿ filters are the most commonly used filter because they are easy to implement and their performance is relatively good. Figure 2.4 shows the schematics of a CR-RCⁿ filter. Its impulse response function can be easily calculated in frequency domain,

$$H(\omega) = \frac{j\omega\tau}{(1 + j\omega\tau)^{n+1}} \quad (2.21)$$

Here $\tau = RC$ is the time constant. We will calculate the noise amplitude after passing through this CR-RCⁿ filter as an example to demonstrate the filtering process.

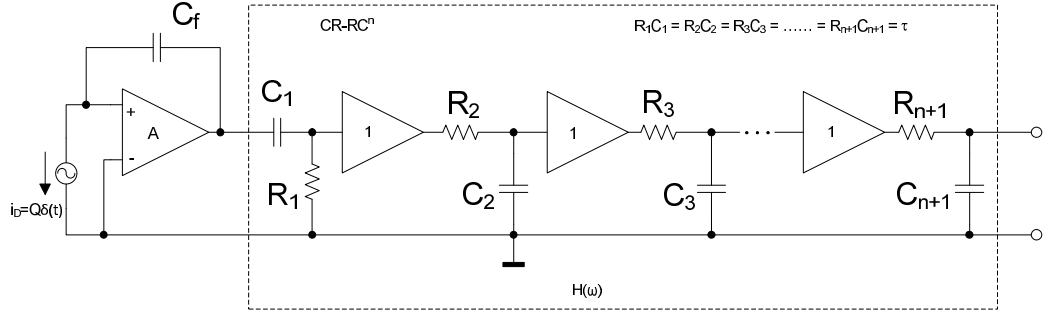


Figure 2.4: An illustration of a CRRCⁿ filter circuit.

The amplitude of electronic noise after passing through this CRRCⁿ filter can be calculated as

$$V_n^2 = \int_0^\infty |H(\omega)|^2 dv_n^2 \quad (2.22)$$

Substitute dv_n^2 using equation 2.18, we can obtain the noise amplitude to be

$$V_n^2 = \frac{a^2\pi}{2\tau} \cdot \frac{(2n-3)!!}{(2n)!!} + \frac{b^2\tau\pi}{2} \cdot (2n-1) \frac{(2n-3)!!}{(2n)!!} + c^2 \cdot \frac{1}{2n} \quad (2.23)$$

The first term with a belongs to serial noise and the second one with b is from parallel noise. The contribution of serial noise and parallel noise changes with τ , which is why an optimal time constant needs to be found when using CR-RCⁿ filters. However, the contribution of 1/f noise as presented by the term with c is irrelevant to the time constant. It only changes with the rank n for CR-RCⁿ filters. The lowest noise can be reached at the optimal time constant as shown below:

$$\tau_{opt} = \frac{\tau_c}{\sqrt{2n-1}} \quad (2.24)$$

Here, $\tau_c = a/b$ and it is called corner time. The minimum noise amplitude can then

be found to be

$$V_{n,opt}^2 = \pi \cdot \frac{(2n-3)!!}{(2n)!!} \cdot ab\sqrt{(2n-1)} + c^2 \cdot \frac{1}{2n} \quad (2.25)$$

To accurately present the performance of a filter, we usually use signal-to-noise ration. In semiconductor detectors, the input signal is a very short current impulse. It can be approximately treated as a δ function with an amplitude of Q , the total induced charge. Then we can calculate the output signal amplitude of a CR-RCⁿ filter to be [26]

$$V_M = \frac{Qn^n}{C_f n! e^n} \quad (2.26)$$

Here, C_f is feedback capacitor. The optimal signal-to-noise ratio for a CR-RCⁿ filter can then be obtained with equation 2.25 and 2.26

$$\eta_{n,opt}^2 = \left(\frac{Qn^n}{C_f n! e^n} \right)^2 \cdot \frac{1}{\pi \cdot \frac{(2n-3)!!}{(2n)!!} \cdot ab\sqrt{(2n-1)} + c^2 \cdot \frac{1}{2n}} \quad (2.27)$$

Usually, 1/f noise is much smaller than parallel and serial noise. However, in modern semiconductor detectors, 1/f noise could be significant [6]. To determine if 1/f noise is a significant component in our system, we need to measure its contribution.

If we consider equation 2.23 to be a function of τ and simplify the coefficients, we will get

$$V_n^2(\tau) = \frac{A}{\tau} + B\tau + C \quad (2.28)$$

Where, A , B and C represents the contribution of serial, parallel and 1/f noise respectively. A , B and C are in different unit and they can't be compared directly. If we change τ , the minimum total contribution from serial and parallel noise can be reached at $\tau = \sqrt{A/B}$ where

$$V_{n,opt}^2(\tau) = 2\sqrt{AB} + C \quad (2.29)$$

Therefore, C can be compared with $2\sqrt{AB}$ to determine if $1/f$ noise is significant or not. Figure 2.5 presents the measured noise amplitude changing with shaping time using CR-RC⁴ filter in detector # 3E2 ($15 \times 15 \times 10$ mm³ pixlled detector with grid fabricated by eV Product). Equation 2.28 is used to determine the contribution of $1/f$ noise and compare it with serial and parallel noise. As shown in the figure, The total amplitude for serial and parallel noise at the optimal shaping time is only about 5 times of the $1/f$ noise amplitude, indicating that $1/f$ noise is relatively large and can't be neglected in the system if the optimal performance needs to be reached. For larger $20 \times 20 \times 15$ mm³ detectors, the leakage current and input capacitor is similar. And as pointed out in section 2.1.1.2, $1/f$ noise origins in pre-amplifier and irrelevant to detectors. Therefore, $1/f$ noise should still be noticeable in the system with big CdZnTe detectors.

It should be mentioned that to ignore $1/f$ noise is also an option here since $1/f$ noise is 5-times smaller than parallel and serial noise. This approximation should result in a conclusion very close to the optimal one.

The signal-to-noise for $1/f$ noise after passing through different filters is presented in figure 2.6. The input signal is assumed to be an ideal rectangular function, corresponding to an ideal current source connected to a charge-sensitive pre-amplifier. As a comparison, serial and parallel noise are also presented in the figure. As shown, for different types of noise, the best filter is different. If the three types of noise adds together, the best filter will depend on the composition of each noise.

2.2 Optimal Filter

2.2.1 Optimal Filter for Charge Collecting Signals

The optimal filter has been derived by Radeka [40] assuming the maximum of the filtered signal as the desired measure of the signal. To construct the optimal filter, it

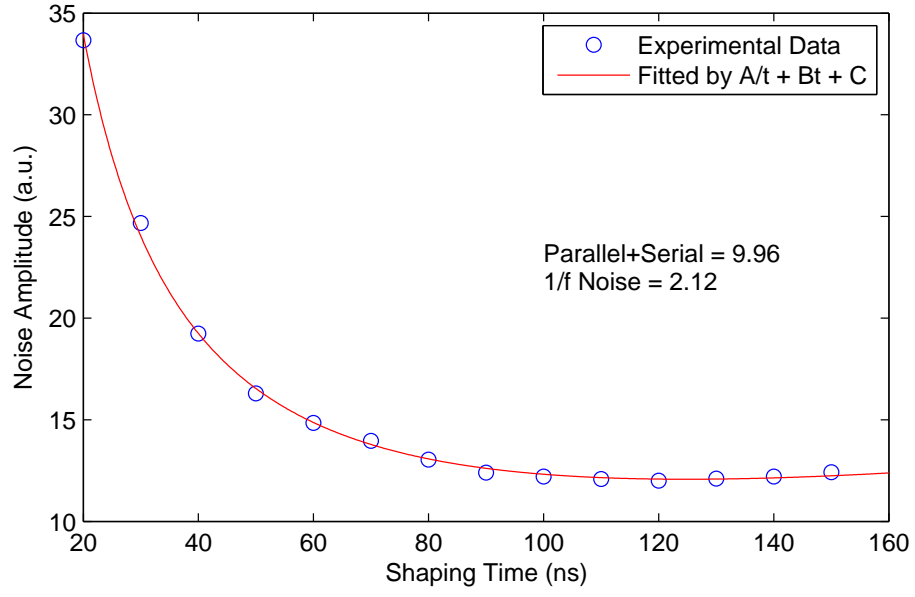


Figure 2.5: The measured noise amplitude as a function of shaping time using CR-RC⁴ filter for channel 40 in detector # 3E2 (15×15×10 mm³ pixlledated detector with grid fabricated by eV Product) with the cathode bias at -2500V and the grid bias at -30V. The sampling frequency is 80 MHz and the sampling precision is 12 bit. The data is fitted with a function of $A/t + Bt + C$ to determine the contribution from serial, parallel and 1/f noise.

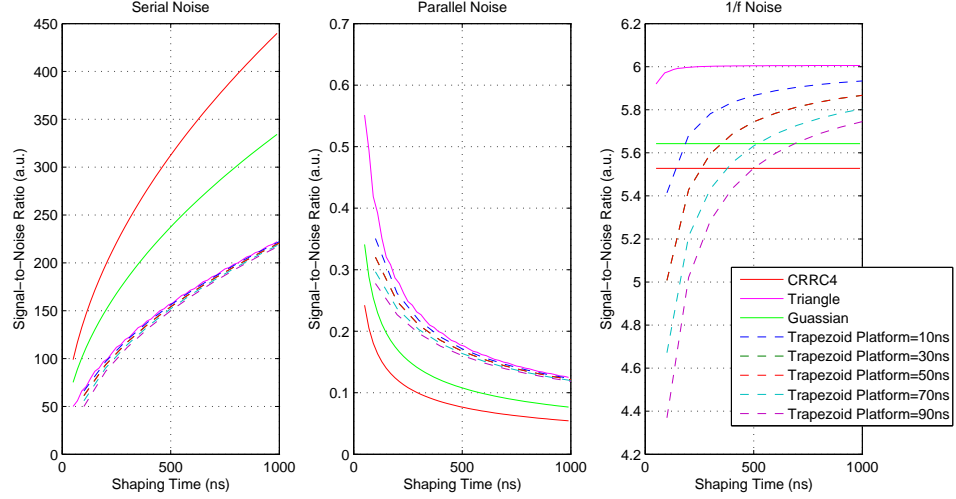


Figure 2.6: Serial, parallel and 1/f noise as a function of shaping time for various filters. Shaping time has different meaning for different filters. In this plot, we define shaping time as follows: for CRRC⁴ filter the shaping time is its time constant; for triangle filter, shaping time is the peaking time; for Gaussian filter, shaping time is the variance of Gaussian function; for trapezoid filter, shaping time is its half width.

is required to have the knowledge of input signal and noise power spectral density. If we assume the input signal to be $v_i(t) \equiv V_i(\omega)$ the double-sided noise power spectral density to be $S_i(\omega)$, the optimal filter can be expressed as

$$H(\omega) = \frac{V_i^*(\omega)}{S_i(\omega)} e^{-j\omega t_M} \quad (2.30)$$

Here, t_M is the time when the filtered signal reaches its maximum. The best signal-to-noise ratio can be

$$\eta_\infty^2 = \frac{1}{2\pi} \int_{-\infty}^{\infty} \frac{|V_i(\omega)|^2}{S_i(\omega)} d\omega \quad (2.31)$$

In semiconductor detector systems, the input signal can be approximately treated as a δ current as talked in previous section. After integrated by the feedback capacitor, the output of the pre-amplifier or the input for the shaper would be a step function $Qu(t)$, whose fourier transform is $\frac{Q}{C_f} \left(\frac{1}{i\omega} + \pi\delta(\omega) \right)$, where Q is the total charge. The power spectral density of electronic noise is shown in equation 2.18. Using equation

2.3, $S(\omega) = \pi(a + b/\omega^2 + c/|\omega|)$. Therefore, the optimal signal-to-noise ratio for semiconductor detector systems can be derived as

$$\begin{aligned}
\eta_{\infty}^2 &= \frac{1}{2\pi^2} \int_{-\infty}^{\infty} \frac{\left| \frac{Q}{C_f} \left(\frac{1}{i\omega} + \pi\delta(\omega) \right) \right|^2}{\left(a^2 + \frac{b^2}{\omega^2} + \frac{c^2}{|\omega|} \right)} d\omega \\
&= \frac{Q^2}{2\pi^2 C_f^2} \int_{-\infty}^{\infty} \frac{(1 + \pi^2 \omega^2 \delta^2(\omega))}{a^2 \omega^2 + b^2 + c^2 |\omega|} d\omega \\
&= \frac{Q^2}{2\pi^2 C_f^2} \int_{-\infty}^{\infty} \frac{1}{a^2 \omega^2 + b^2 + c^2 |\omega|} d\omega \\
&= \frac{Q^2}{2\pi^2 C_f^2} 2 \int_0^{\infty} \frac{1}{a^2 \omega^2 + b^2 + c^2 \omega} d\omega \\
&= \frac{Q^2}{\pi^2 C_f^2} \cdot K
\end{aligned} \tag{2.32}$$

$$K = \begin{cases} \frac{1}{\sqrt{|4a^2b^2 - c^4|}} \cdot \left[\pi - 2 * \tan^{-1} \left(\frac{c^2}{\sqrt{4a^2b^2 - c^4}} \right) \right] & , 4a^2b^2 > c^4 \\ \frac{2}{\sqrt{|4a^2b^2 - c^4|}} \cdot \left(\ln \left| \frac{c^2 + \sqrt{c^4 - 4a^2b^2}}{c^2 - \sqrt{c^4 - 4a^2b^2}} \right| \right) & , 4a^2b^2 < c^4 \\ 2/c^2 & , 4a^2b^2 == c^4 \end{cases} \tag{2.33}$$

To evaluate the performance of a filter, we can compare its signal-to-noise ratio η_{opt} at optimal shaping time with η_{∞} . We define the figure of merit for a filter to be $M = \eta_{opt}/\eta_{\infty}$. The bigger M is, the better the filter is. Obviously, the maximum value of M is 1. Figure 2.7 presents the figure of merit for several types of filters usually used for radiation detectors. As shown that the existence of $1/f$ noise will degrade the performance of those filters. When the ratio $c^4/4a^2b^2$ is close to 1, the degradation becomes very fast. The reason is that those traditional filters (CRRCⁿ, Gaussian, triangle and trapezoid filter) are all designed to optimize serial and parallel noise instead of $1/f$ noise. Additionally, as we know, when there is only serial noise, it can totally removed by averaging. Similarly when there is only $1/f$ noise, it should be possible to find some method to fully remove the its influence and reach infinite signal-

to-noise ratio. In this case, traditional filter still gives a finite signal-to-noise ratio and therefore their figure of merit will be 0. As shown in figure 2.7, when $c^4/4a^2b^2$ is close to 1, the figure of merit for those traditional filters falls very quickly to 0. Usually serial noise and parallel noise contribute more than 1/f noise. If in a system, 1/f noise is found to be significant, it will be required to design a new type of filter or seek a way to form the optimal filter. In our system, it has been measured that 1/f noise is about 1/5 of parallel and serial noise. The degradation of performance with this much of 1/f noise is still small. If we considering that there are other factors rather than electronic noise that contribute to energy resolution as will be discussed in next section, it won't be necessary to develop a new filter or implement the optimal filter to achieve this limited improvement.

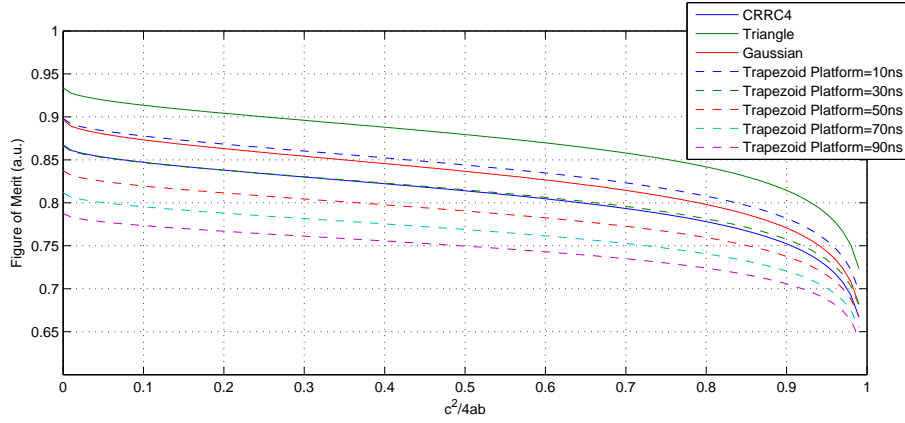


Figure 2.7: Figure of merit for various types of filters when the composition of noise is different. The contribution of 1/f noise is represented by the ratio $C^4/4a^2b^2$. The bigger the ratio is, the more important the 1/f noise component will be.

2.2.2 Optimal Filter for Transient signals

Different from charge collecting signals, the amplitude of the transient signals induced on the neighbor pixels is calculated by maximum of the filtered signal subtracted by the minimum instead of just the maximum. The reason would be described in chapter V. A typical signal can be found in figure 3.6. The optimal filter described

by Radeka [40] cannot be directly applied to those neighboring transient signals. Therefore, we will derive their optimal filter in this section based on the same logic as used by Radeka [40].

The signal amplitude for transient signals can be written as

$$\begin{aligned} v_o &= v_o(t_{max}) - v_o(t_{min}) \\ &= \frac{1}{2\pi} \int_{-\infty}^{\infty} H(\omega) V_i(\omega) (e^{j\omega t_{max}} - e^{j\omega t_{min}}) d\omega. \end{aligned} \quad (2.34)$$

Here, $v_o(t_{max})$ and $v_o(t_{min})$ are the signal maximum and minimum. $H(\omega)$ is the Fourier transform of the filter and $V_i(\omega)$ is the Fourier transform of the noise-free transient signal profile (or the mean input signal). If we know the noise power spectral density function $S_i(\omega)$, the noise amplitude can be calculated as

$$V_n^2 = \frac{1}{2\pi} \int_{-\infty}^{\infty} |H(\omega)|^2 S_i(\omega) d\omega \quad (2.35)$$

The signal to noise ratio can then be expressed as

$$\eta^2 = \frac{v_o^2}{V_n^2} = \frac{\left| \int_{-\infty}^{\infty} H(\omega) V_i(\omega) (e^{j\omega t_{max}} - e^{j\omega t_{min}}) d\omega \right|^2}{2\pi \int_{-\infty}^{\infty} |H(\omega)|^2 S_i(\omega) d\omega}, \quad (2.36)$$

The optimal signal-to-noise ratio [40] occurs when the frequency response of the filter is

$$\begin{aligned} H(\omega) &= k \frac{V_i^*(\omega)}{S_i(\omega)} (e^{-j\omega t_{max}} - e^{-j\omega t_{min}}) \\ &= k \frac{V_i^*(\omega)}{S_i(\omega)} e^{-j\omega t_{max}} [1 - e^{-j\omega(t_{min}-t_{max})}]. \end{aligned} \quad (2.37)$$

$V_i^*(\omega)$ is the conjugate of the Fourier transform of the input signal, k is a constant, and $e^{-j\omega t_{max}}$ is a time-shift term. Neither k nor $e^{-j\omega t_{max}}$ affect the signal-to-noise ratio, thus, they can be eliminated to simplify the equations. Hence, the optimal

filter for neighboring pixel signals is

$$H_{opt}^{nb}(\omega) = \frac{V_i^*(\omega)}{S_i(\omega)} [1 - e^{-j\omega(t_{min}-t_{max})}]. \quad (2.38)$$

The time interval between occurrence of the maximum and minimum signal amplitude of the shaped transient signal depends on the digital filter. As a result, it is difficult to analytically derive the solution for an optimal filter. However, a solution can be found numerically by searching through all possible time intervals.

Fig. 2.8 shows the simulation result of the optimal filters comparing with several traditional filters for charge collecting signals and neighboring transient signals.

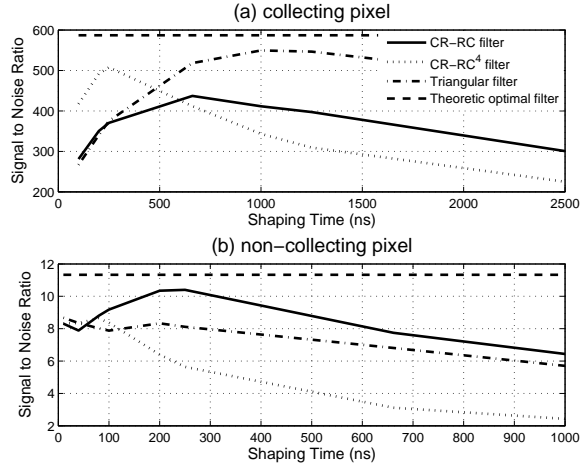


Figure 2.8: The signal-to-noise ratio of different shaping filters for: (a) the charge-collecting pixel signal, and (b) the non-collecting pixel transient signal.

2.3 Digital Filter Design

As will be presented in chapter IV, some digital readout system is capable of outputting the digitalized waveform of the pre-amplifier signals. Various filters can be applied to the data to achieve the best signal-to-noise ratio. Even the optimal filter can be forged without much effort. However, during the digitalization process,

sampling and truncation (within the data acquisition time window) have to be applied to the signal and the characteristic of the signal will be changed.

Nyquist-Shannon sampling theorem [34, 41] states that sampling frequency needs to be at least double the signal bandwidth to avoid aliasing. In fact, the frequency spectrum of a sampled signal is the sum of many frequency spectra of the original signal but shifted by the sampling frequency one by one. When the sampling frequency is not high enough, the frequency spectrum can overlap and cause aliasing. Usually an anti-aliasing filter, which is basically a low-pass filter, is applied to the circuit to make sure the signal bandwidth won't exceed half sampling frequency. Of course, this anti-aliasing filter should be coupled with the sampling frequency. During the system design phase, it is only required to make sure the sample frequency is fast enough to capture all the transient features of the signal. For example, in a $20 \times 20 \times 15$ mm³ CdZnTe detector system with the cathode biased at -3000V, the transient time for anode signals is about 200 ns, namely, 5 MHz. If using a 80 MHz sampler, the sampling frequency would be good enough to avoid signal aliasing.

So what is the consequence of sampling on electronic noise? Because of the existence of the low-pass anti-aliasing filter, high frequency white serial noise will be cut and throw away. Obviously, if any filter applied to the signal has the bandwidth lower than the anti-aliasing filter, there won't be significant influence induced by the anti-aliasing filter. The time constant of a filter controls its band limit. On the other hand, the optimal time constant of a filter is determined by noise corner time $\tau_c = \sqrt{a/b}$. Therefore, eventually whether the sampling changes the behaviors of noise or not is determined by noise corner time. For example, if we consider CR-RC⁴ filter and take the frequency where the amplitude reaches 1% of the maximum as the band limit, the band limit can be calculated to be about $2 \times 1/\tau_{opt} = 2\sqrt{7}/\tau_c$. The noise corner time in our system is about $\tau_c = 300ns$. Therefore, the band limit of the optimal CR-RC⁴ filter is 17 MHz, less than the anti-aliasing band limit (80 MHz/2=40 MHz).

In math, the truncation process is equivalent to multiplying a window function to the signal. In frequency domain, the spectrum of the signal is convolved with a sinc function. However, the impact of truncation is more complicated than what match shows us. A very important consequence of truncation is it makes the filtered noise to become time variant. As talked in section 2.1.1.1, the noise amplitude can be represented by the integration of noise power spectrum density function [5] is because the filtered noise is time-invariant. Truncation makes this assumption invalid and therefore the optimal filter described in section 2.2 won't always be applicable. Truncation also causes amplitude deficit and baseline evaluation problem [3].

Generally, we extract the maximum value of the filtered signal as the signal amplitude and the noise of interest is located at this time. Based on this knowledge, to make a filter not affected by truncation, we need to meet the following condition:

$$\int_0^T v(t)h(t_M - t)dt = \int_{-\infty}^{\infty} v(t)h(t_M - t) \quad (2.39)$$

or

$$\Rightarrow h(t) = 0, \quad t > t_M \quad \text{or} \quad t < t_M - T \quad (2.40)$$

Here t_M is the time when the filtered signal reaches its maximum and T is the time window width of truncation. $h(t)$ is the impulse response of the filter. This equation tells us that the length of the filter needs to be equal or shorter than the time window T and additionally, t_M needs to occur at the correct time (when the filter is reversed and shifted by t_M , it should still be contained by the time window T). If the optimal filter can meet this criteria, it is still the optimal filter, otherwise there will be some other filters or methods that can give better signal-to-noise ratio. If there is only white noise in the system, optimal filter is the matched filter which is the input signal waveform. The maximum amplitude occurs when the optimal filter overlaps with the signal. At this time, outside of the time window, the optimal filter is all zeros.

Therefore, equation 2.39 can be met and the optimal filter is truly the best filter. However, if there are other types of noise (parallel noise and 1/f noise) in the system, theoretically the length of the optimal filter would be infinitely long and it won't be the best filter, unless all other types of noise are so small that they can be ignored. To have a quantified standard to determine if parallel noise or 1/f noise can be ignored for the optimal filter, let's consider a simple case without considering 1/f noise,

$$\begin{aligned}
H(\omega)_{opt} &= \frac{V^*\omega}{S(\omega)} \\
&= \frac{V^*\omega}{a^2 + b^2/\omega^2} \\
&\doteq v(t) * \frac{1}{a} \left(\delta(t) - \frac{1}{2\tau_c} e^{-|t|/\tau_c} \right)
\end{aligned} \tag{2.41}$$

To make parallel noise negligible, $e^{-|t|/\tau_c}$ is the term extend the length of the optimal filter. To make sure equation 2.39 is met, $e^{-|t|/\tau_c}$ has to reach 0 very fast, for example, within just one sample interval, which indicates the sampling frequency Sa has to be

$$1/Sa \gg \tau_c \tag{2.42}$$

In our system the sampling frequency $Sa = 80$ MHz, $1/Sa = 12.5$ ns and τ_c is about 300 ns. Obviously, equation 2.42 can't be satisfied. Therefore, we won't expect the optimal filter to work well in our system.

To search for the best filter for electronic noise in our detector system without being disturbed by any physical causes that degrades the energy resolution, we collected some pure noise signals as well as the mean waveforms on the anode and cathode to simulate the measured signals. Figure 2.11 shows the performance of several traditional filters as well as the optimal filter for charge-collecting pixels. As shown, the optimal filter performs worse than the Gaussian and trapezoid filter. In fact, trapezoid filter is the simple subtraction of the mean values for two groups of samples, which is

very easy to be implemented. Since trapezoid filter and Gaussian filter have the same performance, we choose trapezoid filter as the best filter for charge-collecting pixels. Figure 2.12 shows the same plot but for neighboring-pixel transient signals. Other than fitting, CR-RC filter has the best performance. Therefore, we use CR-RC filter as the best filter for neighbor-pixel signals. As for the fitting methods, they require the signal waveforms to be known, which can only be possible after signal amplitudes have been calculated and the system response function has been established, which will be discussed in chapter VII.

2.4 Electronic Noise Correlation and Waveform Fitting

To obtain the signal amplitude, rather than filtering, there is another option we can employ which is least-square fitting if the expected signal waveform can be obtained. However, is fitting better than filtering? This section will answer this question.

Assuming the measured signal waveform to be $S_m(t)$ and the expected signal waveform profile to be $f(t)$, least-square fitting is to minimized the error function

$$E(a) = \int_0^{\infty} (S_m(t) - a \cdot f(t))^2 dt \quad (2.43)$$

where a is the signal amplitude and the signal is assumed to be 0 before measurement start time, namely time 0. By using traditionally minimization method which is to make $\frac{dE(a)}{da} = 0$, we can obtain the solution

$$a = \frac{\int_0^{\infty} S_m(t) \cdot f(t) dt}{\int_0^{\infty} (f(t))^2 dt} \quad (2.44)$$

Noticing that $\int_0^{\infty} (f(t))^2 dt$ is a constant, we find equation 2.44 represents exactly the matched filter [40]. Therefore, the least-square fitting is equivalent to a matched filter.

Is the matched filter the optimal filter? The answer is no [40]. In fact, matched filter is the optimal filter only in the condition that the noise is white Gaussian noise. Obviously, in a system with the charge-sensitive pre-amplifier the noise is not simple Gaussian noise. Therefore, least-square fitting of pre-amplifier signal won't give the optimal signal-to-noise ratio.

We can also investigate this problem from another point of view. An important feature of white noise is any number of samples of the noise are independent and identically distributed (i.i.d.). For example, if we sample the noise at time t and $t + \Delta t$ as $n(t)$ and $n(t + \Delta t)$, they are independent random variables and share the same possibility distribution. Then the joint possibility density function (p.d.f.) of a series of samples of noise can be written as

$$\begin{aligned} F(x_1, x_2, x_3, \dots, x_n) &= \prod_{i=1}^n \frac{1}{\sqrt{2\pi}\sigma} e^{-\frac{x_i^2}{2\sigma^2}} \\ &= \left(\frac{1}{\sqrt{2\pi}\sigma} \right)^n e^{-\frac{1}{2\sigma^2} \cdot \sum_{i=1}^n x_i^2} \end{aligned} \quad (2.45)$$

If a serial of samples of a measured waveform is represented as S_i^m and the expected signal is af_i (a is signal amplitude and f_i is expected signal profile), their difference should be the noise, namely, $x_i = S_i^m - af_i$. Therefore, the possibility density function of a can be derived

$$\begin{aligned} F(a) &= F(S_1^m - af_1, S_2^m - af_2, S_3^m - af_3, \dots, S_n^m - af_n) \\ &= \left(\frac{1}{\sqrt{2\pi}\sigma} \right)^n e^{-\frac{1}{2\sigma^2} \cdot \sum_{i=1}^n (S_i^m - af_i)^2} \end{aligned} \quad (2.46)$$

Obviously, the most probable a is obtained when $\sum_{i=1}^n (S_i^m - af_i)^2$ reaches minimum, which is in fact the least square method. This discuss can serve as a proof that least-square fitting is the best available method to retrieve signal amplitude when the noise is Gaussian white noise. On the other hand, this discussion also indicates

that if the noise has correlation in time, the probability model will change and model mismatch will occur when employing the least-square fitting. As a result, least-square fitting can't provide the optimal signal-to-noise ratio in a real detector system with charge-sensitive pre-amplifier.

Then what is the correct model for this corrected noise? As talked above, the i -th sample of the electronic noise is consisted of two major components: serial noise a_i and accumulated parallel noise $\sum_{j=1}^{i-1} b_j$. Additionally, there might be some baseline fluctuation and it can be modeled as common mode noise B . Therefore, the i -th noise sample can be written as

$$x_i = B + a_i + \sum_{j=1}^{i-1} b_j \quad (2.47)$$

Actually, the discharge on the feedback resistance will reduce the amplitude b_i when time goes on. Here, we ignore this effect because the time window of data acquisition is much shorter than the feedback time constance. Additionally, if we consider the low frequency $1/f$ noise, it might not be able to be modeled as a simple cumulation process as parallel noise or totally time-independent variables as serial noise. To make our model not too complicated, we guess that we can split $1/f$ noise into two components, one as a cumulation process and another is time-independent. Then those two components can be fused into variable a_i and b_i respectively. Eventually the model keeps the same, but the meaning of those variable is changed.

The joint possibility density function (j.p.d.f.) of n samples of the electronic noise

can be derived as

$$\begin{aligned}
f(x_1, x_2, x_3, \dots, x_n) &= \int_{-\infty}^{\infty} f(x_1, x_2, x_3, \dots, x_n | B, b_1, b_2, \dots, b_{n-1}) \cdot \\
&\quad f(B, d_1, d_2, \dots, d_{n-1}) dB \cdot db_1 \cdot db_2 \cdot db_3 \dots \cdot db_{n-1} \\
&= \int_{-\infty}^{\infty} f(x_1, x_2, x_3, \dots, x_n | B, b_1, b_2, \dots, b_{n-1}) \cdot \\
&\quad f(B) f(d_1) f(d_2) \dots f(d_{n-1}) dB \cdot db_1 \cdot db_2 \cdot db_3 \dots \cdot db_{n-1} \\
&= \int_{-\infty}^{\infty} K \cdot e^{-\frac{1}{2\sigma_a^2} \left[(x_1 - B)^2 + \sum_{i=2}^n (x_i - B - \sum_{j=1}^{i-1} b_j)^2 + \frac{B^2}{\alpha_B^2} + \sum_{i=1}^{n-1} \frac{b_i^2}{\alpha^2} \right]} \\
&\quad dB \cdot db_1 \cdot db_2 \cdot db_3 \dots \cdot db_{n-1}
\end{aligned} \tag{2.48}$$

K is a normalization factor. σ_a , σ_b and σ_B denote the variance of a_i , b_i and B respectively. $\alpha_B = \sigma_B/\sigma_a$ and $\alpha = \sigma_b/\sigma_a$ and they are used to simplify the equation. By maximize $f(x_1, x_2, x_3, \dots, x_n)$, we can find another method different from the least-square fitting to fit the data. We call this method matched-model fitting. However, it is hard to calculate the general expression for $f(x_1, x_2, x_3, \dots, x_n)$ for arbitrary number of sample points n and variance ratio α . To investigate the characteristics of the new matched-model fitting, let's first consider a simple case. Assuming there are only two points and $\sigma_B = \sigma_b$, we can obtain the j.p.d.f of those points to be

$$f(x_1, x_2) = K \cdot e^{-\frac{1}{2\sigma_a^2} \left(\frac{x_1^2}{(1+\alpha^2)} + \frac{(\alpha^2+1)(x_2 - \frac{\alpha^2}{1+\alpha^2}x_1)^2}{\alpha^4+3\alpha^2+1} \right)} \tag{2.49}$$

If we know the expected value for these two sample points are w_1 , w_2 and the measured value is m_1 , m_2 , the best amplitude a should make $f(x_1, x_2)$ reach maximum. So that

$$a = \frac{m_1 w_1 \left[1 + \frac{1}{(\alpha^2+1)^2} \right] + \left(m_2 - \frac{\alpha^2}{1+\alpha^2} m_1 \right) \left(w_2 - \frac{\alpha^2}{1+\alpha^2} w_1 \right)}{w_1^2 \left[1 + \frac{1}{(\alpha^2+1)^2} \right] + \left(w_2 - \frac{\alpha^2}{1+\alpha^2} w_1 \right)^2} \tag{2.50}$$

If applying least square method, the amplitude a' would be calculated as

$$a' = \frac{m_1 w_1 + m_2 w_2}{w_1^2 + w_2^2} \quad (2.51)$$

We can compute the variance of a and a' and they are

$$Var[a] = \frac{1}{\frac{2_1^2}{1+\alpha^2} + \frac{(w_2 - \frac{\alpha^2}{1+\alpha^2} w_1)^2}{\frac{\alpha^4+3\alpha^2+1}{1+\alpha^2}}} \quad (2.52)$$

$$Var[a'] = \frac{(w_1 + \frac{\alpha^2}{1+\alpha^2} w_2)^2 \cdot (1 + \alpha^2) + w_2^2 \cdot \frac{\alpha^4+3\alpha^2+1}{1+\alpha^2}}{(w_1^2 + w_2^2)^2} \quad (2.53)$$

Let $\sigma_1^2 = 1 + \alpha^2$ and $\sigma_2^2 = \frac{\alpha^4+3\alpha^2+1}{1+\alpha^2}$ and if we make w_1 and w_2 to form a two-point step function, namely, $w_1 = 0$ and $w_2 = 1$, we will get

$$Var[a] = \sigma_2^2 \quad (2.54)$$

$$Var[a'] = \sigma_2^2 + \frac{\alpha^2}{1 + \alpha^2} \sigma_1^2 \quad (2.55)$$

Obviously a has smaller variance than a' . $\alpha = \sigma_b/\sigma_a$ is the key factor to describe how correlated the noise is and how much better the matched-model fitting can do comparing to the least-square fitting. The bigger α is, the more the correlation of the noise would be and therefore the better the matched-model fitting can improve from the least-square fitting. For arbitrary number of samples n , this statement should also be true. Though the general expression of $f(x_1, x_2, x_3, \dots, x_n)$ wasn't found, we figured out a way to calculate $f(x_1, x_2, x_3, \dots, x_n)$ with computer program if n and α are known as described in appendix A. If we define the variance suppression factor of the matched-model fitting to be the ratio of the two amplitude variances obtained by the matched-model fitting and the least-square fitting, the performance of the matched-model fitting is shown in figure 2.9. As plotted, if α is very small, the correlation in noise can be ignored, so the matched-model fitting performs the same as the least-

square fitting. However, with α becoming bigger and the correlation getting stronger, matched-model fitting can be more than 5 times smaller variance than the least-square fitting. Though in this calculation, the baseline is zero. In real experiment, there is always some baseline and it can't be exactly determined. Therefore, we added baseline evaluation in the calculation and because of the additional parameter, the performance of the matched-model fitting was degraded.

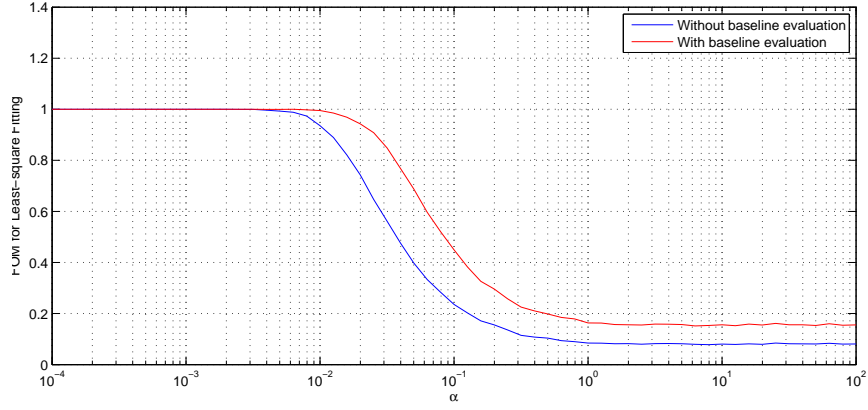


Figure 2.9: The change of the variance suppression factor of the matched-model fitting as a function of the variance ratio α . The noise here is simulated through equation 2.47. The signal waveform is the average signal obtained on a charge collecting pixel in detector # 3E2, which has 160 sample points.

To measure the variance ratio α , we can investigate the j.p.d.f. of any two sample points. However, in our experiment the ADC precision is relatively poor comparing to the amplitude of each noise sample. So that we have to calculate the difference between the mean of two groups of m samples points wat are spaced by k points to evaluate α .

$$M_1 = \frac{1}{m} \sum_{i=1}^m x_i \quad (2.56)$$

$$M_2 = \frac{1}{m} \sum_{i=m+k+1}^{2m+k} x_i \quad (2.57)$$

With simple derivation, it can be known that the variance of $M_2 - M_1$ is

$$\text{Var}[M_2 - M_1] = \frac{2}{m} \sigma_a^2 + \left[\frac{2}{m^2} \sum_{i=1}^m i^2 + (k-1) \right] \sigma_b^2 \quad (2.58)$$

By varying k and m , we can obtain σ_a and σ_b . Figure 2.10 shows how the variance of $M_2 - M_1$ changes with k and m . As shown, all the curves have similar slopes, indicating that the model we discussed above is correct. Using linear fitting we can finally obtain $\sigma_a^2 = 46.4$ and $\sigma_b^2 = 0.0794$. Therefore $\alpha = 0.0421$. Figure 2.11 and figure 2.12 shows the performance of the matched-model fitting. As plotted, matched-model fitting can provide the best signal-to-noise ratio.

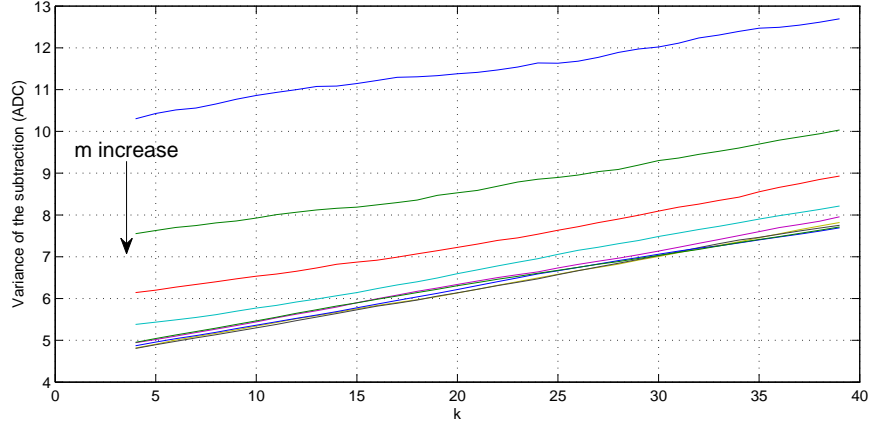


Figure 2.10: The change of the difference between the mean of two groups ($\text{Var}[M_2 - M_1]$) versus the length of the mean m and their spacing k . For different m , the slope of those curves are similar, which matches with the expectation of equation 2.58, indicating the model we used for the noise is correct.

2.5 Conclusion

This chapter introduces the origin and contribution of the electronic noise in the semiconductor detector system. The feature of the electronic noise in our system is studied. Different traditional filters are tested. It is found that for the charge-

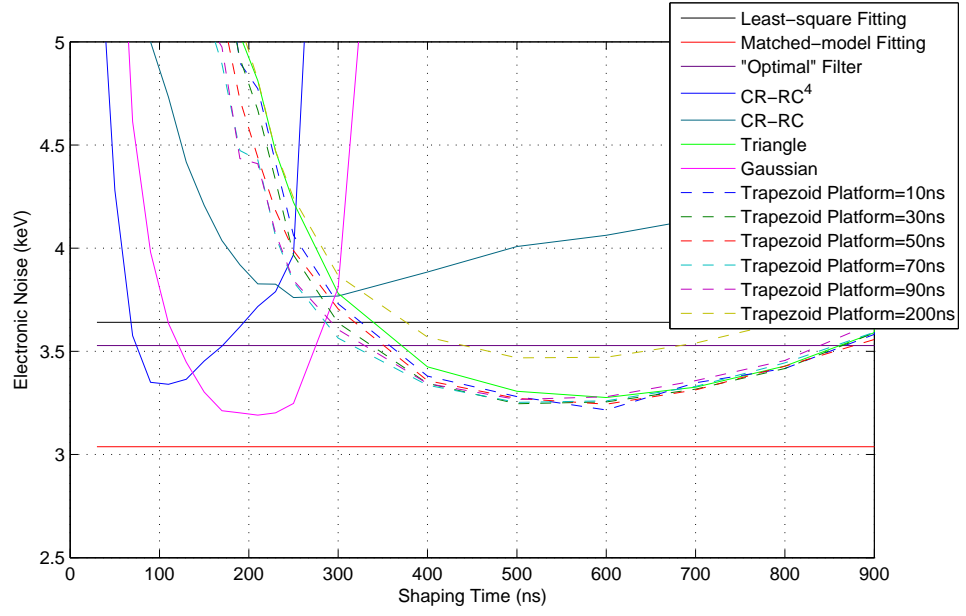


Figure 2.11: Filter performance for charge-collecting pixel signals. The data is obtained on detector # 3E2 with cathode biased at -2500V and grid biased at -30V.

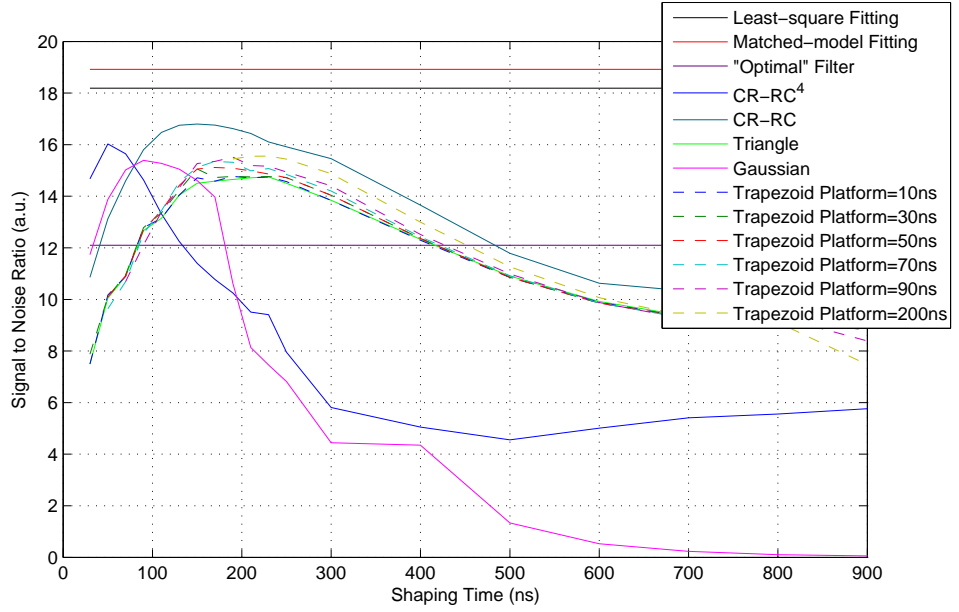


Figure 2.12: Filter performance for neighboring pixel transient signals. The data is obtained on detector # 3E2 with cathode biased at -2500V and grid biased at -30V.

collecting pixels, trapezoid filter or subtraction method is the best filter, while for the neighboring pixels, CR-RC filter is the best one.

A new fitting method is introduced in this chapter with the consideration of the correlation of the electronic noise. Better performance of this new fitting method is demonstrated using experimental data.

CHAPTER III

System Simulation

3.1 Introduction

A simulation was performed to find expected preamplifier output pulse waveforms. These simulated waveform results are then to be used to develop and optimize the sub-pixel position estimation techniques for experimental data. The simulation package includes two components: charge transport and induction, and electronic noise.

3.2 Simulation Software

3.2.1 Geant4

Geant4 is a C++ package designed by the European Organization for Nuclear Research (CERN) to simulate particles interacting with materials. It is widely employed in the fields of high energy physics, astronomy, medical physics, home security etc. We used this package to simulate the interactions between gamma rays and detectors within an energy range of 0 to 3 MeV, which by Geant4 standard is in low energy range.

The detailed distribution of energy deposition for each interaction, including tracking of the ionization path of the recoil electron (which is also referred as an electron cloud) is obtained through the simulation. Charge sharing effect is a very impor-

tant phenomenon in our detectors, especially for multi-pixel-triggered events. This is because the size of the electron cloud (around $300\text{ }\mu\text{m}$ at 662 keV) is not negligible comparing to the pixel size of our detectors (pixel pitch size is 1.72 mm), especially when the recoil electron energy is high. The multi-pixel-triggered Compton events are used to track the source location [49], However, charge sharing events can be confused with Compton events. Therefore, it is necessary to include the electron cloud simulation in Geant4 to study the impact of the charge sharing effect. To do so, we set the threshold of electron tracking to be as small as 3 keV , corresponding to a $1\text{ }\mu\text{m}$ range. With this threshold, the simulated electron cloud should have a precision of $1\text{ }\mu\text{m}$. The gamma-ray threshold is also set very low, at about 1 keV ($1\text{ }\mu\text{m}$ range) such that characteristic X-rays and bremsstrahlung radiation are included. Multi-pixel-triggered events caused by those low energy gamma rays are studied and compared with charge sharing events and Compton events. [Jaechon paper, Weiyi thesis]

Figure 3.1 shows an example of a parallel beam hitting the 18-detector array. Figure 3.2 shows the electron tracks for several different energy. As shown, as the electron energy increasing, the length of the tracks gets longer and the orientation becomes more correlated with the initial direction of the electron. Figure 3.3 is the plot of the average electron cloud size as well as the variance of the size, as a function of energy. Here, electron cloud size is defined as the largest distance between any two points in the electron track. At 662 keV , the electron size is about $250\text{ }\mu\text{m}$.

3.2.2 Maxwell

To simulate the charge drifting behavior inside detectors and calculate the induced signal on the electrodes, the computation of the electric field is necessary. We use a numeric software called Maxwell by Ansoft to perform the computation and obtain the solution for operating electric field and weighting field. Operating electric field is the

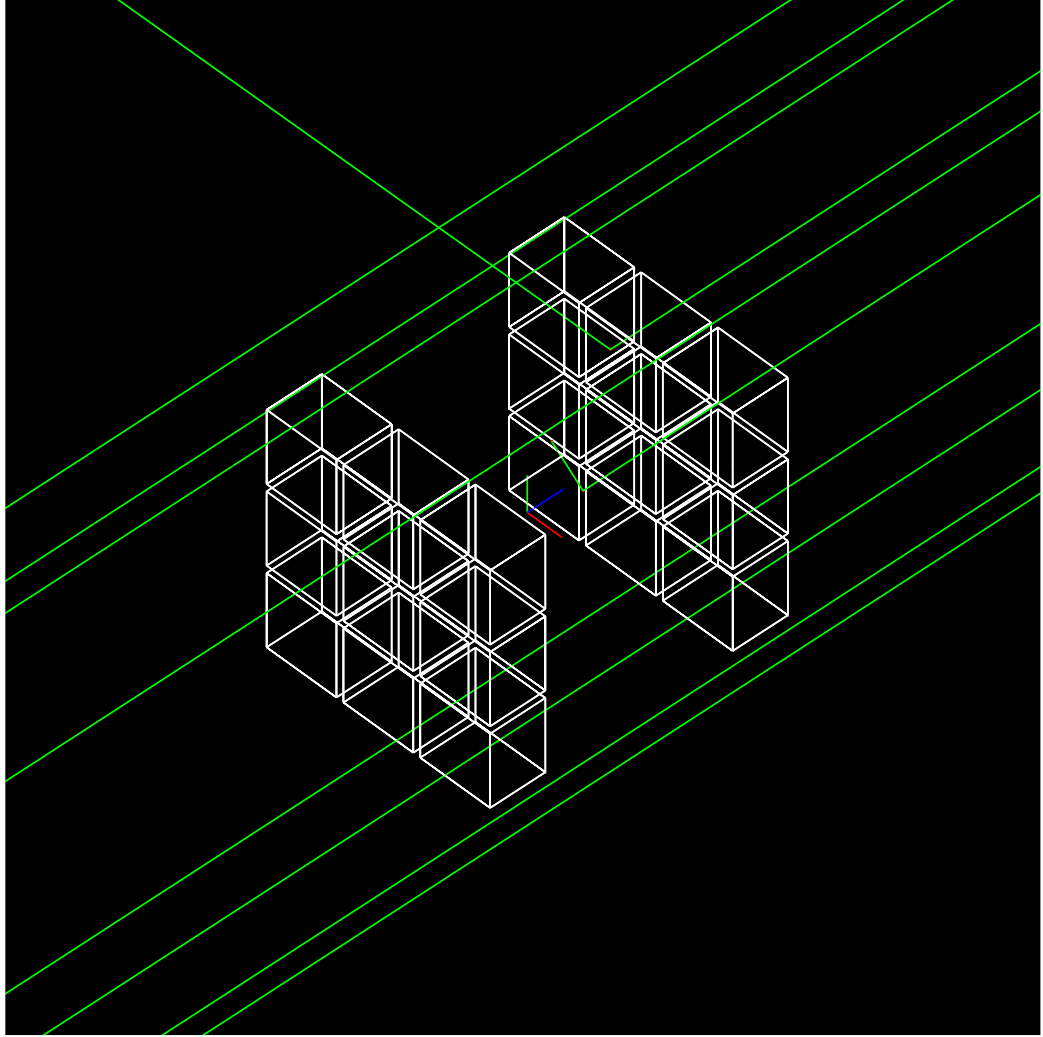
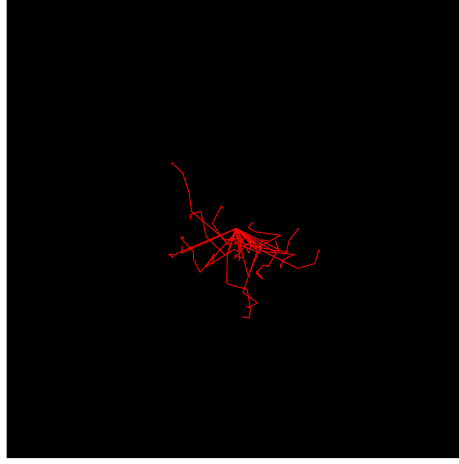
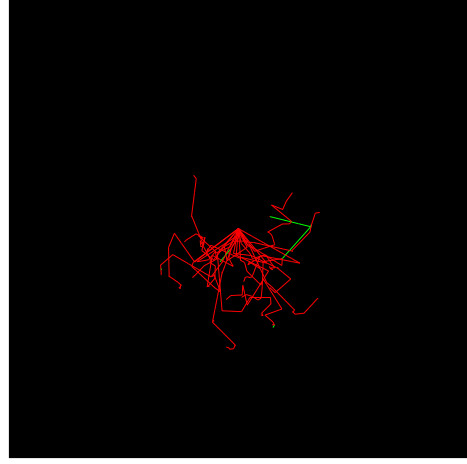


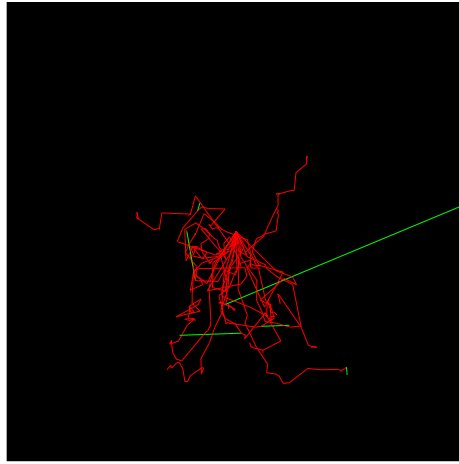
Figure 3.1: This plot shows the Geant4 simulation of the 18-detector array irradiated by a parallel beam of 662 keV.



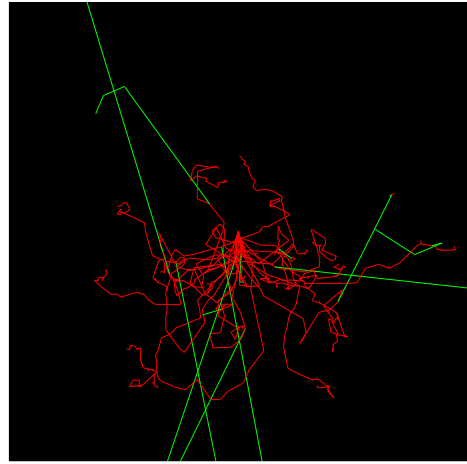
(a) 184 keV, Zoom \times 32



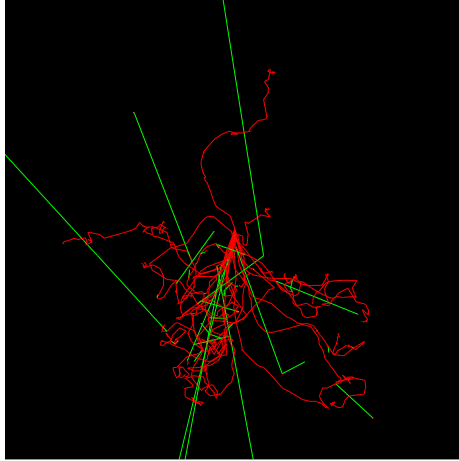
(b) 356 keV, Zoom \times 16



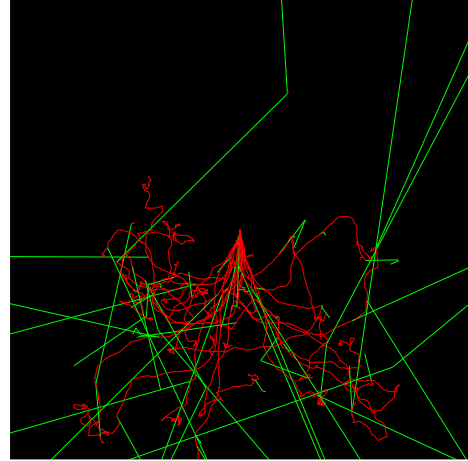
(c) 662 keV, Zoom \times 8



(d) 1460 keV, Zoom \times 4

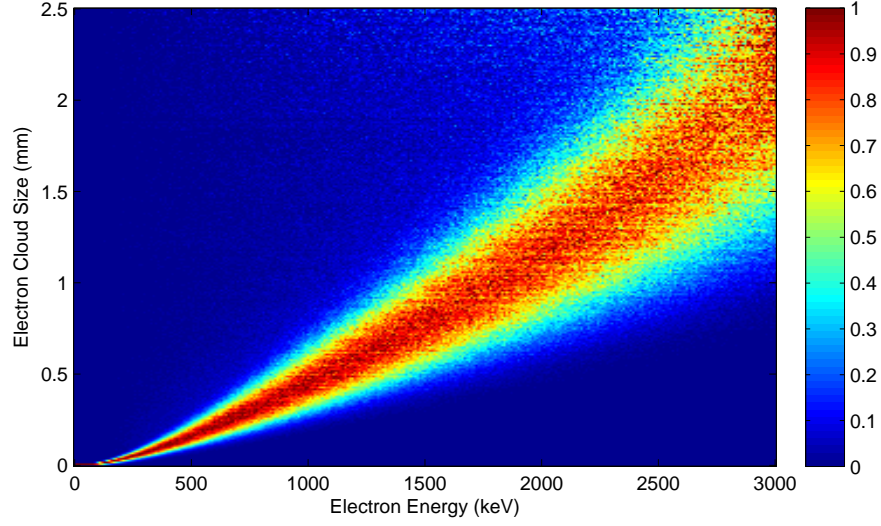


(e) 2615 keV, Zoom \times 2

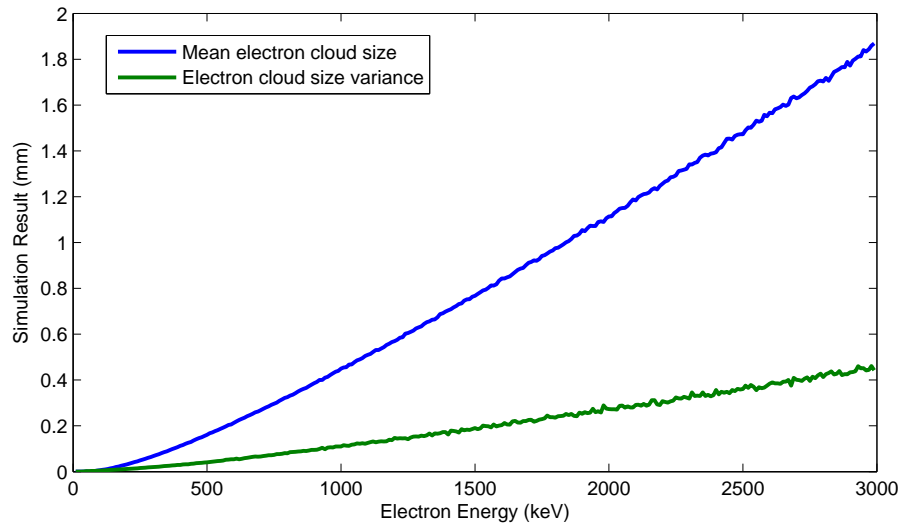


(f) 6000 keV, Zoom \times 1

Figure 3.2: Accumulated tracks of 20 electrons, which are located in the same position and emitted toward the same direction in each case (perpendicularly downward). The blue lines are from gamma rays and the red lines are the electron track.



(a) Electron cloud size distribution



(b) The mean and variance of electron cloud size

Figure 3.3: Electron cloud size distribution in the energy range from 0 to 3 MeV. This result is obtained from Geant4 simulations. The electron cloud size is defined as the largest distance between any two points in the electron track.

true electric field inside the detector when the cathode and grid are biased. Weighting field is a virtual field to help calculate the induced signals on each electrode [12].

The operating electric field is very similar to a uniform field in detector bulk. However, in the anode vicinity, since the grid needs to be biased at a different voltage from the anode pixels, the operating field gets complicated. As discussed in the introduction, the grid is used to steer electrons toward the pixels to help fully collecting charge. If the grid is left grounded as the pixels, charge will be collected on the grid. However if the grid is biased at a negative voltage, electrons will be steered away from the grid. As the grid voltage becomes more negative, more charge will be steered to the pixels. There is a critical voltage above which all electrons will be driven away from the grid. This effect is shown in Figure 3.4. As illustrated, -60 V is the optimal grid bias, which is consistent with what we have observed through experiments.

Weighting field [12] is the electric field when the electrode of interest is set at 1 V and the others are set at 0 V. Figure 3.5 shows the potential for the weighting field (weighting potential) of the central pixel. Note that the colorbar is in log scale. We choose log scale because the weighting potential drops very fast from the pixel of interest. The weighting potential drops to about 1/10 at a distance of just one pixel away. When the distance increasing to several pixels, the weighting potential is only about 1/100. However, the energy resolution of our detector system is below 1%. Therefore, though the weighting potential is very weak, its influence on induced signal amplitude still need to be considered.

3.3 The Signal Induction

Charge induction on a given electrode can be calculated using the Shockley-Ramo theorem [12]. An example was demonstrated [17] to tell how to calculate the charge induction on electrodes. A simulation procedure applied for pixelated CdZnTe detectors is described in detail by Kim [25]. This section uses a similar simulation method.

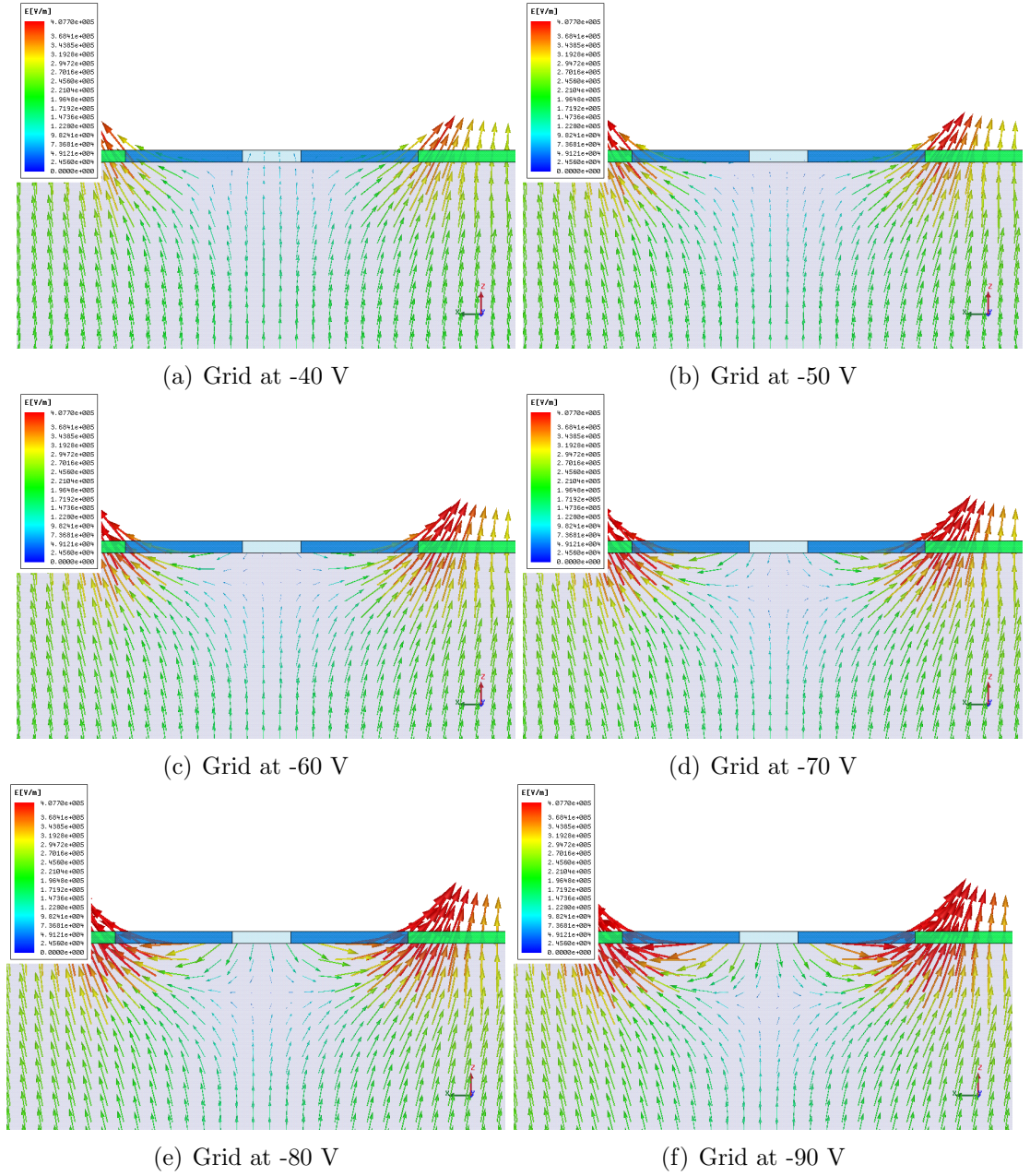


Figure 3.4: These plots show the electric field change with the grid bias. The length of the arrow is proportional to the electric field strength and the arrow-head shows the opposite direction of the electric field to illustrate the electron drift path. The light blue rectangle-shaped electrode is the grid, and the green one is the pixel. This result is obtained with a 3-D Maxwell simulation for a $20 \times 20 \times 15 \text{ mm}^3$ CdZnTe detector. The cathode is biased at -3000 V and the grid at -40 V, -50 V, -60 V, -70 V, -80 V, -90 V respectively.

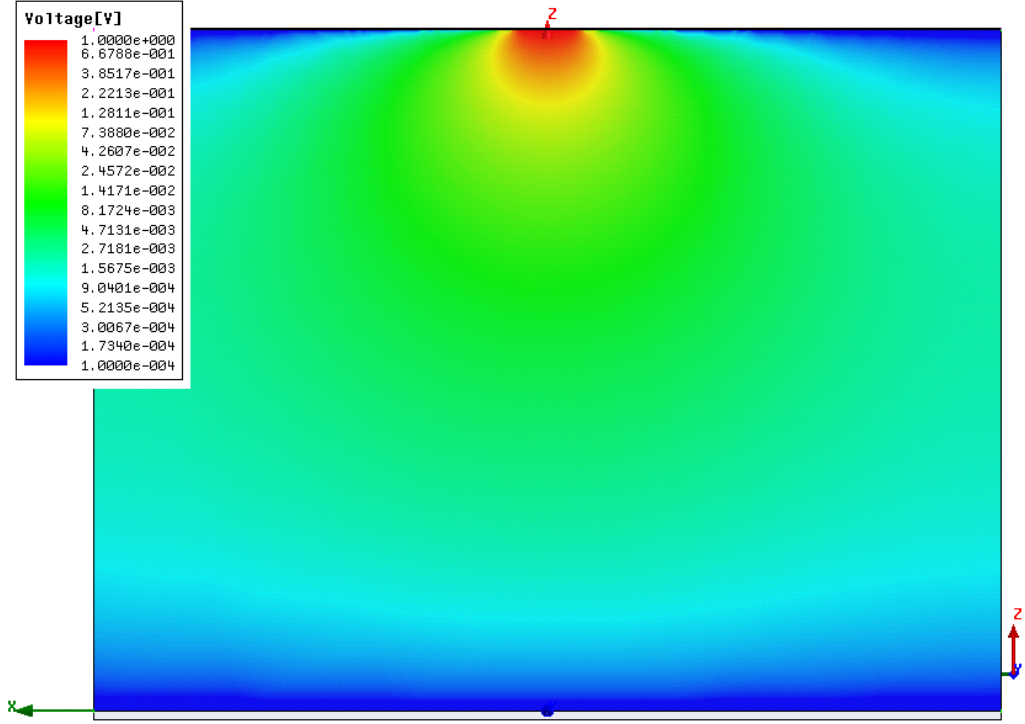


Figure 3.5: The weighting potential distribution for the center pixel (with a red dot on it). This result is obtained with a 3-D Maxwell simulation for a $20 \times 20 \times 15 \text{ mm}^3$ CdZnTe detector.

A simple description of the method is given in the following paragraphs.

The track and velocity of electrons and holes are determined by the operating electric field in the detector. It is assumed that electrons and holes follow the electric field lines in CdZnTe detectors. Of course electrons move toward the opposite direction of the electric field. When holes reach the cathode surface, they are simply collected by the cathode. However, When electrons reach the anode surface, electrons are assumed to be able to move further along the surface from the grid to the anode pixels if the grid is biased. If the grid is not biased, electrons are assumed to stay at the same position as they reach the anode surface.

The induced charge on each electrode is calculated from the weighting potential along each charge track. The final induced signal at time t is then equal to the product of the charge quantity and the difference in weighting potential between the charge carriers position at time t and its initial position.

Figure 3.6 gives an example of the simulated waveform signal induced on a center collecting pixel as well as the pixels surrounding it. The operating and weighting fields are computed by Maxwell 3D v11. In this example, each electron cloud is modeled as a geometrical point with a total charge equivalent to the energy deposition of a 662-keV photon. Two electron clouds are simulated in this figure, one is located at the center of the collecting pixel (thick line) and another is near the pixel edge (dashed line). They both originate in the middle depth of the detector. For this simulation, the cathode bias is -3000 V. Because the mobility of holes is much lower than that of electrons, only the electron drift is simulated during the charge collection time. The trapping of electrons in the detector is not modeled as it is not a critical factor in this study, which will be discussed in Section 5.4.

The signal induced on the center collecting pixel is very small in the detector bulk until the electron cloud drifts to the vicinity of the pixelated anode. In this anode region, the induced signal rises rapidly due to the large gradient in weighting potential,

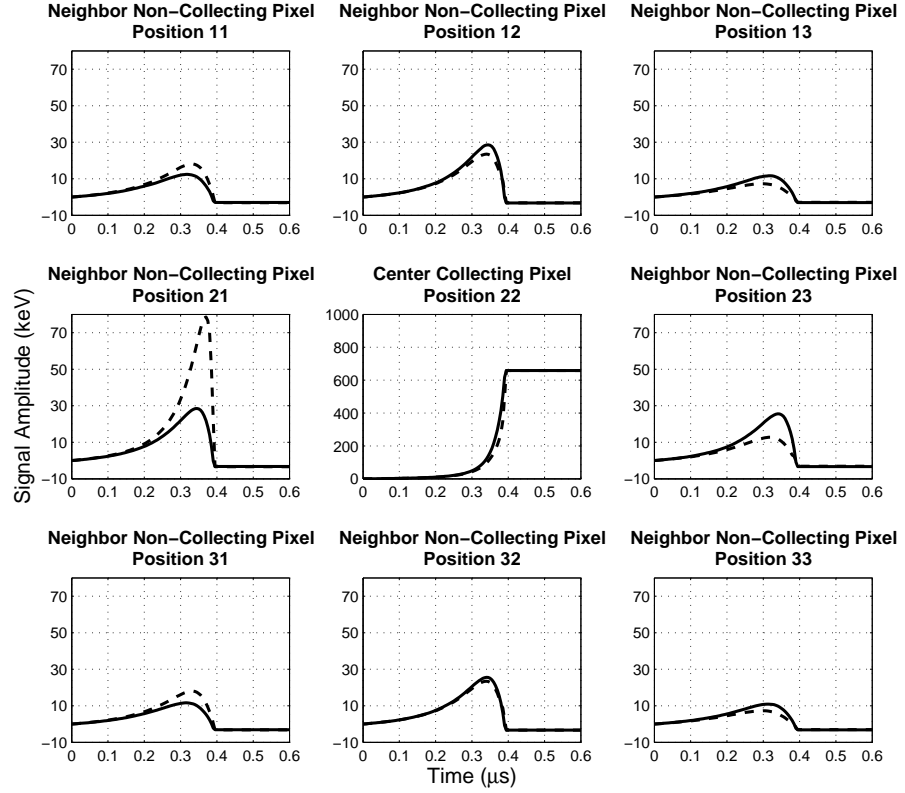


Figure 3.6: Signal induction for a collecting pixel (pixel 22) and its 8 neighbors. The responses correspond to a single simulated 662-keV point electron cloud collected by the center pixel. The transient signals of the neighbor pixels are shown for two events: one occurring underneath the center (thick line) and the other near the edge (dashed line) of the collecting pixel. They both originate in the middle depth of the detector.

and eventually it will rise to an amplitude close to the original 662 keV. There is a small amplitude deficit due to the trapped holes in the detector bulk. Similarly, electron trapping can contribute to the deficit of the induced signal amplitude.

For the non-collecting neighboring pixels, the signal first rises as the electron cloud travels from the detector bulk to near the anode surface and then drops when the electron cloud enters the anode region. The boundary of the anode region is defined as the depth where the “transient signal” reaches a maximum value, roughly one pixel pitch away from the anode surface. Eventually, the signal will drop to zero or to a negative value (hereafter referred as a “negative tail”) due to trapped holes. The amplitude of the negative tail depends on the depth of the initial interaction. When the interaction happens at the cathode surface, the neighboring pixel signal will drop to zero. If the interaction occurs in the detector bulk or in the anode region, the negative tail occurs. The negative tail is the largest when the interaction happens at the anode region boundary.

The peak signal amplitude of the neighboring pixel’s transient waveform is very sensitive to the lateral position (or sub-pixel position) of the interaction position. As seen in Figure 3.6, the induced signal on the neighboring pixels changes significantly when the electron cloud moves from the pixel center (the thick line) to the edge (the dashed line). As was mentioned earlier, the transient signal reaches its maximum when the electron cloud is roughly one pixel pitch away from the anode. At this time, the lateral distance from the electron cloud to the center of a neighboring pixel ranges from half a pixel to one-and-a-half pixels for interaction location on one edge of the collecting pixel. As a result, the total 3-D distance from the electron cloud to a neighboring pixel at the transient peaking time strongly depends on the lateral position of the electron cloud at that time. Therefore, the peak amplitude of the neighboring transient signals actually gives the lateral position where the electron cloud enters the anode region.

An interaction location is the starting point of an electron cloud trajectory. If an electron cloud trajectory is a straight line perpendicular to the cathode and anode surface, the neighboring transient signal peak amplitudes would be directly related to the initial lateral interaction position. However, the electron cloud trajectory can be bent due to grid bias or material defects. The impacts of those factors on neighboring pixel transient signals are different. The grid bias is used to help improve charge collection efficiency and it is normally very small compared to the cathode bias. Its impact on an electron cloud trajectory is negligible before the electron cloud gets very close to the anode surface, so the initial interaction position can still be obtained by the neighboring transient signals. As for material defects, they can alter an electron cloud trajectory significantly when the electron cloud is still in the detector bulk. In this case, the neighboring pixel transient signals won't be able to provide initial interaction positions.

If a detector crystal is of very good quality and is free of material defects, we can use the peak amplitude of the transient signals to determine the sub-pixel position of an interaction. However, as we can see in Fig. 3.6, the transient signals are quite fast and have very small amplitude compared to the charge collection signal. Electronic noise is expected to be the limiting factor in how accurately we can determine the sub-pixel interaction position.

3.4 Electronic Noise Simulation

Pullia and Riboldi [39] provided a method to precisely simulate the electronic noise of a detector system in the time domain. As discussed in section 2.1.1.2 the noise power spectrum density function can be written as

$$S^2 = a^2 + b^2/\omega^2 + c^2/\omega. \quad (3.1)$$

Where S^2 is in unit of keV^2/Hz and ω is the circular frequency. a , b and c are required to performance the noise simulation. If using a CR-RC^{*n*} shaping, we can obtain a curve showing the noise amplitude changing with the shaping time. This curve should follow equation 2.23 when the shaping time is much smaller than the time window of the data. Then, a , b and c can be obtained as discussed and demonstrated in section 2.1.1.2.

However, in simulation, we did not consider 1/f noise. The reason is that 1/f noise is small in our system compared to parallel and serial noise as already shown in section 2.1.1.2. Additionally, in terms of searching for the optimal filter, existence of 1/f noise will not make much difference as shown in Figure 2.7. For example, triangle filters are better than CR-RC⁴ no matter how much 1/f noise exists. Lastly, the simulation of 1/f noise requires calculation of erf function, which is very time consuming.

3.5 Conclusion

This chapter presents the method to perform a complete simulation of the whole system. The gamma-ray interactions are modeled by Geant4 and the electric field is modeled by Maxwell. The induced signal is forged based on the Shockley-Ramo theorem and the electronic noise is simulated using a method provided by Pullia and Riboldi [39]. In the later chapters, we will use this simulation method and compare its results to the experimental results.

CHAPTER IV

UM-VAD ASIC and its Readout System

4.1 Introduction

Modern semiconductor detectors utilize specialized electronic system for data readout, which is called Application Specified Integrated Circuit or ASIC. For past ten years, we have been collaborating with Gamma Medica-Ideas for designing ASICs for pixellated 3-D position sensitive CdZnTe detector array system[ref polaris project]. We have successfully designed one generation of ASIC which we name as VAS_TA. Those VAS_TA ASICs are capable of readouting the signal amplitude as well as the drift time of each electron cloud for each pixel. So that energy and 3-dimensional position be obtained for each interaction of multi-pixel events, which make it possible for a single detector to produce a 4-PI image of radiation sources through Compton imaging. However, thereif are still lots of limitation in these ASICs. For example, if a Compton event has two interactions happened in a single pixel, VAS_TA ASICs won't be able to distinguish them. Additionally, the crosstalk on the neighboring pixels can produce fake signals in VAS_TA ASICs, which can't be distinguished only knowing signal amplitude and drift time. Those fake signals can become very significant when the energy deposition is high. As mentioned in chapter V, pre-amp waveforms carry very rich information of the history of charge carriers drifting. Therefore we worked together with Gamma Medica-Ideas again and developed a new ASIC (UM_VAD as

we call it) which is capable of digitalize and output the pre-amplifier waveforms. This UM_VAD ASIC carries lots of potential and it will help to further explore the capability of CdZnTe detectors. This chapter introduce the basic performance of the UM_VAD ASIC. Chapter VI and chapter VII will present its performance and some of its applications.

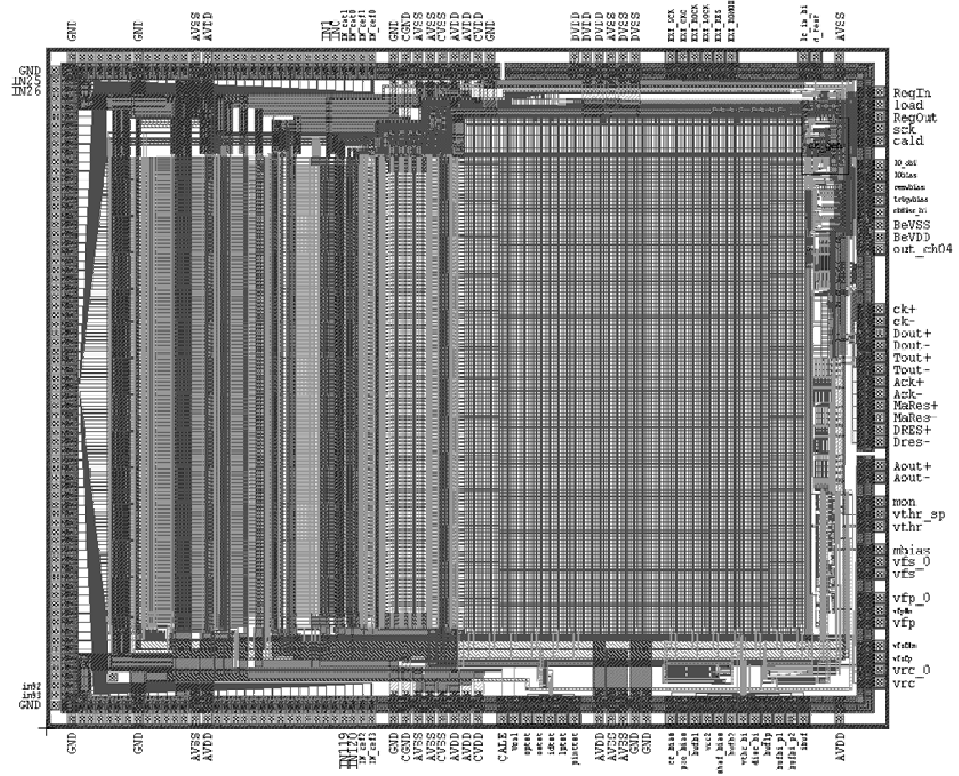


Figure 4.1: The layout of the UM_VAD ASIC.

4.2 UM_VAD ASIC

4.2.1 Overview

UM_VAD ASIC is a 124-channel pipeline circuit with charge-sensitive pre-amplifiers. It is designed to provide the information of per-amplifier signal waveform instead of just signal amplitude and timing information. In the same time it will achieve a dynamic range of 3 MeV with low electronic noise of about 2 keV and low power con-

sumption around 2 mW per channel. The last version of the first iteration UM_VAD ASIC (UM_VAD v1.2) has all the designed functions working and its performance is close to the specification.

The 124 ASIC channels include 1 reference channel for baseline monitoring, 1 cathode channel, 1 grid channel and 121 anode channels for 121 pixels as shown in figure 4.2 ¹. Each channel is consisted of a charge-sensitive pre-amplifier, a anti-aliasing filter and 160 sample-and-hold storage cells. The pre-amplifier signals are continuously sampled and stored in the 160 cells sequentially and circularly at a frequency up to 80MHz until a readout sequence is initiated. At that time, all the cells will have their values hold unchanged. After the readout is ended, the ASIC will continue the sampling process and wait for another one. The readout sequence is controlled outside of the ASIC. It can be initiated anytime and can be irrelevant to any external triggers. This feature provides us a way to measure the baseline and the electronic noise of the system precisely at anytime. Of cause, in normal data acquisition, readout sequences are issued in response to the external triggers. There are two modes of readout: full readout and sparse readout. In full readout, all 124 channels are output as long as one pixel has a trigger; in sparse mode, only those those channels who are have triggers or whose neighbor is triggered will be readout. Those modes will be discussed in detail in section 4.2.2.

Additionally, to produce clean triggers, the output of every pre-amplifier is fed into a noise-reduction fast filter. This filter has small time constant so that the delay from the start of the event and the trigger is small. Following the filter is a discriminator which can be adjusted by users to further tune the threshold pixel by pixel. Usually, the system will be triggered when any pixel has a signal passing the threshold after shaped by the fast shaper. The cathode and grid are designed not being able to trigger the system independently to avoid abnormal triggers. Since cathode and grid

¹This plot is provided by Gamma Medica-Ideas

have relative large area, their electronic noise is much larger than anode pixels and they are [vulnerable] to interference. Those shortcomings make it easy for cathode and grid to produce fake triggers.

This ASIC also provides several special functions which will be discussed in section 4.2.5.

4.2.2 Data Acquisition

This section describes the working sequence of UM_VAD ASIC responding to an gamma-ray interaction in a pixellated CdZnTe detector.

UM_VAD ASIC is running sampling continuously in a round-robin manner. When a UM_VAD ASIC is power on and the main clock signal is fed in by the readout system, it starts to sample the pre-amplifier signals no matter if there is any trigger or not. The round-robin manner is a method to sample infinitely long signals with limited number of buffer units. Those buffer units are called cell in our ASIC. We have 160 cells for each channel. In round-robin way, samples are stored in cells one by one until they reach the the last one, the 160th cell. At this moment, the sample storing will be turned around and restart from the 1st cell. The values stored in the old cells will be wipe out. Therefore, the newest cell is the one just refreshed and the oldest cell is the one next to it. From the oldest cell to the newest one, the 160 adjacent cells contain the 160 samples of a waveform. The system keeps a record how many rounds it has rewound and which cell is currently under refreshing. This information will be stored in a 16-bit global variable and used as the time stamp of the event, which will be output during readout. The sampling frequency is controlled by the main clock generated by the FPGA in the readout system. Additionally, ASIC itself can slow down the sampling frequency to $1/2$, $1/4$ and $1/8$ of the main clock frequency. Currently, UM_VAD ASIC works at 80 MHz. With 160 sampling cells, it can capture the signals as long as $2\ \mu\text{s}$.

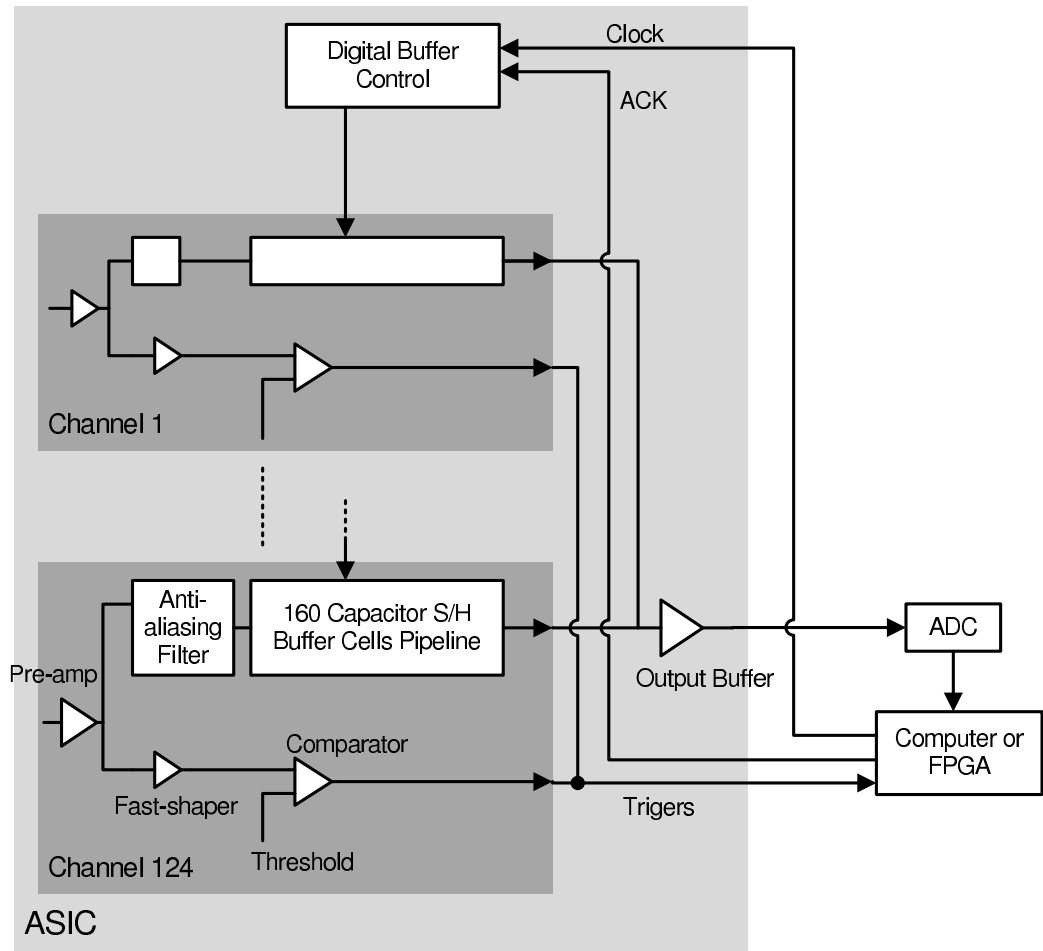


Figure 4.2: This figure is an illustration of the ASIC functionality. Each ASIC has 124 channels. Among them, channel 1 is a reference channel for baseline monitoring, channel 2 is grid channel, channel 3 is cathode and channel 4 to channel 124 are anode pixels. Each channel has its own pre-amplifier followed by an anti-aliasing filter and a block of 160 analog buffer cells for sampling and store pre-amplifier output. The output of the pre-amplifier is also routed to another path going through a fast shaper and a comparator to produce clean triggers. The ASIC main clock, which is also the sampling clock, is generated by an external system, which normally is a FPGA. This FPGA monitors the trigger signal from ASIC and determines if a readout sequence needs to be initiated. By assert the ACK control line, the FPGA can start a readout sequence at any time.

When an interaction happens, signals are induced on cathode and anodes. Each UM_VAD ASIC anode channel has a fast filter and a comparator. When an electron cloud reach anode, a trigger is generated in the ASIC. This trigger is an internal signal and not visible to the readout system. At the trigger time, the charge collecting may haven't been completed yet. Therefore, the ASIC will keep sampling for certain amount of time, which is called hold-delay time, to ensure complete acquisition of charges for every event. When hold-delay time is reached, the ASIC will stop sampling and hold the amplitudes on all cells. At this time, an outgoing trigger, which we call as Tout, will be generated to inform the FPGA the completion of the signal sampling. The ASIC will wait for the reply of the FPGA for certain amount of time, which we call reset delay time. If there is no response received from the readout system, The ASIC will reset itself. All trigger information will be cleared and the state machines will be reset. Figure 4.3² shows the diagram of the signal flowing.

The response of FPGA to the ASIC is the acknowledge signal, or ACK signal. FPGA can send ACK signals at any time. They may not necessarily be the response to triggers. For UM_VAD ASICs, as long as they receive a ACK signal, the amplitudes of the cells will be held when ACK gets asserted and a readout sequence will start when the asserted ACK is released. Therefore, the baseline of the ASIC can be obtained by sending ACK signals in absence of triggers. This method can be used for debugging, calibration or electronic noise measurement. We call this working mode internal trigger mode. On the other hand, if FPGA only responses to the ASIC when there is a trigger, we call the system working in external trigger mode.

When ACK signal is asserted, the amplitudes of the cells of a UM_VAD ASIC will be held and kept unchanged as long as the ACK signal isn't released. If there are multiple ASICs having triggers, by asserting the ACK signals, we can readout the data of one ASIC while keeping the data of the others untouched. In each readout

²This plot is provided by Gamma Medica-Ideas

sequence, the ASIC will continue to output data until all flagged channels are read or dreset is set high. For each channel all 160 hold capacitors will be read, starting with the one that contains the oldest sample. The readout frequency can be $1/4$ or $1/8$ of the ASIC sampling frequency or ASIC main clock. The first analog value of a channel is valid on the second cycle of the readout clock and then the next on the following cycle. Therefore it takes 161 cycles of the readout clock to read one channel, which is 644 and 1288 ASIC main clocks for the readout clock as $1/4$ and $1/8$ ASIC main clock respectively.

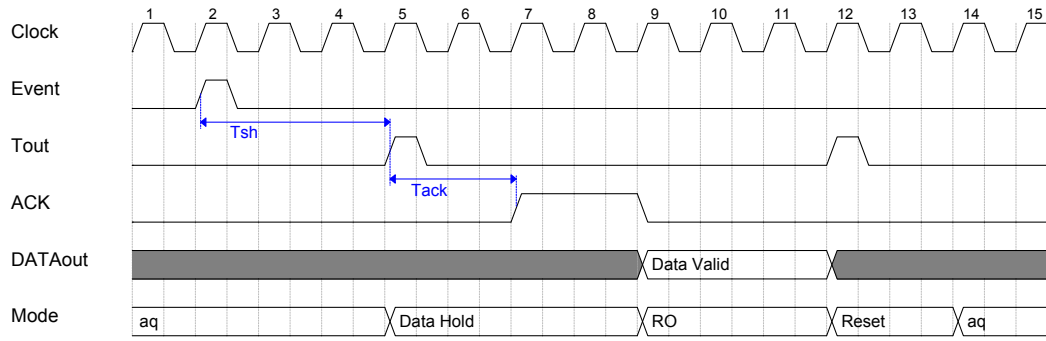


Figure 4.3: The timing diagram of UM_VAD ASIC. The external signals "Clock", "Tout", "ACK", and "DATAout" are shown for a typical operating sequence of the ASIC when an event happens. The acquisition of signals (or "aq"), data readout (or "RO"), and reset are marked. The number of clock cycles shown here is for an illustration. In real operation, it is difference and it changes with the different modes the ASIC is operating in.

UM_VAD ASICs can work in either full readout or sparse readout mode. In full readout mode, all channels are readout as long as one of them is triggered. In this mode, the signals induced by an electron cloud on all 121 pixels can be examined. We can then determine the crosstalk between any two pixels using only single-pixel-triggered events. In addition, with sub-pixel position sensing, we can even determine the crosstalk in sub-pixel scale and provide better calibration for multi-pixel-triggered events especially for neighboring-pixel events, for which, crosstalk plays a critical role in energy reconstruction.

However, full readout requires a large amount of data to be streamed out of the system, which limits the count rate. The highest count rate in full readout was measured to be around 200 count per second. This count rate is too low for real operation. Therefore, sparse readout function was designed and implemented in UM_VAD ASICs. In sparse readout, ASIC can output up to 9 channels for each triggered channel: the triggered channel and its 8 neighbors. Obviously, the crosstalk between two pixels with the distance greater than one pixel can't be determined in this mode. Therefore, full readout can be run for a calibration purpose while sparse readout can be used for routine operation.

4.2.3 Cell Pedestal Calibration

The pedestal of each cell can be calibrated in internal trigger mode with all channels being readout (full readout) as described in section 4.2.2. This calibration should be done without any detector attached to reduce electronic noise as much as possible. The calibration procedure is simple in theory and is consisted of two steps: (1) We acquire certain number of waveforms in internal trigger mode for every channel with no signal on its pre-amplifier. The acquired waveforms should be the samples of zeros and therefore the output of the cells can tell their pedestal. (2) We average the acquired amplitudes for each cell to reduce the uncertainty caused by electronic noise and obtain the pedestal.

However, there is some crosstalk found between hold signal and pre-amplifier signal, which makes the calibration more complicated in reality. As talked in 4.2.2, in internal trigger mode, the amplitudes on the cells will be held as soon as the ASIC receives an ACK signal. However, the hold signal itself can introduce some interference on the pre-amplifier signal and it happens before holding procedure is completed. As a result, there would be some cells that are made enabled for sampling at that moment have their amplitudes changed to the interfered signal instead of their

true pedestal. Which cells are influenced depends on when the FPGA issues the ACK signal. The ASIC provides a function in internal trigger mode that user can specify on which cell FPGA should issue an ACK signal and start a readout. We call this cell readout start cell. In fact, we found the interfered cells include the readout start cell and several cells before it. Therefore, in real operation, we will need to first specify one cell as the readout start cell and perform the pedestal calibration for the un-interfered cells. Then we change the readout start cell and calibrate the pedestal for those cells previously having interference. [more discussion?]

4.2.4 ASIC Performance

4.2.4.1 Power Consumption

Power consumption of a ASIC is a critical parameter. It first determines how much cooling power is required to keep the system temperature in the operation range. Second, it defines how portable the whole detector system can be. For temperature, as we know high temperature will cause high electronic noise and it can also make the system unstable. Especially, for Polaris project, it is consisted of an array of 18 detectors with 18 ASIC chips. All those 18 chips need to be packed in a small space to make Polaris portable. Therefore, a small amount of power increment for one ASIC would result in significant amount of additional heat generated by the packed 18 chips. As for portability, if the ASIC power is low, it would be possible to have the whole detector system running on battery, which is the ultimate goal of Polaris project.

The power consumption for UM_VAD ASIC was targeted at 1.5 mW per channel. We made a measurement of the current which flows into the FEC board between the Vdd, Vss power rails and the ground in the GM-I system when it is acquiring data at 80 MHz to calculate the power consumption. Table 4.1 shows the result.

	Voltage(V)	Current(mA)	Power(mW)
Vdd	+1.50	36.6	54.9
Vss	-2.00	-74.9	149.8
Ground	0	38.5	-
Total		-0.2	205.7
Power per channel			1.65

Table 4.1: The power consumption of the GM-I system when it runs at 80 MHz

4.2.4.2 Linearity

Figure 4.4³ represents the linearity of the system measured with the internal test pulse of the ASIC. The system used in this measurement is GM-I 80 MHz system. Since there is lots of extra electronic noise in the test pulse (the test pulse peak is measured to be about 20 keV FWHM though the electronic noise of the system is only 3 keV FWHM), this linearity measurement has big uncertainty. Therefore, we can only estimate the limit of the system linearity. The maximum nonlinearity is below 50 ADC number for whole dynamic range as shown in the figure without considering measurement uncertainty. Previous experiments have shown that 1200 ADC number is corresponding to about 662 keV, which gives about 5400 ADC number as 3 MeV. If we use the maximum difference from the linear fitting divided by the dynamic range to quantify the nonlinearity, the system non-linearity should be less than 0.9% for 3-MeV dynamic range. Additionally, if we use 2nd-order polynomial fitting to find out the trend of the measured differential linearity, the nonlinearity of the system can be estimated to be around 10 to 20 ADC number, which is about 0.2 to 0.4% nonlinearity.

We also evaluated the system linearity using gamma-ray sources on 40MHz system with detector 3E-2. A simple waveform processing algorithm (simple subtraction) of calculating the difference of the 64-point averages before/after the transient of the signal was used to extract the pulse amplitude. The reconstructed photopeak centroids

³This plot is provided by Cassarah Brown, University of Michigan

are shown in figure 4.5⁴, together with the difference between the true gamma energy and the reconstructed energy. The results show that overall the VAD_UM ASIC has excellent linearity, especially below 1 MeV. For higher energy, the reconstructed energy tends to be larger than the true energy. The maximum deviation from the best fit is 20keV at 2.6 MeV, giving about 0.7% nonlinearity for 3-MeV dynamic range. However, at high energy, the electron cloud size is large and thus some of charge may be lost to the neighboring pixels, resulting in physical nonlinearity. Therefore, the electronic nonlinearity is expected to be less than 0.8%, which agrees with the test pulse result.

4.2.4.3 Electronic Noise

The test pulse injected into the UM_VAD ASIC is generated in the readout system. It has very large extra noise so that the electronic noise of the ASIC can't be measured with the test pulse. With the capability of reading out the baseline in internal trigger mode, the electronic noise can still be accurately measured by investigating the baseline fluctuation after signal processing procedures, such as filtering and signal fitting.

Figure 4.6 is a histogram showing the measured baseline fluctuation in internal trigger mode for channel 40 of detector # 3E2 with the detector biased at -2500 V and the grid at -30 V. The amplitude of the baseline is obtained by using simple subtraction, which is equivalent to the trapezoid filter. The FWHM of the peak is 5.8 channels. ¹³⁷Cs 662-keV gamma-ray line is measured to be located around at channel 1200. Then the electronic noise is calculated to be 3.2 keV. The common mode noise is subtracted which is discussed in section 4.4.

With detector attached and biased, the electronic noise in the system will increase. Figure 4.7 shows the electronic noise changing with the setup. The contribution of

⁴This plot is provided by Feng Zhang, University of Michigan

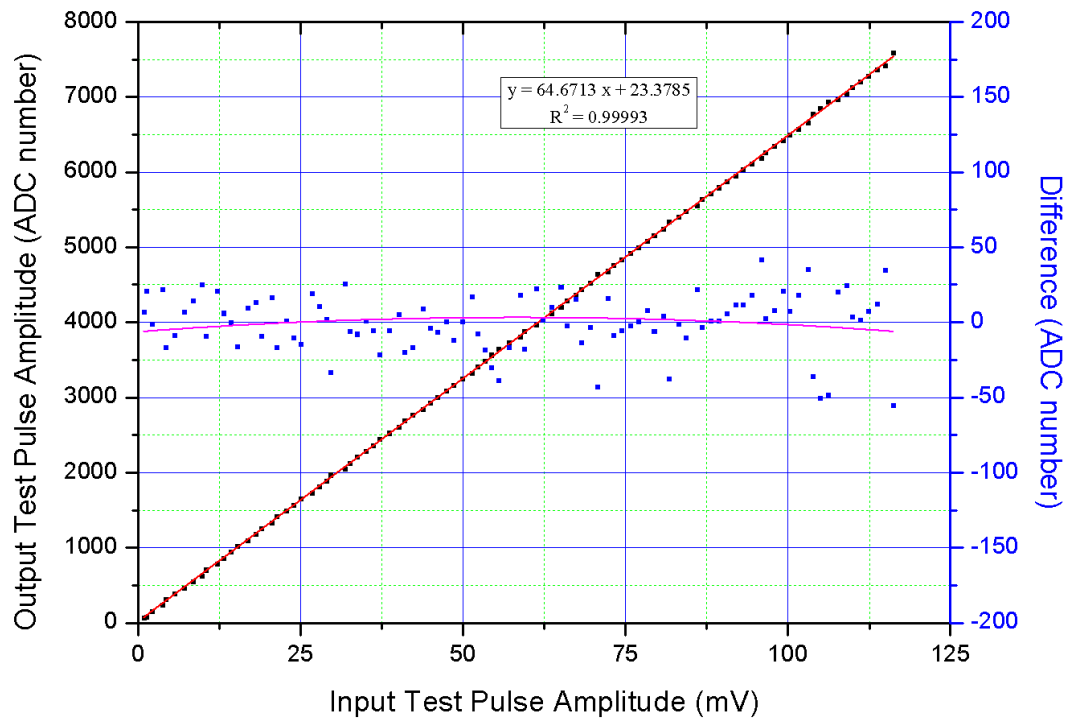


Figure 4.4: Integral (black dots) and differential (blue dots) linearity (the difference between the linear fitting and the measurement) of the VAD_UM ASIC in the ASIC dynamic range measured with the internal test pulser. The linear fitting to the integral linearity is presented as the red line and the 2nd-order polynomial fitting to the differential linearity is presented by the magenta line.

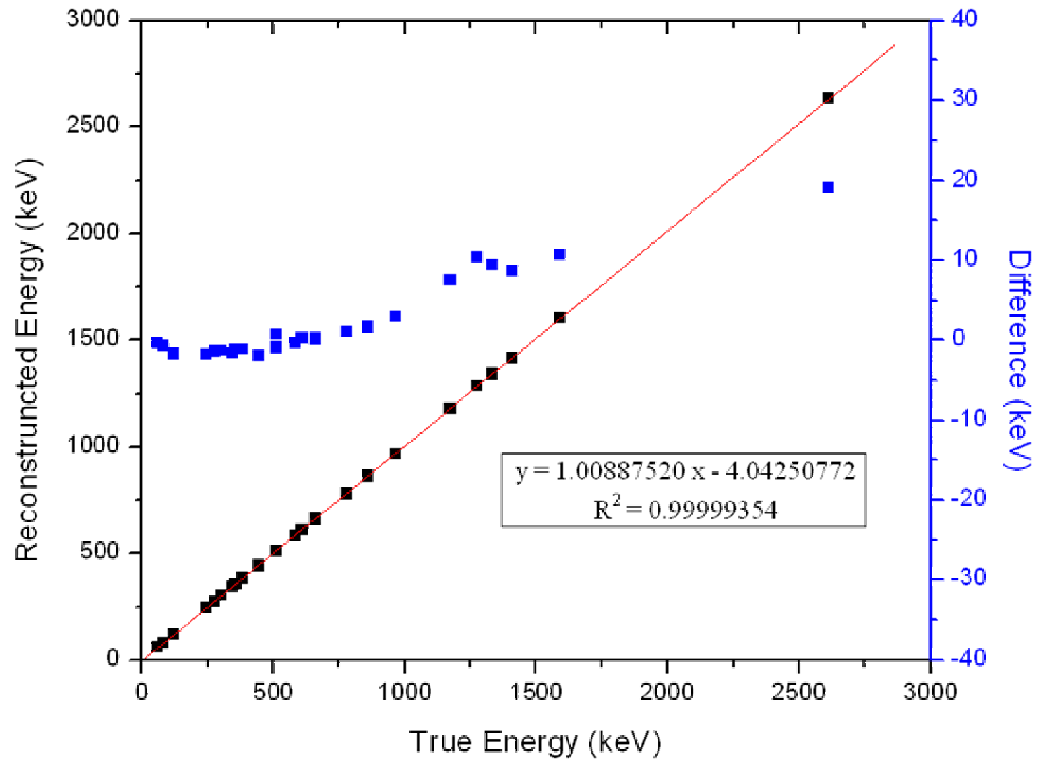


Figure 4.5: Integral (black dots) and differential (blue dots) linearity (the difference between the linear fitting and the measurement) of the VAD_UM ASIC from 60 keV to 2.6 MeV measured with radiative sources. The linear fitting to the integral linearity is presented as the red line.

each factor can be seen in plot. For cathode channel, the most contribution of the electronic noise comes from the capacitance of the cathode bias board (HV board). The cathode capacitance is another very important contributor. Surprisingly, the leakage current is found to play an insignificant role in this case. For anode pixels, the anode capacitance, grid-to-anode leakage (bulk leakage) and cathode-to-anode leakage (surface leakage) all play important roles. Among them, the pixel capacitance is found to be the most important one. For a good pixel, such as channel 83 as shown in the figure 4.7, either bulk leakage or surface leakage won't contribute significantly to the electronic noise.

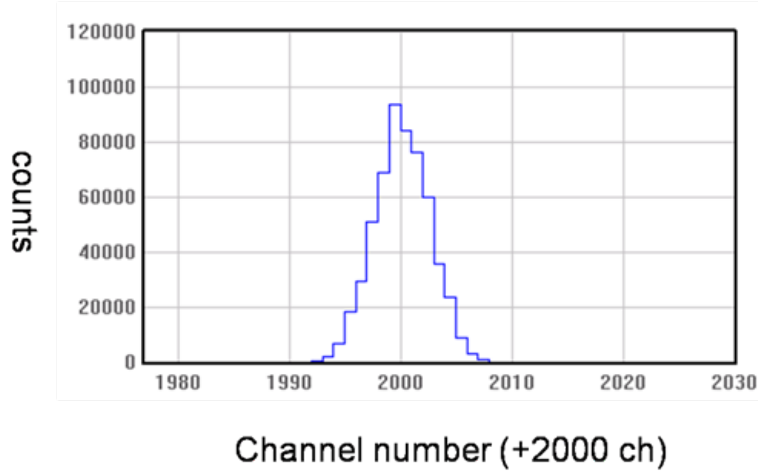
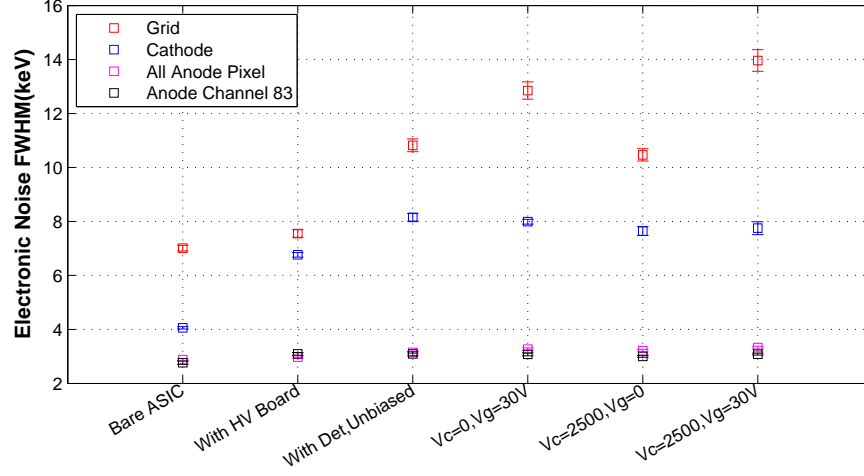


Figure 4.6: The fluctuation of measured baseline. The amplitude is obtained using subtraction method. The data is obtained for channel 40 of detector # 3E2, which is biased at -2500 V on the cathode and -30 V on the grid.

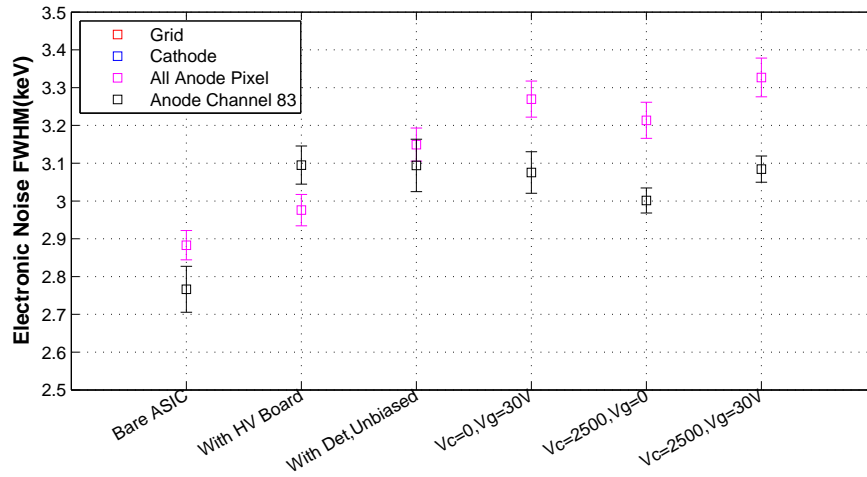
4.2.5 Special ASIC Functions

4.2.5.1 Frequency Change Mode

The frequency change mode is designed to solve the conflict between the sampling time window length and the sampling frequency. To capture the transient behavior of induced signals, the sample frequency needs to be high. But to capture the complete information of the event, the length of the sampling time window needs



(a) Grid and Cathode



(b) Anode Pixels

Figure 4.7: The measured electronic noise changing with the setup. The detector used here is detector # 3E2. V_c and V_g are cathode bias and grid bias respectively. HV board is the cathode bias board. Channel 83 is the pixel that has the best energy resolution. The leakage current on this pixel should be low.

to be sufficiently long. There are only 160 cells for each channel, so that these two requirements can't always be satisfied.

For example, if the electron drift time is 750 ns, the time window is required to be at least double the drift time, namely $1.5\ \mu\text{s}$. The reason is for multi-pixel-triggered events, when one electron cloud triggers the system, the cathode signal has up to 750 ns rising edge before the trigger and the anode waveforms from the other electron clouds can delay as long as another 750 ns. Additionally, the baseline data before the interaction happens and the tail data (the flat part of the signal after the charge is collected) are necessary to determine the signal amplitude. If we use a filter of $1\ \mu\text{s}$ peaking time, the tail needs to be $1\ \mu\text{s}$ long. Then the totally time window needs be at least $2.5\ \mu\text{s}$ long even if the baseline is ignored, which is longer than the $2\text{-}\mu\text{s}$ time window 160 cells can store when the system runs at 80 MHz. Lower the sampling frequency to 40 MHz can solve the problem. However, the measurement on the neighboring pixel transient signals will be less accurate.

The frequency change mode provides a method to avoid this conflict. It can slow down the sampling frequency to a half after certain amount of time when the ASIC receives a trigger. Therefore, the length of the signal tail can be extended. For the example discussed above, $1\ \mu\text{s}$ tail can be sampled when the sampling frequency is slowed down to 40 MHz, which only requires 25 cells to store. Since the $1.5\ \mu\text{s}$ time window requirement due to drift time only cost 120 cells at 80 MHz, there are still 15 cells left which can be used for the baseline.

However, the frequency change mode increases the difficulty of signal processing since the samples are acquired at different frequencies. Additionally, if the drift time caused time window requirement is too long, such as $1\ \mu\text{s}$, the changing sampling frequency method can't help to completely acquire the signal waveforms.⁵

⁵Dr. Feng of University of Michigan proposed another solution, which is to double the number of storage cells for the cathode channel so that the drift time caused time window requirement will be the drift time itself instead of the double of the drift time.

4.2.5.2 Slope Trigger Mode

The slope trigger function was designed to only acquire the photopeak events so that both calibration data size and time can be reduced. As talked in section 4.2.1, UM_VAD system can only be triggered by anode signals. In slope trigger mode, those anode triggers need to be validated by the cathode slope. Only when the cathode slope is bigger than the threshold the anode signals can trigger the system. Since the cathode slope is proportional to the energy deposition, photopeak events can be selected in the slope trigger mode.

4.3 Readout System

Our readout system is an electronic and data interface for UM_VAD ASICs. It provides the power and the clock signal (ASIC main clock) to the ASIC and it transfer the data ASIC acquired to the host computer. Our readout system has two key components, the front end board (or FEC board) with ASICs bonded on it and the motherboard having FPGA and ADC to control the ASICs and perform data manipulation and transportation. The FEC boards have detector connectors on them for detectors to be attached on. The inputs of the 124 channels of a UM_VAD ASIC are connected to the electrodes of a detector through those detector connectors. The power, clock, test, data and control pins of the ASIC are routed out and connected to the motherboard by a plugin connector, So that the FPGA on the motherboard can configure the ASICs.

During readout, the ASIC streams out two sets of data: (1) the digital data containing the information of each channel included in the readout and (2) the pipeline data which is actually the analogue current signal proportional to the pre-amplifier amplitude samples stored in the cells and.

The digital data contains the coordination of each output channel and its trigger

flag. It is serially output to the FPGA one bit every readout clock. The format of the digital data is listed in table [digital data format]. The function of this digital data is to tell the identity of those readout channels. In full readout mode, the digital data isn't necessarily required since the channel number is directly related to the readout index number of this channel. For example, the fourth readout channel is always the anode channel #1. (The first three readout channels are always reference channel, cathode and grid for full readout and sparse readout mode since they all needed to be output no matter which readout mode the system is in.) However, in sparse readout mode, the fourth readout channel can be any one of the 121 anode channels. Therefore, it is required to use digital data to tell the channel number of each readout channel.

The pipeline data is output on a differential current buffer. The range of the buffer is approximately from -500uA to +500uA. This signal is converted to a differential voltage signal on the espresso board before AD conversion. The cathode channel receives charge of different polarity, but the analog data is inverted such that the output polarity becomes the same for all channels. The ADC on the espresso board samples continuously on 1/4 or 1/8 of the ASIC main clock frequency. The ADC sampling frequency can be changed in FPGA. It should match the readout clock to reach optimal performance. Additionally, the ADC clock is also designed be able to be inverted and/or delayed by 25-75 ns to further match the ASIC analog output.

The analog data and digital data for one channel are not synchronized because the analog data needs to go through the AD conversion and it will be delayed for 8 ADC clock cycle. There are two settings in FPGA: ADC data delay for the analog data and ASIC data delay for the digital data, that can be adjusted to synchronize the analog and digital data. In fact, since the analog data is always 8-ADC-clock-cycle later than the digital data, ASIC data delay needs to be 8-ADC-clock-cycle larger than ADC data delay.

During readout, the ACK signal is kept low. The FPGA can issue Dreset to end the readout immediately and clear all the trigger data. When the last channel is read, the ASIC will reset automatically. Old data will still be present in the pipeline for 160 clock cycles after reset.

We have developed two readout systems. One of them was designed by GM-I and it supports up to 4 detectors. The other system was designed together by Space Physics Research Laboratory (SPRL) at the University of Michigan and our group. This system is called DGD-1 and it was originally targeted at supporting 18 detectors. Currently DGD-1 system has finished its first iteration and it can now support a 3 by 3 detector array, totally 9 detectors. The following two sections will present a detailed description of those two systems.

4.3.1 GM-I Readout System

GM-I system as shown in figure 4.8⁶ is consisted of a FEC board, a espresso motherboard, a cROB8s data acquisition board as well as a national instrument digital IO card installed in a host computer. The cROB8s board and the national instrument card work together as the digital data transfer interface between the motherboard and the host computer.

The FEC board in the GM-I system has four ASIC chips wire-bonded on it. The four ASICs share the same configuration line but each of them has its own data path and AD converter chip to minimize the system dead time. The electronic noise introduced by the readout system was measured to below 1 keV FWHM according to GM-I, which is insignificant comparing to the total 3 keV electronic noise of the system.

GM-I system has undergone two versions: 40 MHz and 80 MHz. The 40 MHz system has the ASIC main clock running at 40 MHz instead of 80 MHz in the 80

⁶This plot is provided by Gamma Medica-Ideas

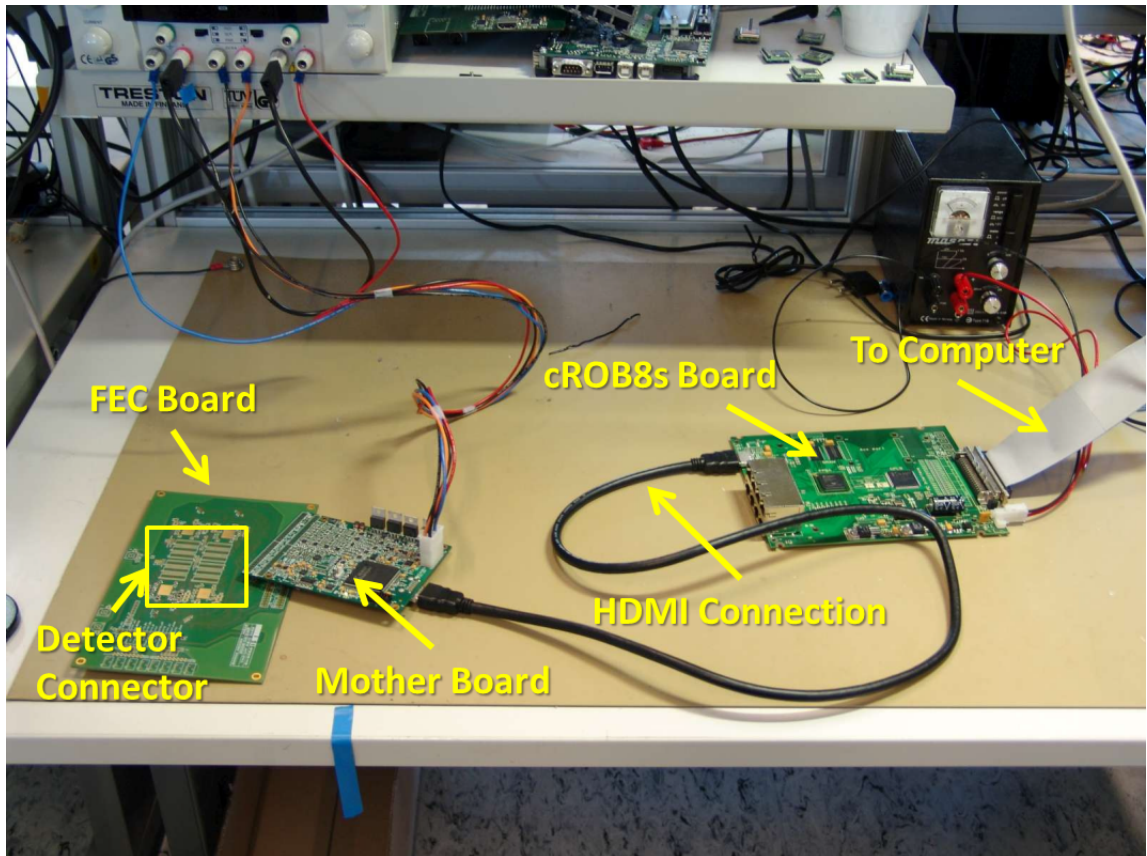


Figure 4.8: A plot of the GM-I system. As can be seen, the FEC board has detector connectors on it and ASICs bonded on the other side. The espresso board is connected through a HDMI interface to cROB8s data acquisition card and then to a national instrument PCI-DIO-32HS card and finally to a host computer.

MHz system. It was designed for debugging purpose. Since the ASIC main clock is fed in by the readout system, the 40 MHz system can be upgraded to 80 MHz by simply changing the FPGA code.

However, the GM-I system only supports 4 ASICs, while our ultimate goal is to develop a system that can handle a detector array with 18 detectors. In addition, the GM-I system requires two hardware components: cROB8s and national instrument DIO card to transfer data between the motherboard and the host computer, which is too complicated and inconvenient. For example, this complicated system is too large to fit into a hand-held system which is our future goal of the project. And the HDMI interface of cROB8s is found vulnerable to external interference. We observed that HDMI cable used for connecting the motherboard and the cROB8s board can pick up interference in air and feedback to the pre-amplifier signals. If the HDMI cable is put in a wrong pose, huge interference can be observed on the pre-amplifier. Additionally, the national instrument DIO card used in the system shows lots of problems during operation. This card can get frozen easily when the data piled up in its memory and requires rebooting of the computer to reset the system. Therefore, we initiated an effort to design a new readout system that supports 18 detectors and has a simpler, more robust and more convenient data transfer interface.

4.3.2 DGD-1 Readout System

DGD-1 system is designed together by SPRL[full name] and our group. Its target is to build a system that can support up to 18 detectors, which has two layers of 3 by 3 detector array. This system follows the basic design of GM-I system. It also has FEC board and motherboard. The difference is a DGD-1 motherboard connects to 3 FEC boards and each FEC board has 3 ASIC chips bonded on it so that one DGD-1 motherboard can totally support 9 detectors. Additionally, USB interface is realized directly on the motherboard for system control and data transfer. Figure 4.9

shows the diagram of the system⁷. It is more convenient and more robust than GM-I system in hardware debugging and practical operation.

For the 3 ASICs on a FEC board, they share the same ADC and configuration line. As a result, DGD-1 system needs more time to readout one event comparing to GM-I system if there are multiple ASICs having triggers. However, the readout time is not the bottleneck that limits the event rate. In fact there is massive amount of data generated for every event. The transfer speed of this amount of data defines what is the event rate that can be processed by the whole system. As mentioned in previous section, the GM-I interface with cROB8s plus NI digital IO card can provide an event rate of 200 events per second in full readout mode. With USB interface, the event rate can theoretically go to 1500 events per second if assuming full transfer speed of USB 2.0 interface, which is 480 Mbits/sec. Currently, we have achieved a transfer speed of 70 Mbits/sec with Cypress USB chips. It is corresponding to 220 events per second in full readout mode, slightly better than GM-I system.

We have performed several tests on DGD-1 system. The motherboard works properly. The electric noise introduced on the motherboard during data transfer from ASICs to ADCs was measured to be less than 1 keV FWHM, which is similar to what we have obtained on GM-I motherboard. However, we found the DGD-1 FEC board is noisier than GM-I FEC board because of crosstalk. One observation we got was the test pulse can induce signals on channel 104(?). Another is the common mode noise. We found in DGD-1 system, common mode noise plays more important role that it does in GM-I system. With deeper investigation, we discovered that the common mode noise in DGD-1 system wasn't uniform from one channel to another. We believe some of the common mode noise should be due to the crosstalk between input channels and control signals. A detailed discuss will be described in section 4.4.

⁷This plot is provided by SPRL

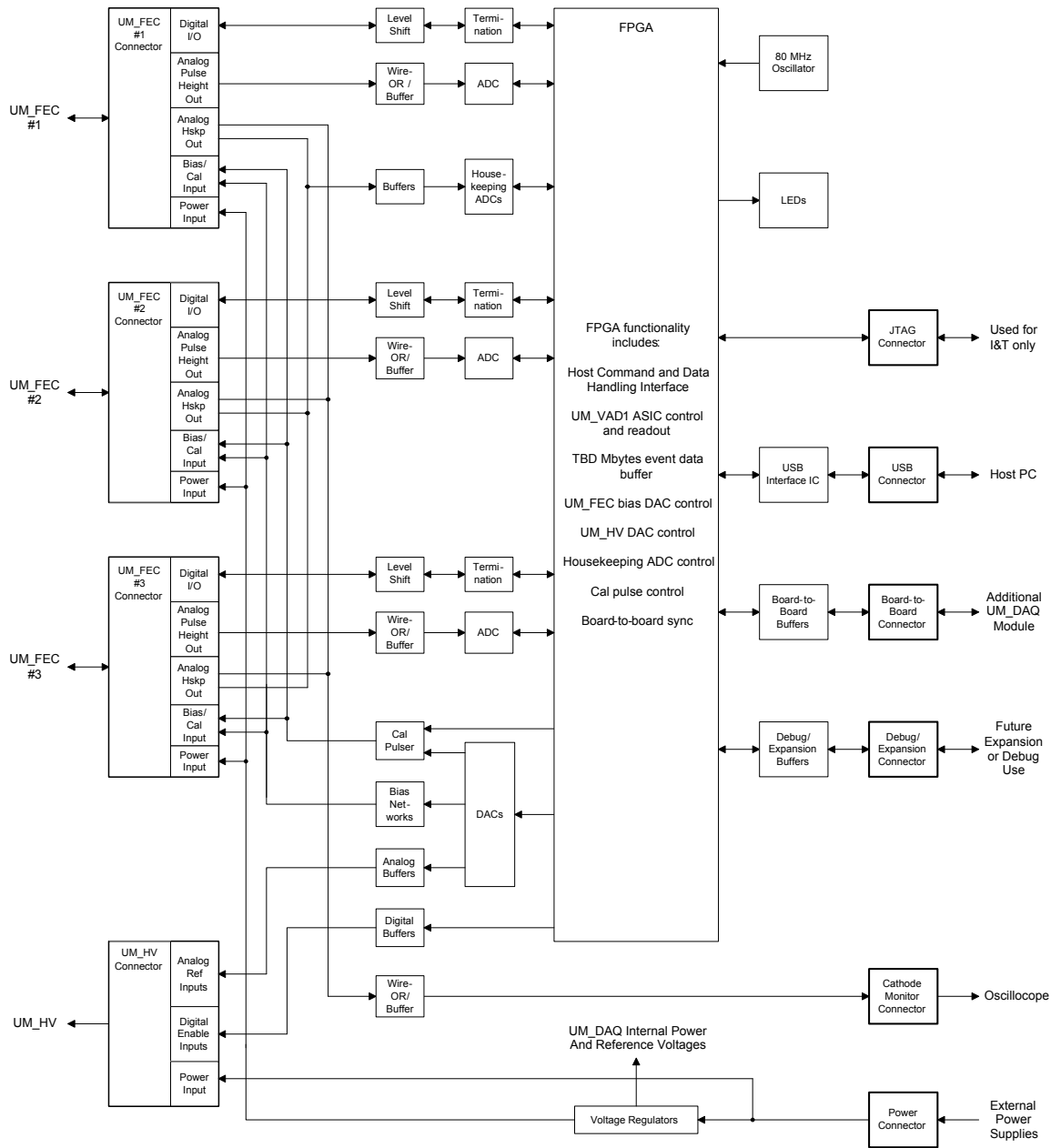


Figure 4.9: the diagram of the DGD-1 system.

4.4 Common Mode Noise

In full readout mode, for singl-pixel-triggered events, there are many pixels having very tiny induced signals, which can be neglected. By simple average the signals measured on those pixels, the common mode noise of the system can be observed. We measured the common mode noise in the GM-I 40 MHz system and 80 MHz system. Two categories of common mode noise were identified the 40 MHz system: high frequency common mode noise (HFCM noise) and low frequency common mode noise (LFCM noise).

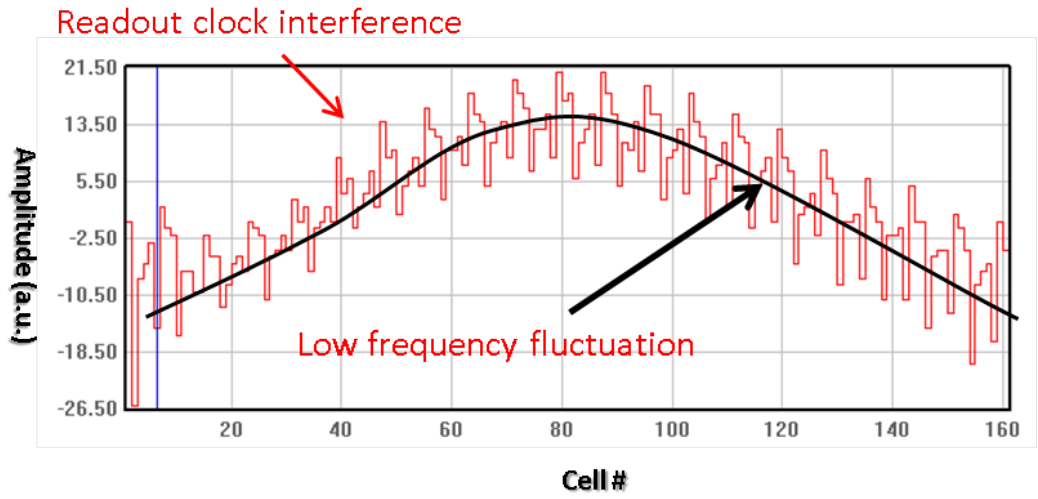
The HFCM noise was found to be correlated with the readout clock. It was suspected that the readout clock line can induce interference on the pre-amplifier output line. If it is running when the sampling is carrying on, the sampled signals will include the interference. In fact, readout clock needs to be enabled only when a readout sequence is enabled when the sampling is already done. Therefore, the readout clock can be disabled during the sampling process and then the HFCM noise can be removed. The upgrading from 40 MHz to 80 MHz of the GM-I system included this correction.

Figure 4.10 shows the measured common mode noise in the 40MHz system and 80MHz system. Both of these plots were acquired at a lower sampling frequency ($1/8$ of the ASIC main clock) in order to observe the LFCM noise clearly. It can be seen that the readout clock interference (HFCM noise) is removed in the 80MHz system, showing the operation to turn off the readout clock during sampling is an effective solution.

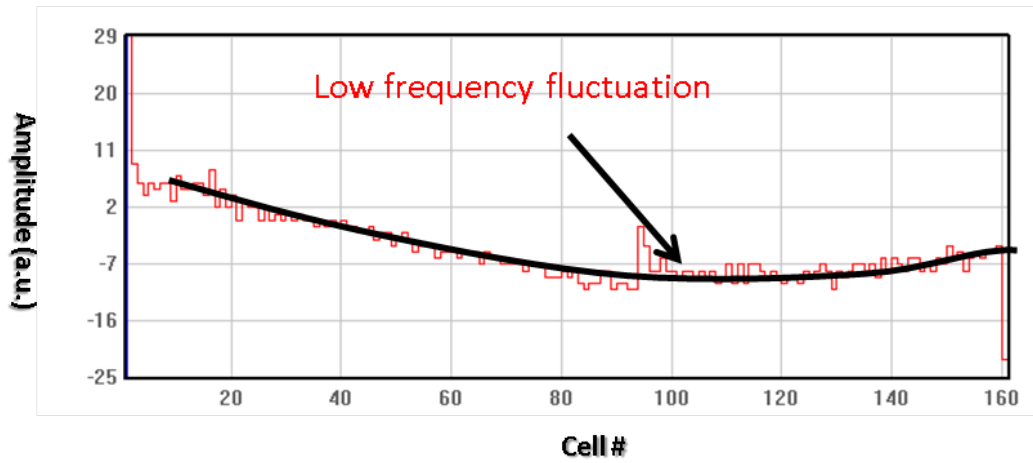
The LFCM noise exists in both 40 MHz and 80 MHz systems as shown in figure 4.10. This slow oscillation of the signal is usually caused by the fluctuation of power supply. An effort was made to filter out the LFCM noise when the power was fed into the ASICs in the GM-I readout system. However, the LFCM noise wasn't totally removed.

In full readout mode, the common mode noise can be calculated. Therefore, common mode noise correction (CMN correction) can be applied by subtracting the measured signal in each channel by the common mode noise. As long as the number of no-signal or weak-signal pixels is large enough that common mode noise can be calculated without much uncertainty, the CMN correction shouldn't introduce extra uncertainty to the system while the common mode noise is totally removed. CMN correction can help to evaluate the influence of common mode noise. Figure 4.11 shows the influence of LFCM noise for 121 anode pixels at different sampling frequency. Changing the sampling frequency can be realized because UM_VAD ASIC can slow down its sampling frequency as mentioned in section 4.2.2. As observed, at low sampling frequency, the total electronic noise is much smaller when CMN correction is performed. However, at 80 MHz, the reduction of electronic noise is small.

As mentioned in section 4.2.2, in full readout mode, either GM-I system or DGD-1 system can only run at 200 events/sec because of large data size. To reduce dead time, the only option is to use sparse readout mode. However, common mode noise can be corrected in full readout mode. Therefore, it is required to have low common mode noise to realize sparse readout. As shown in figure 4.11, in current system, the contribution of common mode noise to the total electronic noise is around 10%. Degradation of performance is expected when the system is running in sparse readout mode. For example, the energy resolution of detector # 3E2 is measured to be 0.78% FWHM at 662 keV using GM-I 80 MHz system. The electronic noise is 3.2 keV after CMN correction. Without CMN correction, the resolution can be estimated to be about 0.81% FWHM at 662 keV. Such a performance degradation is acceptable.



(a) 40 MHz GM-I system



(b) 80 MHz GM-I system

Figure 4.10: The common mode noise measured in the 40 MHz system and the 80 MHz system.

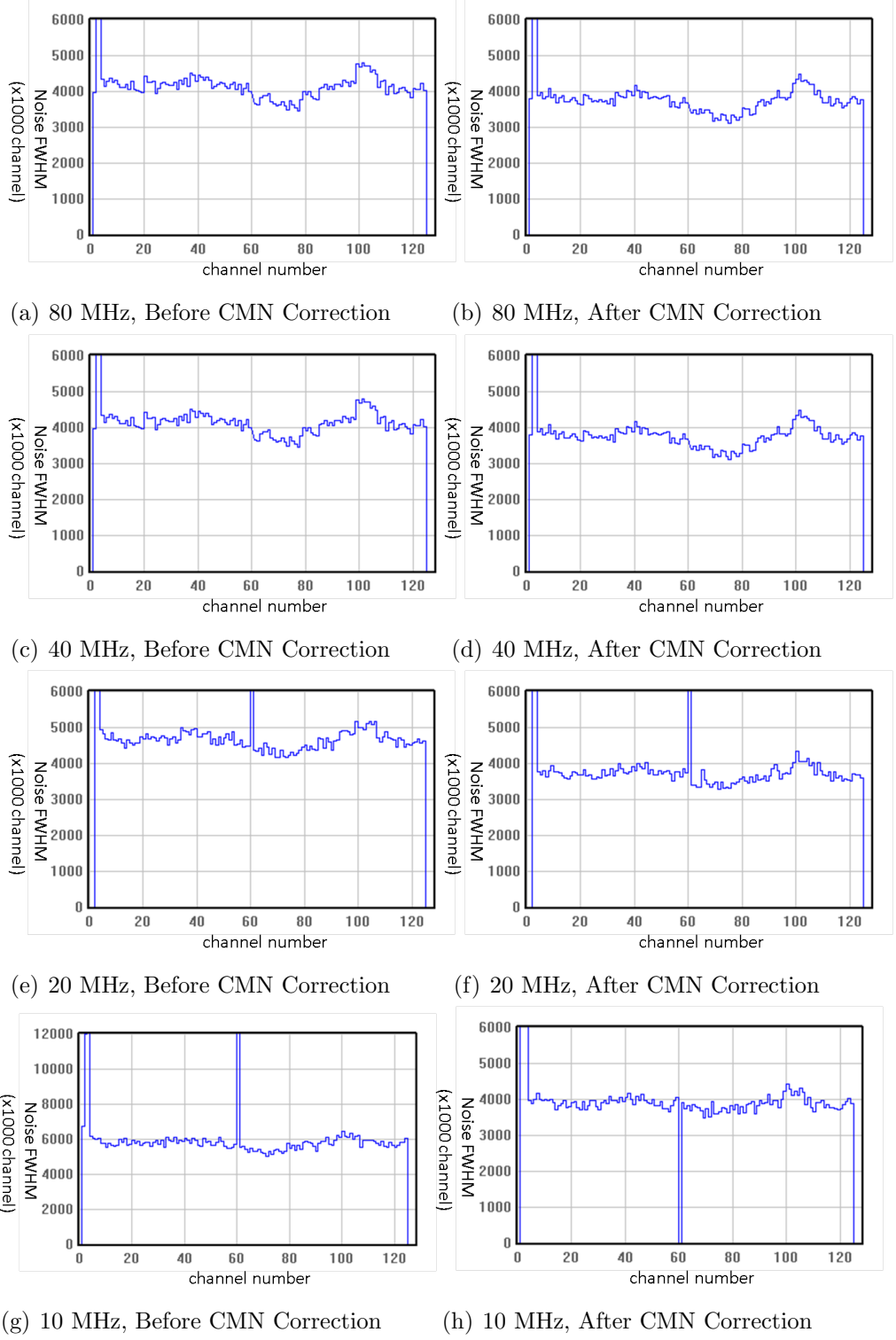


Figure 4.11: The common mode noise measured in the 80 MHz system with the modification to reduce LFCM noise. The common mode noise is measured when the sampling frequency is set at 1, 1/2, 1/4 and 1/8 ASIC main clock frequency.

4.5 Conclusion

In this chapter, we introduced the UM_VAD ASIC and its readout system. This ASIC is designed collaboratively by University of Michigan and Gamma Medica-ideas. It is a very powerful DAQ system because it can produce digitalized pre-amplifier signal waveforms for each event rather than only the signal amplitude and drift time for traditional ASICs. The first version UM_VAD ASICs has been delivered and modified based the test result. Its performance is summarized in this chapter. In general, the UM_VAD ASIC has good linearity and low power consumption. The electronic noise is measured to be around 3 keV. The functions of the ASIC all work as designed. In the future, we would like to further lower the ASIC noise to 2 keV. Currently the BNL ASIC has 2 keV electronic noise [24], which presents the best result we have achieved. With the UM_VAD ASIC improved to 2 keV electron noise, it is expected to produce better results than the BNL ASIC because of the much richer information that can be obtained from the pre-amplifier waveforms.

CHAPTER V

Sub-pixel Position Resolution

5.1 Introduction

As talked in I, our Pixelated CZT detectors are capable of providing 3-D position information of gamma-ray interactions within one detector volume. It is a key performance parameter for Compton imaging applications. The lateral position resolution of CZT detectors using pixelated anodes is currently limited by the pixel pitch. In our present CZT detector configuration, each pixel pitch is 1.72 mm. As a comparison, our depth sensing-techniques provide an interaction-depth resolution of about 0.5 mm [52], much more precise than the pixel pitch. This relatively poor lateral position resolution limits the Compton image angular resolution to roughly 40 degrees FWHM using simple back-projection reconstruction [49].

Better position resolution is desired to improve the angular resolution of gamma-ray imaging reconstruction. A number of efforts have been made in the past decades to achieve position resolution better than the dimension of charge collecting electrodes in semiconductor detectors. Warburton [47], Burks et al. [7] and Williams et al. [48] proposed and demonstrated a method to obtain improved position resolution based on induced transient signals on non-charge-collecting electrodes in striped CdZnTe and HPGe detectors. Marks et al. [30], Vickersa and Chakrabarti [45] and Jakubek and Uher [20] studied several algorithms to achieve sub-pixel position resolution when an

electron cloud is collected by several pixels in pixelated detectors. Narita et al. [32] showed the difference in the transient signals on neighboring non-charge-collecting pixels in pixelated CdZnTe detectors when the gamma-ray interaction position was changed. For our detectors, the pixel size of the anode is 1.72 cm as mentioned above. It is bigger than or similar as the electron cloud size in the energy range of 0 to 3 MeV, the dynamic range of our detector system [25]. Therefore, the charge-sharing sub-pixel position determination method discussed in [30, 45, 20] can't be applied. The transient signal method mentioned in [7, 48] is promising. As mentioned in [32], the induced transient signals on the neighbor pixels change with electron cloud location. However, since the area of a pixel in our detectors is much smaller than the area of the anode strip in [7, 48], the induced transient signals on the non-collecting electrodes are expected to be much smaller in our case. Therefore, it is challenging to implement the transient signal method in our pixelated detectors.

This chapter describes the first detailed study on a sub-pixel position calculation algorithm based on non-charge-collecting transient signals [7, 48] for pixelated CdZnTe detectors. First, a detailed simulation to generate the signal pulse waveforms expected from the detection system is presented. Next, several sub-pixel position calculation algorithms are proposed for single-pixel events, which, combined with results from simulations, provides the theoretical limit on the best achievable position resolution as a function of electronic noise and energy deposition. These simulation results are then compared with the experimental data from a 2.0 cm \times 2.0 cm \times 1.5 cm CZT detector irradiated with a ^{137}Cs 662 keV gamma-ray source collimated by a tungsten collimator with a 100 μm opening. The result validated the accuracy of the proposed sub-pixel calculation methods. Finally, a method for measuring sub-pixel positions for two-pixel triggered events (or two-pixel events as we call) is presented and discussed.

5.2 The Detector System

An illustration of a 3-D position-sensitive CZT detector is shown in fig. 1.5. The CZT detector used in this study is 1.5 cm thick and its volume is 2.0 cm \times 2.0 cm \times 1.5 cm. The cathode is a simple continuous plane, while the anode consists of an array of 11 \times 11 pixels. Each 1.22 mm \times 1.22 mm pixel is surrounded by a grid biased at a voltage lower than the pixel. This technique effectively steers electrons toward pixels, thereby improving charge-collection efficiency. Alternatively, the grid can be biased at the same potential as the anode pixels, i.e. 0 V. In this case, some charge will be collected by the grid if the electron cloud occurs outside of the pixel. The grid also serves as a guard ring to reduce the surface leakage current from the side of the crystal. The steering grid is 100 μ m wide and has a 200 μ m gap to the pixels. Therefore, the total pixel pitch is 1.72 mm. In this study, a prototype digital readout system was build, which is capable of digitizing preamplifier signals waveforms as a function of time from a 3x3 pixel array. These signals can be used to retrieve a wealth of information of the interaction, including sub-pixel interaction positions. The details of this system are given in Section 5.5.1.

5.3 Sub-pixel Position Calculation Algorithm

The maximum amplitude of the transient signals of the 8 neighboring pixels can be compared quantitatively to determine the sub-pixel position of an interaction. However, the transient signal maximum decreases as the interaction position changes from the cathode side toward the anode side. The signal becomes very small when the interaction is in the anode region. If we choose the signal maximum to calculate the sub-pixel position, the algorithm coefficients may vary from depth to depth and the sub-pixel position resolution will be poor in the anode region.

Fortunately, the signal maximum occurs in a certain depth for the interactions

located at a particular lateral position, where the electron cloud just drifts past the boundary of the anode region. The weighting-potential change from this depth to the anode surface (charge fully collected) is independent of the initial depth of the electron cloud when this interaction occurs in the detector bulk. In other words, the signal difference between the signal maximum and its negative tail, the signal minimum, is not a function of interaction depth at a particular lateral position and in detector bulk. Therefore, we define the transient signal amplitude as the value difference between the signal maximum and minimum amplitudes. In the anode region this transient signal amplitude is no longer independent of interaction depth. However, it is still much bigger than the transient signal maximum, which is actually zero and thus this definition extends the active region where we can perform subpixel position calculation.

Transient signal amplitude is the key measurable parameter that is used to calculate sub-pixel interaction position. A method referred to as the *opposing-neighboring ratio* uses these neighbor pixel amplitudes to calculate the sub-pixel centroid position of an electron cloud. If the position of the center collection pixel and its 8 neighbors is labeled as shown in Fig. 3.6, the opposing-neighboring ratio along the lateral x direction, Rn_x can be written as

$$Rn_x(x, y, z) = \frac{s_{21}(x, y, z) - s_{23}(x, y, z)}{s_{21}(x, y, z) + s_{23}(x, y, z)}, \quad (5.1)$$

where $s_{21}(x, y, z)$ and $s_{23}(x, y, z)$ are the transient signal amplitudes on the middle-left and the middle-right neighbors respectively induced by an electron cloud located at (x, y, z) . As described above, the transient signal amplitude is not a function of depth z unless the interaction happens in the anode region. Therefore, equation 5.1 can be simplified as

$$Rn_x(x, y) = \frac{s_{21}(x, y) - s_{23}(x, y)}{s_{21}(x, y) + s_{23}(x, y)}. \quad (5.2)$$

Here, Rn_x is not only a function of the lateral x coordinate of the electron cloud, but also the lateral y coordinate. If a electron cloud is moving along the y direction, its distance to the middle-left neighbor (pixel 21) and middle-right neighbor (pixel 23) will change, resulting in different induced signals on those neighbors. However, if the left three neighbors and right three neighbors are considered as a whole respectively, the mean distance from the moving electron cloud to these neighbors will change much less. Therefore, a new signal ratio can be written as

$$\begin{aligned}
s_l(x) &\approx s_l(x, y) = s_{11}(x, y) + s_{21}(x, y) + s_{31}(x, y) \\
s_r(x) &\approx s_r(x, y) = s_{13}(x, y) + s_{23}(x, y) + s_{33}(x, y) \\
R_x(x) &= \frac{s_l(x) - s_r(x)}{s_l(x) + s_r(x)}.
\end{aligned} \tag{5.3}$$

We call this the opposing-neighboring ratio. The relationship between R_x and the x coordinates is calculated by simulation for different lateral y positions and depths z . The result is presented in Fig. 5.1. The change in R_x due to the variation of the lateral y position and the depth z of an interaction is given by the error bar. As can be seen, such change is small compared to the pixel size, indicating that the approximation of equation 5.3 is valid. Additionally, Fig. 5.1 shows that the R_x versus x curve is close to a straight line. To a first order approximation, we can employ a linear function to model the signal ratio R_x versus x in the sub-pixel position calculation.

In the y direction, the opposing-neighboring ratio R_y can be formed the same way as for R_x :

$$\begin{aligned}
s_t(y) &\approx s_t(x, y) = s_{11}(x, y) + s_{12}(x, y) + s_{13}(x, y) \\
s_b(y) &\approx s_b(x, y) = s_{31}(x, y) + s_{32}(x, y) + s_{33}(x, y) \\
R_y(y) &= \frac{s_t(y) - s_b(y)}{s_t(y) + s_b(y)}.
\end{aligned} \tag{5.4}$$

Besides the opposing-neighboring ratio, there are at least two more ratios that can be used to calculate the electron cloud position:

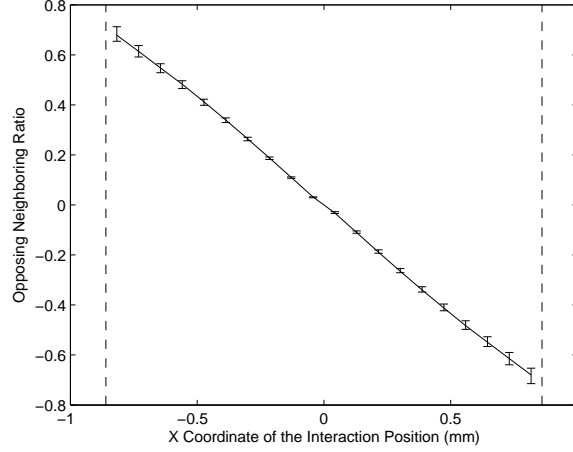


Figure 5.1: The relationship between the opposing-neighboring ratio R_x and real lateral x coordination calculated by simulation. The curve gives R_x as a function of x when the electron cloud is in the middle of a pixel ($y = 0$) and near the cathode surface ($z = 0$). The error bars mark the range of the R_x if the lateral y position and the depth z of the electron cloud change in the pixel volume. The dashed lines mark the boundary of a pixel.

1. the ratio between the neighboring pixel signals and the center pixel signal
2. the signal ratio between two corner neighbors and the center pixel signal.

We refer to (1) as the *neighbor-to-center ratio*, and (2) the *corner-neighbor ratio*. The neighbor to center ratio (Rc_x and Rc_y) and corner neighbor ratio (Rcr_x and Rcr_y) are expressed as

$$\begin{aligned} Rc_x(x) &= \frac{s_l(x)}{s_{22}} \\ Rc_y(y) &= \frac{s_t(y)}{s_{22}} \end{aligned} \tag{5.5}$$

and

$$\begin{aligned} Rcr_x(x, y) &= \frac{s_{11}(x, y) - s_{13}(x, y)}{s_{22}} \\ Rcr_y(x, y) &= \frac{s_{11}(x, y) - s_{31}(x, y)}{s_{22}} \end{aligned} \tag{5.6}$$

where s_{22} is the charge collected by the center pixel. These two methods have their shortcomings. For the neighbor-to-center ratio, the ratio is not a linear function of the actual electron cloud position. For the corner-neighbor ratio, the ratio is a function

of both x and y coordinates and thus is difficult to calibrate. Therefore, the opposing neighbors' transient ratio is preferred.

However, neighbor-to-center ratio and corner-neighbor ratio require fewer neighboring pixel signals than the opposing-neighboring ratio. The neighbor-to-center ratio requires three neighbors on one side of a collecting pixel. The corner-neighbor ratio method requires two corner neighbors. For multi-pixel interaction events, the induced signal on a neighboring pixel from a electron cloud may be polluted by the signal induction from another separate electron cloud. In this situation, opposing-neighboring ratio may not be applicable and then the neighbor-to-center ratio or corner-neighbor ratio could be employed to determine the sub-pixel position for each electron cloud. Section 5.6 addresses this scenario in greater detail.

5.4 Estimate of Sub-pixel Position Resolution by Simulation

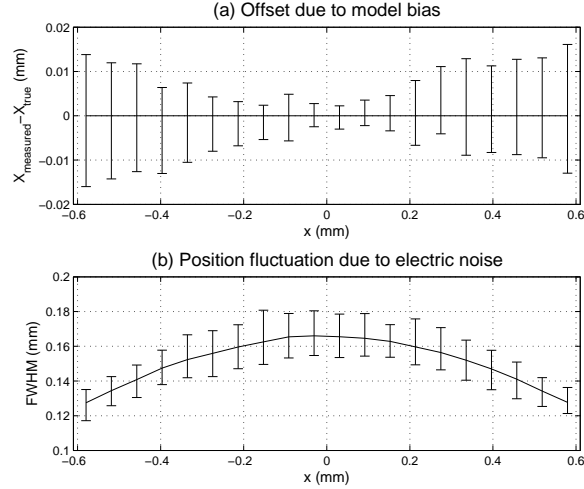


Figure 5.2: Sub-pixel simulation performance results: (a) the offset difference between the mean calculated position and the true simulated position based on the linear assumption, and (b) the position variation in terms of FWHM due to 4 keV electronic noise. The offset and position variation is plotted for the x coordinate. The error bars mark the offset and FWHM range as the electron cloud position is shifted along y and z directions through the volume of the collecting-pixel column.

The precision of the sub-pixel position obtained by the opposing-neighboring ratio method can be estimated based on the system model discussed in section III. The results are given in Fig. 5.2. In this simulation, the energy deposition of the gamma ray is set to be 662 keV and the electronic noise is set to 4 keV FWHM. The cathode is assumed to be biased at -3000V and the grid is at -100V. The sampling frequency is set as 100MHz. The energy is assumed to be deposited at a single space point rather than an extended electron cloud for principle study. Fig. 5.2(a) gives the bias of the calculated position using the linear-relation assumption of R_x (as defined in Equ.5.3) versus x from the true energy-deposition position. Fig. 5.2(b) presents the calculated sub-pixel position uncertainty due to the 4 keV electronic noise. The calculated position bias is smaller than the position uncertainty, indicating that the linear assumption is an appropriate model.

The dominant source of uncertainty in the calculated sub-pixel position is the electronic noise. Uncertainty in the collected charge due to charge production in the ionization process and charge trapping will generate proportional changes to the signals induced on all 8 neighbors. As a result, the associated fluctuation cancel out using the signal ratio. As seen in Fig. 5.2(b), the expected sub-pixel position resolution at 662 keV is below 180 μm . This simulation result assumes energy is deposited at a single point. In reality, energy is deposited in an extended electron cloud. The calculated sub-pixel position for a real interaction is the centroid of the electron cloud. As a result, the size of the electron cloud will introduce additional uncertainty in the determination of the interaction position.

5.5 Experimental Measurements and Analysis

5.5.1 Measured Sub-pixel Position Resolution with Collimator

Results from a collimation experiment provide an experimental measure of the sub-pixel position resolution. Fig. 5.3 illustrates the design of the collimator experiment. The collimator is made of 6-cm thick tungsten with a 100- μm opening, separated by 3 cm away the bottom surface of the detector. The opening of the collimator is aligned parallel with the edge of a target pixel. A ^{137}Cs point source is placed in the collimator and used to irradiate a narrow section of the pixel from the cathode side of the detector. The irradiated pixel and its 8 neighbors are connected to eV-Products model 5093 preamplifiers. Each preamplifier signal is fed into a channel of a GaGe Octopus CompuScope model 8389 multichannel digitizer card (8 channels per card, 14-bit resolution, 125 MHz), operating at a 100 MSa/s sampling rate (10-ns sampling interval).

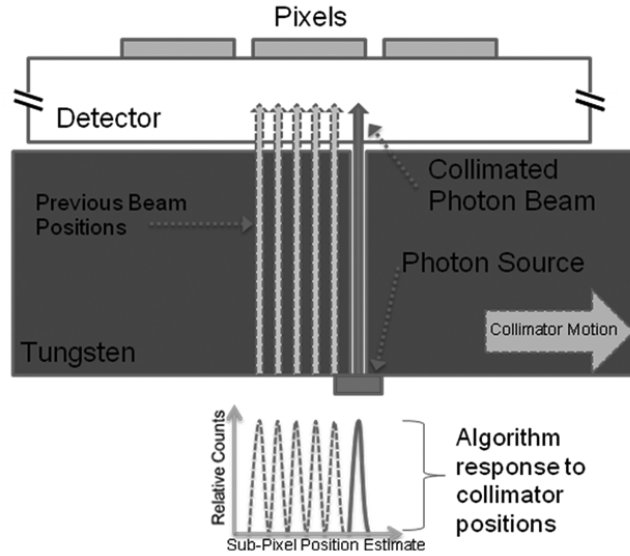


Figure 5.3: The collimator design for experimentally measuring sub-pixel position resolution.

The detector is manufactured by eV-Products. The detector schematics are identical to those found in the system model discussion in Section III. During operation,

the cathode is biased at -3000 V but the grid was unintentionally left unbiased. However the different grid bias shouldn't impact the conclusion we have achieved in the simulation.

The collimator is positioned near the center of the pixel at first and then moved toward the edge with a step size of $100\text{ }\mu\text{m}$. For each collimator position, photopeak events from single-pixel interactions are selected for use in the sub-pixel study. For neighbor-pixel signals, a CR-RC filter with 200-ns shaping time is employed. This filter choice is based on the simulation results described in Section 2.3. The results of the measurements at four collimator positions are summarized in Fig. 5.4. Fig. 5.4(a) shows the opposing-neighboring ratio for each collimator position and Fig. 5.4(b) gives the measured position uncertainty. The x axis origin of both plots are the start location of the collimator. The FWHM of the position estimate is below $360\text{ }\mu\text{m}$.

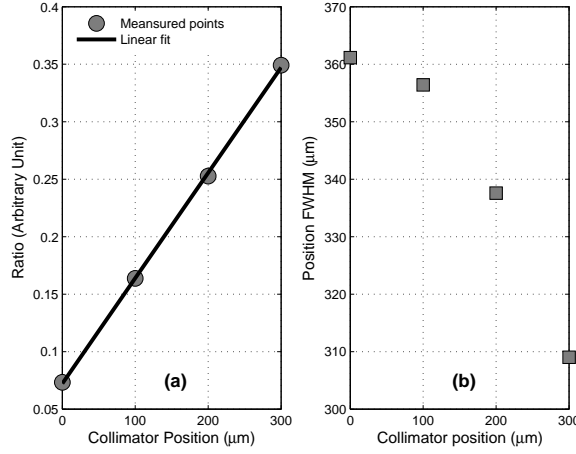


Figure 5.4: Measured sub-pixel resolution at 662 keV: (a) the mean neighboring pixel ratio for each collimator position. This data is fitted by a linear function and the result shows the slope as $(9.2 \pm 0.5) \times 10^{-4}$ and the interception as 0.072 ± 0.009 with 95% confidence; (b) the FWHM of the position variance at each collimator position. The origin of x axis of these plots are the start location of the collimator instead of the center of the pixel.

However, this $360\text{-}\mu\text{m}$ position uncertainty is not equivalent to the sub-pixel res-

olution. There are two more factors that add uncertainty to the measurement: (1) collimator-beam size and (2) electron cloud size. The collimator has a $100\text{-}\mu\text{m}$ opening, but the beam will be spread bigger at the detector surface and the beam size will become even wider when the interactions occur at deeper depths in the detector. The increase in measured resolution caused by the collimator is significant. Additionally, the measured sub-pixel position of each interaction represents the centroid of the ionized electron cloud not the initial gamma-ray interaction position. As a result, even when the gamma beam is fixed at a single position relative to the detector, the electron cloud centroid will be different if the secondary fast electron follows a different track. Using the Geant4 simulation package, we can simulate the total uncertainty contribution from the two factors together. As shown in Fig. 5.5, we find that the collimator beam and 662-keV electron cloud can cause $280\text{-}\mu\text{m}$ FWHM position uncertainty in the measurement. The contributions of spreading from collimator and electron cloud size can be simulated individually and the result shows collimator can cause $150\text{ }\mu\text{m}$ spreading in FWHM and electron cloud size introduces $240\text{ }\mu\text{m}$. Though both collimator and electron cloud caused spreading are not strictly Gaussian shaped, the quadratic sum of the contribution from collimator and electron cloud results in the same result as obtained with the simulation considering them together, indicating quadratic operation can be applied in estimating the contribution of each factor to sub-pixel position resolution measurement.

After quadratic subtraction, the real sub-pixel resolution of the system in terms of determining electron cloud centroid position is calculated to be around $230\text{ }\mu\text{m}$ at 662 keV. However, if we consider the initial gamma-ray interaction position, we would need to add the the additionally uncertainty caused by electron cloud size. The projection of electron cloud size on x-y plane is a function of recoil electron direction, especially at high energy. If assuming the secondary electrons are emitted isotropically, the sub-pixel position resolution of initial gamma-ray interaction position would

be 330 μm FWHM at 662keV.

The 230- μm sub-pixel position resolution at 662 keV is a little bit worse than the simulation result of 180 μm . There are several factors that may cause the difference, including the inaccuracy of the measured geometry of the collimator setup (especially the distance between the detector and the collimator and the opening width), slight skewing of the collimator beam, the neglected $1/f$ noise, the diffusion of the electron cloud and material defects.

The inaccuracy of the measurement on geometry setup can be estimated in a easy way. The spreading caused by the collimator should be proportional to $\delta \times (d + z)/z$, where δ is the opening width, d is the distance between collimator surface and detector surface and z is the collimator thickness. It can be calculated that even with 1 cm error on d or z , the change of total uncertainty caused by collimator and electron cloud would be smaller than 20 μm . For opening width δ , the error of measurement should be less than 10% and its influence on total uncertainty can be calculated to be smaller than 20 μm too. Therefore, the geometry measurement error should be negligible. Diffusion can change the drifting path of electrons [26]. For our 1.5 cm CdZnTe crystals at 3000V, diffusion caused position uncertainty for each electron would be about 70 μm in standard deviation and thus 170 μm in FWHM if assuming Gaussian distribution. However, ideally diffusion shouldn't shift the centroid of an electric cloud if the electron cloud is consisted of infinite number of electrons. In reality we expect additional uncertainty from diffusion but its impact on sub-pixel position resolution should be much smaller than 170 μm and we expect its impact on the measurement uncertainty should be negligible. The presence of $1/f$ noise may change the performance of the CR-RC filter and cause some underestimation of the uncertainty from the electronic noise in simulation. At last, the material defects in CdZnTe has been known for deviate electrons from drifting straight [22]. In a poor crystal, this effect can move electron several hundred microns in lateral direction. In

our experiment, a good CdZnTe detector was chosen but the deviation should still be noticeable according to Kaye et al. [22]. Therefore, we suspect material defects to be the main cause of the slight inaccuracy of the collimator experiment result.

The sub-pixel position resolution of electron cloud centroid is proportional to the energy deposition. The reason is the induced signals on the neighboring pixels are proportional to the energy deposition while the electronic noise is a constant. However, with the energy deposition increases, the electron cloud size gets larger. The total influence of those two effects will make the measured gamma-ray interaction position resolution improve at first with energy deposition increasing and then degrade when the energy deposition passes a favorite energy. On the other hand when the energy of recoil electrons is very high, the electron track would be very long and there might be a chance to extract the electron cloud distribution and reduce the impact of the large electron cloud size on identifying gamma-ray interaction position.

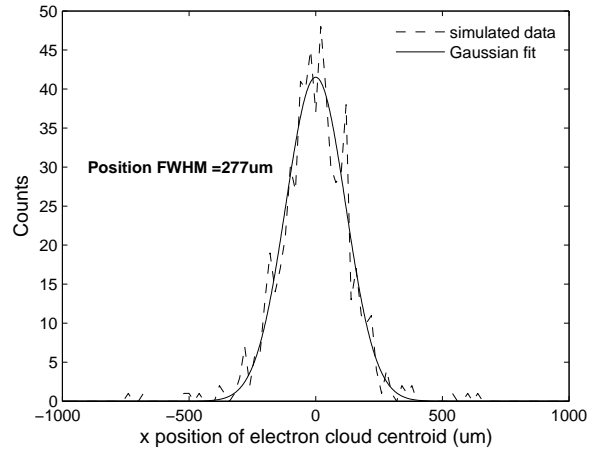


Figure 5.5: The simulated distribution of the electron cloud centroid from a 662-keV gamma-ray source using a collimator. Distribution width is due to the collimator and electron cloud size.

5.5.2 Complete Charge Collection Boundary

If a source is placed on the detector's cathode side and far from the detector, the single-pixel photopeak counts should be distributed uniformly along the lateral plane

of the collecting pixel.

The boundary of this distribution marks the edge of the complete charge collection region. If the steering grid between the pixels is biased at the correct voltage, the electrons are expected to be steered toward the pixel and no charge should be lost in the gap between anode electrodes. In this case, the full pixel is the complete charge collection region and photopeak counts distribution should spread from one pixel edge to another, namely from -0.86 mm to 0.86 mm since the pixel pitch is 1.72 mm. When the grid is unbiased or grounded, only those events located under the pixel pad can be fully collected. The complete charge collection region should shrink to the pixel pad size, which is 1.22 mm.

Fig. 5.6 shows the distribution of measured single-pixel photopeak events within a pixel when the steering grid is unbiased. The dotted line marks the measured pixel boundary of complete charge collection. As shown, the complete charge collection region is from -0.6 mm to 0.6 mm, totally 1.2 mm, consistent with our expectation.

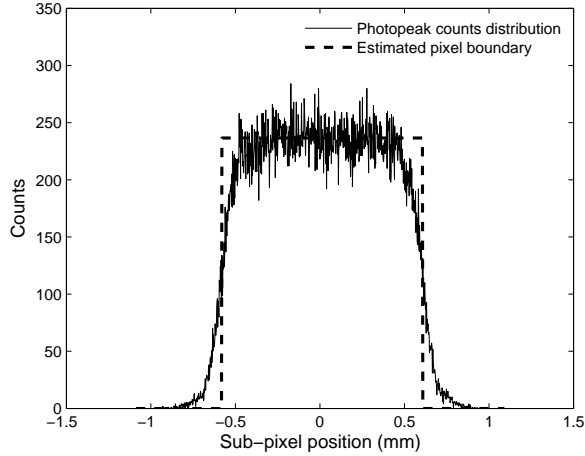


Figure 5.6: The distribution of single-pixel photopeak events inside a pixel.

The pixel boundary can affect the measured result of the collimator position. When the collimator is placed close to the complete charge collection boundary with unbiased grid, a portion of events will lose some charge to the gap or the grid and then

they will not be registered as photopeak events. If we only choose photopeak events to measure the collimator center position, the measured collimator center position will be shifted. Fig. 5.7 shows that the center position of the selected photopeak events, or the measured collimator center, is shifted toward the inside of the pixel when the collimator is placed near the edge of the complete charge collection region. The dotted line shows the edge of the complete charge collection region. A simulation was carried out to test this behavior. The result is also shown in Fig. 5.7. The solid curve gives the calculated collimator center using only photopeak events based on the sub-pixel calculation algorithm. It agrees well with the measurement.

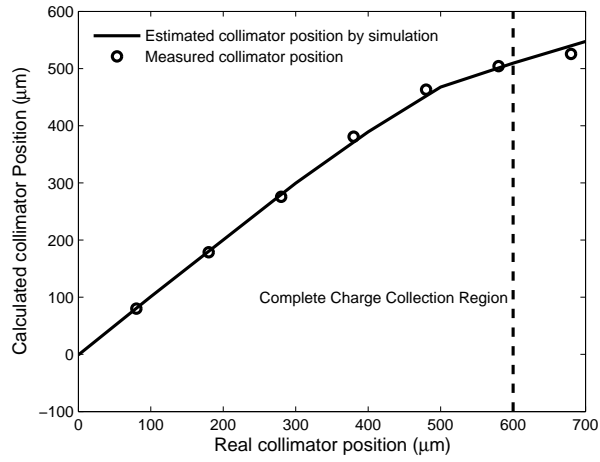


Figure 5.7: Calculated position versus collimator position including a comparison between the simulation and experimental results. The dotted line marks the boundary of the complete charge collection region.

5.6 Sub-pixel Resolution for Two-pixel Events

Two-pixel events can be categorized into three groups according to the distance between the two triggering pixels:

1. neighboring events, including side neighboring or diagonally neighboring events
2. non-neighboring events with a pixel-center-to-pixel-center distance less than

three pixels, and

3. non-neighboring events with a pixel-center-to-pixel-center distance greater than or equal to three pixels.

In the discussion above, we only considered the induced signals on the 8 pixels surrounding the charge collecting pixel. For the non-neighboring pixels, the distance to the electron cloud is far, but signals are still induced. However, these signals are so small that we can ignore them in a first order approximation. With this assumption, the sub-pixel position calculation can be performed in the same way as it was for single-pixel events in case (3). However, for case (1) and case (2), the induced signal on a neighboring pixel from one electron cloud may be polluted by the induced signal from another electron cloud. To study these two cases, they can be further grouped into two categories based on the arrangement of the triggered pixels:

- (a) the two collecting pixels are diagonally placed, and
- (b) the two collecting pixels are both on the same row or column

Fig. 5.8 illustrates the two categories of neighboring pixel events. In Fig. 5.8(a), the two collecting pixels are pixel A and pixel B. The neighboring pixels of pixel A are labeled as A1, A2, A4, A5, A6, A7 and A8, while for pixel B as B1, B2, B3, B4, B5, B6, B7 and B8. Based on our assumption that the induced signals on non-neighboring pixels are negligible, the signals on the neighboring pixels except pixel B7/A5 and pixel B4/A2 are induced only by one electron cloud and their amplitudes can indicate the position of that electron cloud. These unpolluted neighbors are sufficient to apply neighbor-to-center ratio (as defined in section 5.3) and both x and y sub-pixel positions can be determined.

For the case shown in Fig. 5.8(b), the x -direction unpolluted neighbors for collecting pixel A are A1, A4 and A6. They form one column so one can apply the

neighbor-to-center ratio for x direction. However, for the y direction, there is not an entire row of 3 unpolluted pixels. Therefore, the corner neighbor ratio method needs to be employed. We will discuss the application of neighbor-to-center ratio first and then the corner-neighbor ratio.

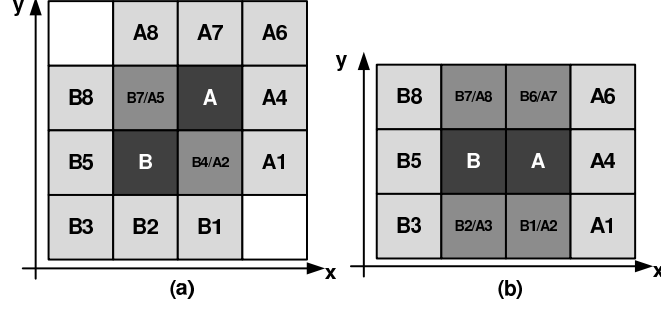


Figure 5.8: The two cases of the arrangement of the triggered pixels for neighboring pixel events.

As discussed in Section 5.3, the neighbor-to-center ratio does not have a linear relationship with the interaction position. However, the opposing-neighbor ratio is a linear function of interaction position. Therefore, we can associate the neighbor-to-center ratio with the opposing-neighbor ratio to calibrate the nonlinear relation. This step can be done for single-pixel events.

To demonstrate the effectiveness of the neighbor-to-center ratio, we again use a fan-beam collimator experiment. The collimator was placed near the center of a pixel and its opening was oriented along the y direction so that all the events through the collimator were located around $x=0$. The neighboring two-pixel photopeak events were chosen and the sub-pixel position of the first interaction (its electron cloud was collected by the collimated pixel) was calculated with the neighbor-to-center ratio. As a comparison, we also blindly applied the opposing-neighbor ratio method even though the neighboring pixel signals were polluted. If the sub-pixel position calculation was correct, we should observe the first interaction position around $x=0$.

The results are presented in Fig. 5.9. The sub-pixel position distribution for single-pixel photopeak events is also plotted to give a reference position of the collimator.

As can be seen, the sub-pixel position calculated from the opposing-neighboring ratio is pushed away from the real interaction position. Since for neighboring two-pixel events, a neighbor is collecting charge and its total induced signal becomes much higher than it should be. The neighbor-to-center ratio method gives a much better result. However, the position resolution is poorer than that for the single-pixel events. A major reason is that the energy of each interaction of a two-pixel photopeak events is less than that of single-pixel photopeak events leading to smaller induced neighboring pixel signals. Additionally, the neighbor-to-center ratio for neighboring two-pixel events assumes the induced signals are negligible if the distance is greater than two pixels. However, the induced signals are not exactly zero. This small charge induction can cause small offsets of the calculated interaction position from the real interaction position. This effect will be most prominent when the electronic noise becomes very low.

In Fig. 5.8 (b), the y sub-pixel position needs to be calculated by the corner-neighbor ratio. As mentioned in section 5.3, the corner-neighbor ratio is a function of both x and y coordinates. Thus, the x sub-pixel position needs to be calculated first by the center-to-neighbor ratio and then the corresponding relation of corner-neighbor ratio versus y position can be extracted and used for calculating the y sub-pixel position. As a result, the corner-neighbor ratio is expected to have higher uncertainty than the neighbor-to-center ratio.

5.7 Performance Improvement with Sub-pixel Resolution

5.7.1 Compton Imaging Improvement

With sub-pixel position sensing, Compton imaging resolution can be improved. However, the events that can be used for Compton imaging are multi-pixel-triggered

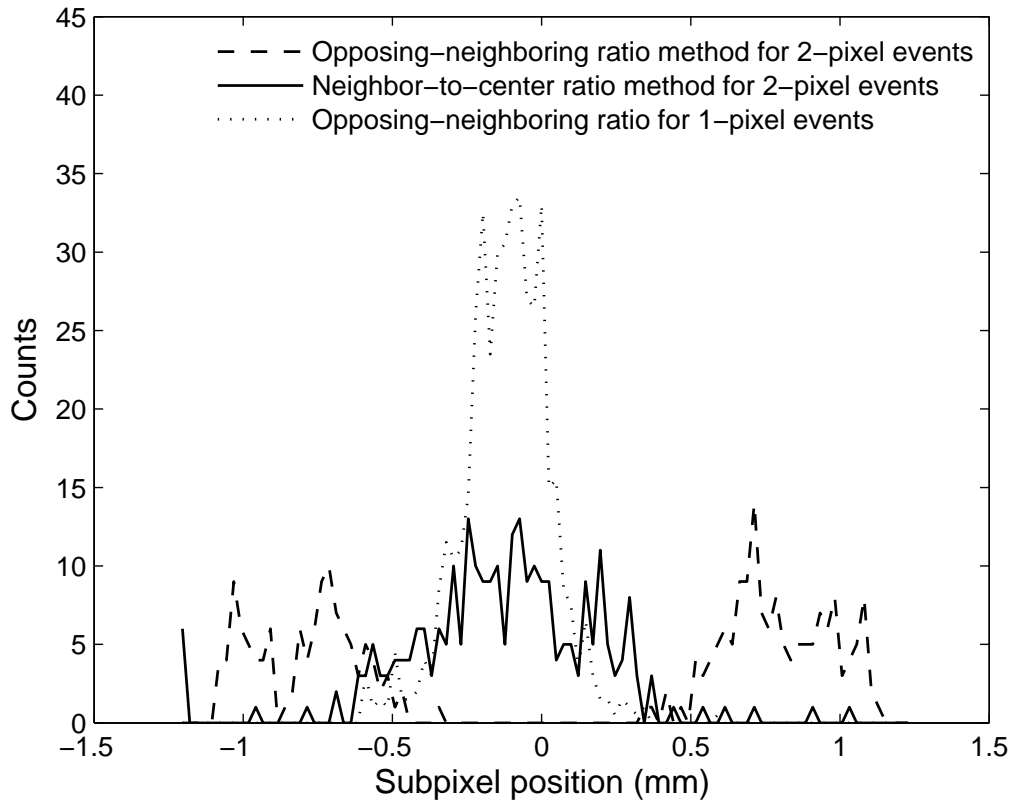


Figure 5.9: Sub-pixel position for the two-pixel events in the collimator experiment. The energy deposition on the neighboring pixels is required to be greater than 100 keV.

events. As talked, sub-pixel position resolution is reversely proportional to the energy of the electron cloud. Therefore, the improvement of the image quality isn't a simple function of total energy deposition. To estimate how much the sub-pixel position sensing can improve Compton imaging, we did a simple simulation based on Geant4. In this simulation, we used the inversely proportional relation between sub-pixel position resolution and energy to add uncertainty to the simulated electron cloud centroid to emulate the impact of electronic noise. Since the sub-pixel position sensing would be very poor when the energy is low, the triggered pixel location may be more precise than the calculated sub-pixel position. Here is the criteria we applied to determine if the sub-pixel position should be used: if the calculated sub-pixel position is outside of the collecting pixel, we put the cloud back to the edge of the pixel; if the energy is too small that the sub-pixel position uncertainty is bigger than the pixel size, we pick the pixel center as the interaction location, or in other words, we discard the sub-pixel information. The simulation result is shown in figure 5.12¹.

Additionally, there is one more information that can be used to further improve the imaging quality, which is the displacement from the original interaction location to the measured electron cloud center due to the momentum of recoil electrons. As we know, the measured sub-pixel position isn't the original interaction position, but the centroid of the electron cloud generated by the recoiled electron. The displacement is a random variable. Figure 5.10 shows the 2-D plot of the distribution of this displacement for those electrons emitted toward the positive x-axis for several different energies. As shown, there is a hot spot in each plot, which represents the most possible displacement that can happen. On the other hand, if the electron cloud centroid is measured and the recoil direction is known, we should be able to correct the displacement and determine what is the most possible original interaction location. It is well known that in Compton imaging the recoil direction isn't unique. Compton

¹This plot is from Weiyi Wang, University of Michigan.

scattering only tells the recoil angle and the recoil direction can be any one of the directions on the recoil cone. However, if we apply the displacement correction to each possible recoil direction, the corresponding incoming gamma-ray direction will be better determined. As a result, the incoming gamma-ray cone can be more precise and the Compton image can be better formed. The improvement of this recoil electron correction depends on the uncertainty of the displacement. If the uncertainty is too big, the improvement could be very limited. Figure 5.11 shows the mean displacement and the variance as a function of energy. As can be seen, the uncertainty is smaller than the mean value, indicating that it is possible to observe some improvement, which can be seen from plot 5.12(a) to plot 5.12(b). The detailed correction algorithm can be found in [Weiyi's thesis].

To verify the simulation result, we carried out an experiment on detector # 4E3, a $20 \times 20 \times 15$ mm³ CdZnTe detector made by eV product. The same criteria is employed to determine how the calculated sub-pixel position should be used. Figure 5.13² shows the experimental result, which is poorer than the simulation result but having the similar trend of improvement as sub-pixel and displacement correction is applied individually.

5.7.2 Energy Resolution Improvement

Sub-pixel position sensing can help to improve the energy resolution (1) for single-pixel-triggered events by correcting photopeak shift in lateral direction and (2) for multi-pixel-triggered events by obtaining much detailed crosstalk information. This section will give a demonstration of those two effects.

For single-pixel-triggered events, there are two factors that can cause the photopeak to vary within one pixel: (1) lateral change of weighting potential and (2) small charge leakage to the neighboring pixels. The weighting potential is a function of

²This plot is from Weiyi Wang, University of Michigan.

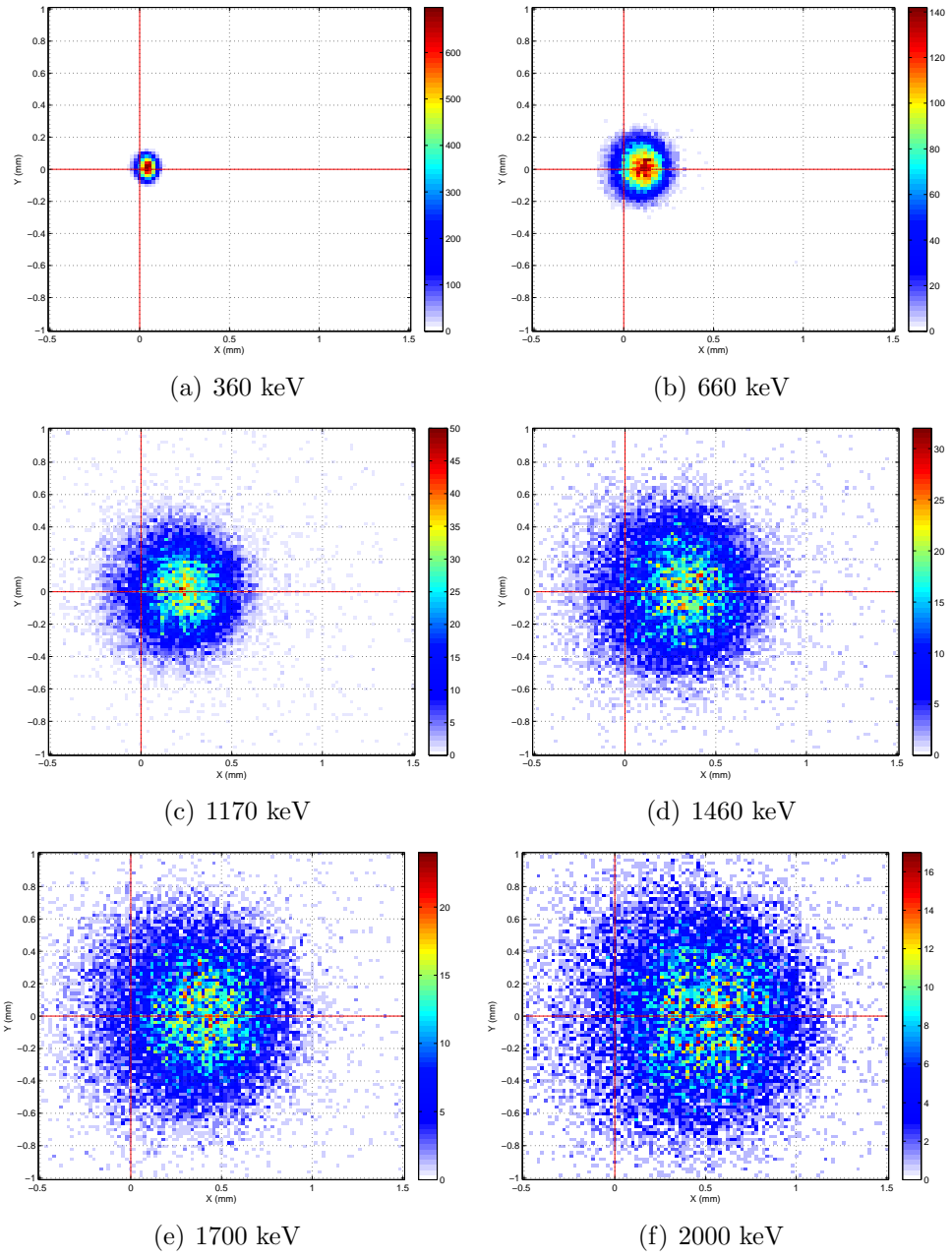


Figure 5.10: The distribution of the displace between the original interaction location and the centroid of the electron cloud. The crossing point of the red lines marks the origin of the interaction. The electrons are emitted toward positive-x direction.

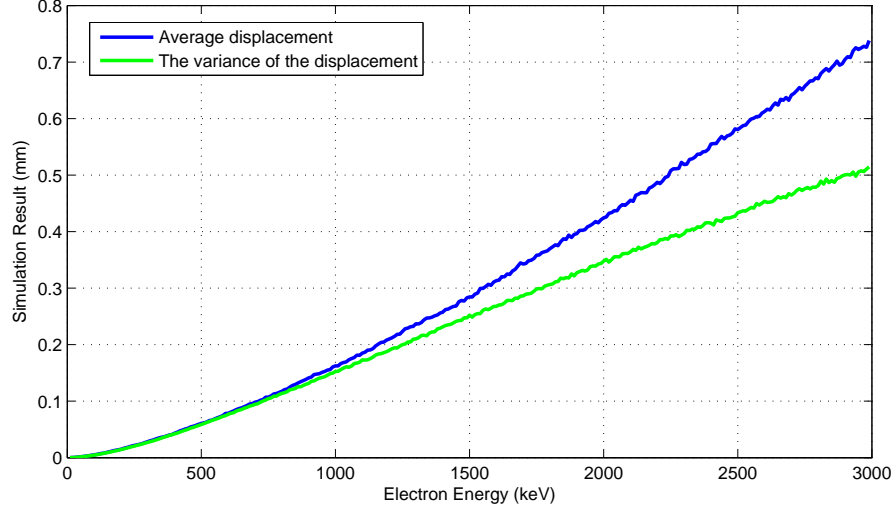
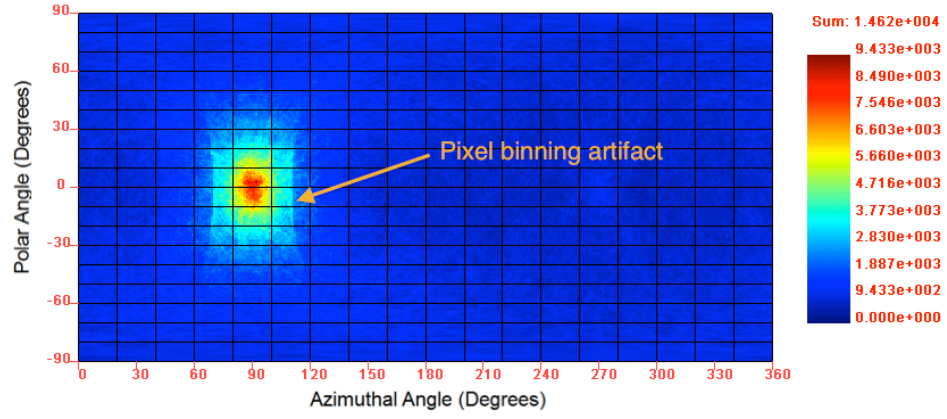
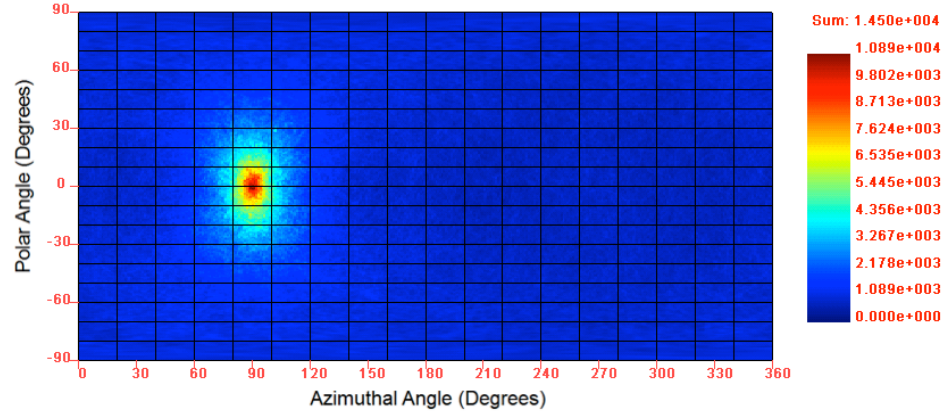


Figure 5.11: The mean and variance of the displace between the original interaction location and the centroid of the electron cloud. The variance is calculated for the displace spreading along x, y and z directions. The biggest variance among the three directions is shown in this plot.

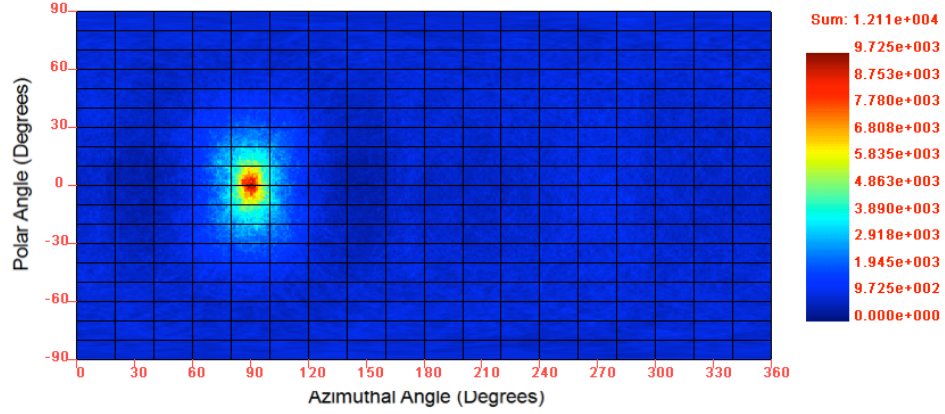
3-dimensional position. When the interaction is in the detector bulk, the variation of weighting potential from one sub-pixel location to another is very small so that usually this difference can be ignored. When the interaction gets close the anode surface, this difference can become noticeable. As a result, the induced signal for those interactions close to the anode surface is a function of sub-pixel location, which is an very important reason why the anode side photopeak resolution is pretty poor as shown in figure 5.14. The charge leakage to the neighboring pixels happens when the interaction is close to the pixel edge. Usually we use a simple threshold to tell if any charge is deposited on the pixel. With this method, when the leaked charge is so small that it is comparable to the electronic noise, it will be invisible to the system. Additionally, the induced signal on the neighboring pixels is a function of depth. It become more and more negative when the interaction happens closer and closer to the anode surface, which can hide some charge and make the total signal appear to be under the threshold even when the leaked charge is noticeable. Those two effects can cause energy resolution to degrade.



(a) Back-projected image with simple pixels. The polar and azimuthal angular resolution is 31.7 degree and 23.6 degree respectively.

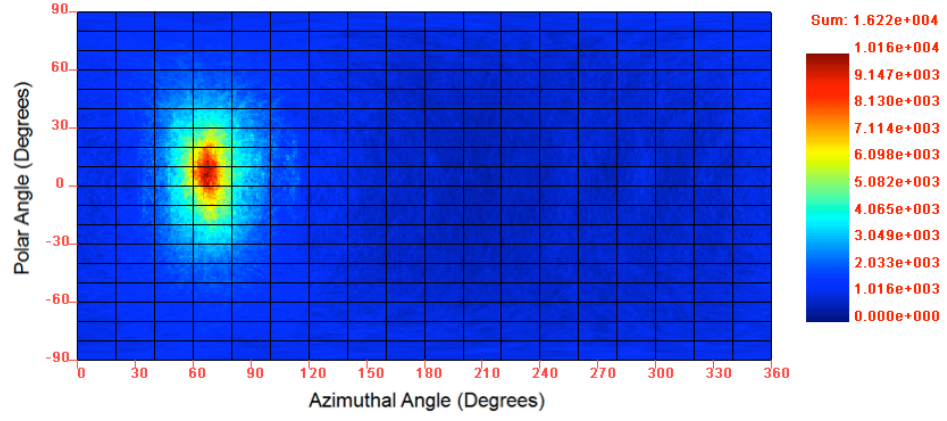


(b) Back-projected image with sub-pixel position. The polar and azimuthal angular resolution is 24.8 degree and 15.8 degree respectively.

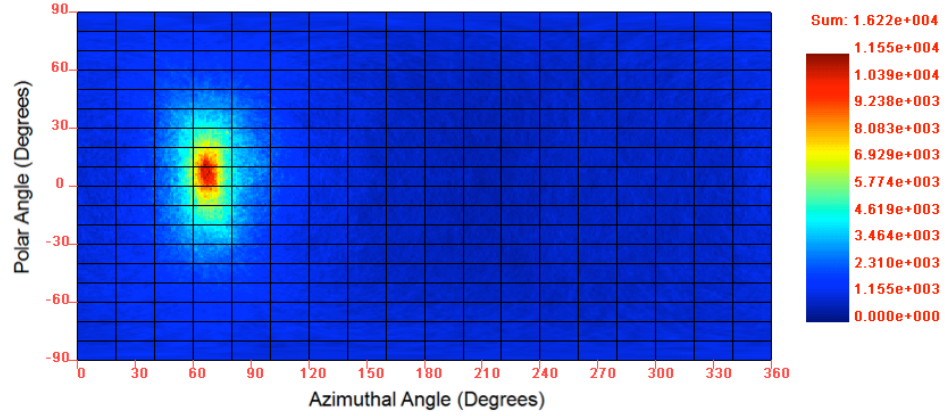


(c) Back-projected image with sub-pixel position plus recoil electron correction. The polar and azimuthal angular resolution is 21.2 degree and 14.4 degree respectively.

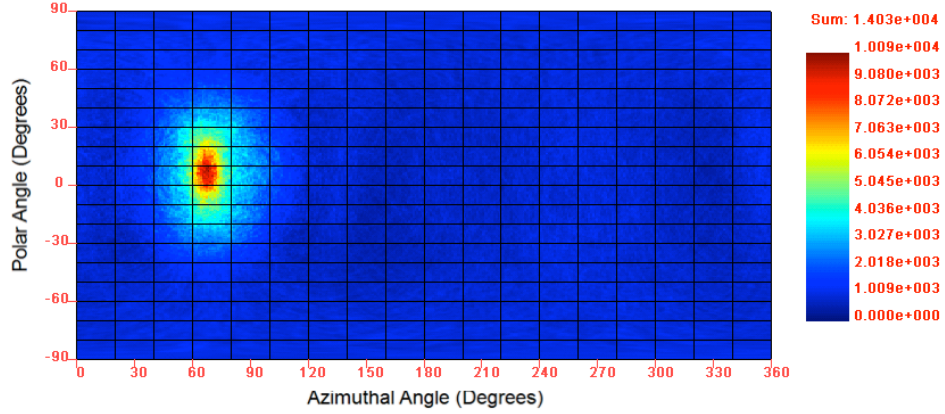
Figure 5.12: Simulated improvement of Compton imaging quality using simple back-projection method after applying sub-pixel position calculation algorithm and displacement correction. The sub-pixel position resolution is assumed to be $300 \mu\text{m}$. The gamma-ray source is 1460 keV.



(a) Back-projected image with simple pixels. The polar and azimuthal angular resolution is 37.5 degree and 23.1 degree respectively.



(b) Back-projected image with sub-pixel position. The polar and azimuthal angular resolution is 33.9 degree and 16.6 degree respectively.



(c) Back-projected image with sub-pixel position plus recoil electron correction. The polar and azimuthal angular resolution is 30.0 degree and 15.3 degree respectively.

Figure 5.13: The observed improvement of Compton imaging quality using simple back-projection method after applying sub-pixel position calculation algorithm and displacement correction on detector # 4E3. The sub-pixel position resolution is estimated to be about $300 \mu\text{m}$. The gamma-ray source is Co-60 1332-keV line.

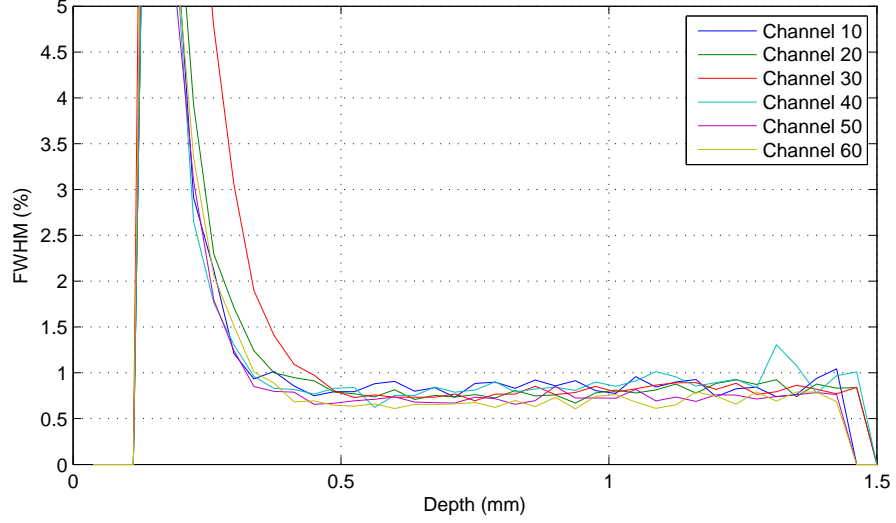
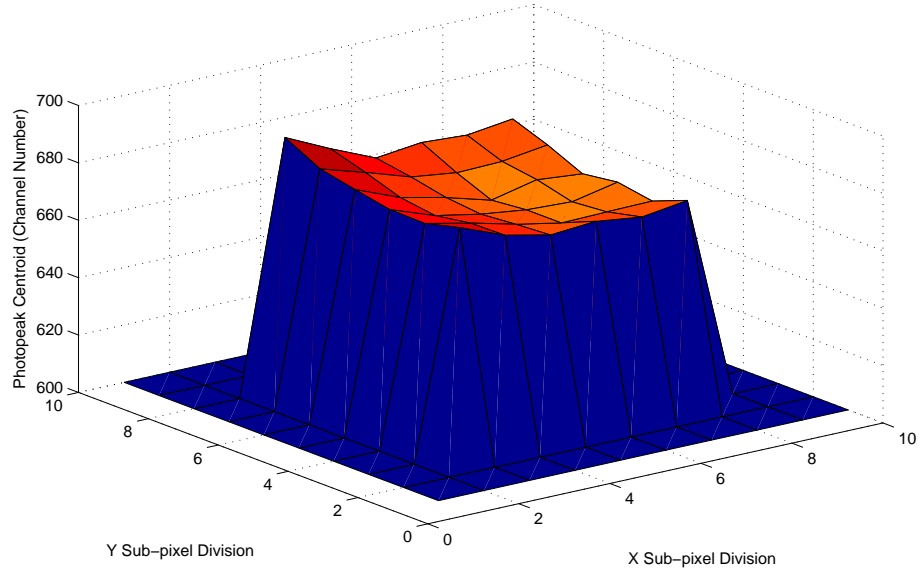


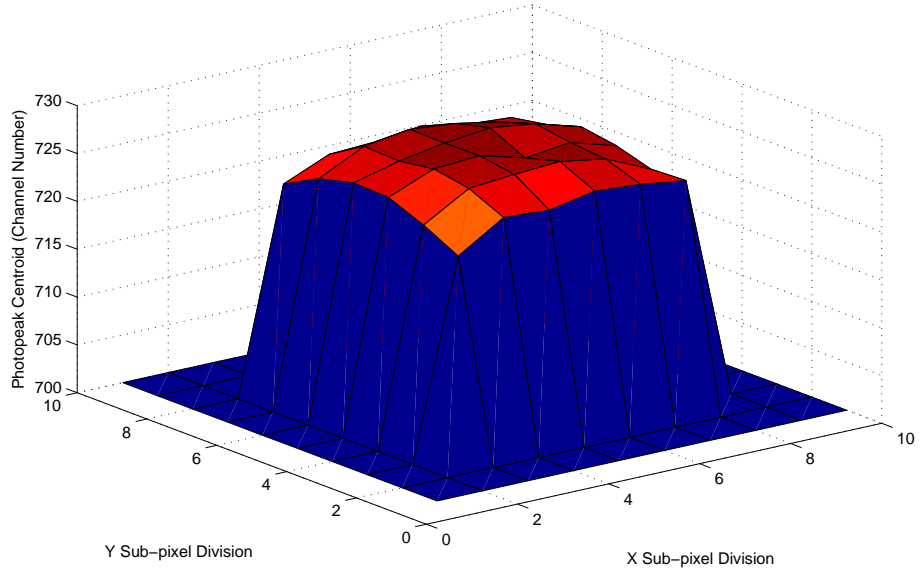
Figure 5.14: The measured energy resolution changing with depth for several channels. This data is obtained from detector # 4E3 with the cathode biased at -3000V and the grid biased at -40V. This detector is a $20 \times 20 \times 15$ mm³ CdZnTe detector made by eV product.

Figure 5.15 presents the 662keV photopeak centroid variation with sub-pixel position for two depths: one is near the anode side and another is in the middle of the detector. When the interaction is the detector bulk, the change of weighting potential as a function of sub-pixel position is very small, so that we can observe very clear photopeak centroid drop at the edge of the pixel because of charge leak as shown in the figure 5.15(b). On the anode side, weighting potential variation becomes significant and so that we can observe a different variation trend of photopeak centroid. In fact, in the edge region of the pixel, the absolute weighting potential is smaller comparing to the area in the middle of the pixel. Therefore, the difference of the weighting potential between the interaction location and the collecting pixel surface (which is 1) is bigger for the edge region. As a result, the induced signal would be bigger which is what figure 5.15(a) presents.

We can directly apply this measured photopeak centroid vs. sub-pixel position relation to correct the sub-pixel signal variation. We found this correction can help the energy resolution to be improved from 0.73% FWHM to 0.69% FWHM at 662keV



(a) 2.3 mm from the anode side which is very close to the anode pixels.



(b) 7.5 mm from the anode side which is in the middle of the detector.

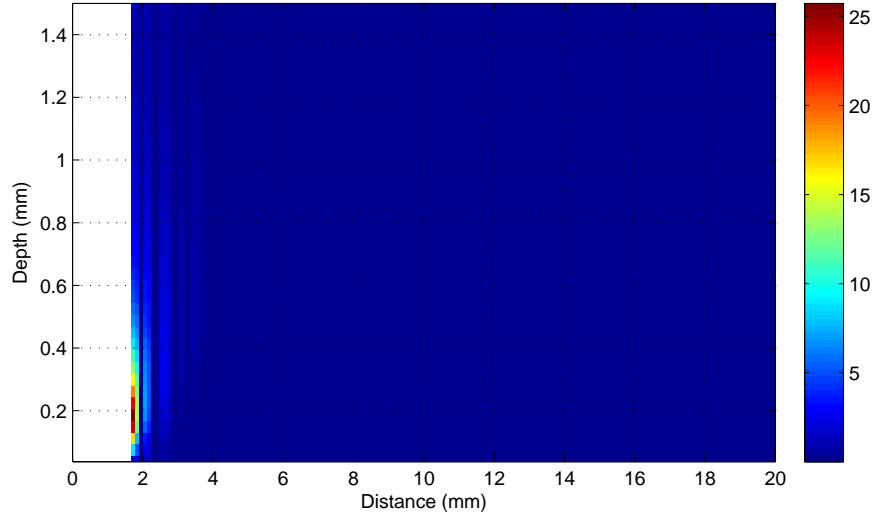
Figure 5.15: The 662keV photopeak centroid variation with sub-pixel position at two depths. This plot is measured on $4E7$ with the thickness about 15 mm and the cross-section as $20 \times 20 \text{ mm}^3$. This detector is made by eV product.

in detector 4E7. However, it should be noticed that this improvement shows the upper limit of sub-pixel correction. In fact, the charge loss is related to electron cloud size and it is a function of energy. As a result the photopeak centroid variation with sub-pixel position at other energy is different from that at 662 keV. Therefore, the two factors, weighting potential variation and charge leaking, need to be separate in the calibration process. The charge leaking needs to be compensated before the weighting potential variation can be figured out. Chapter VII will talk about the method to compensate the charge leaking.

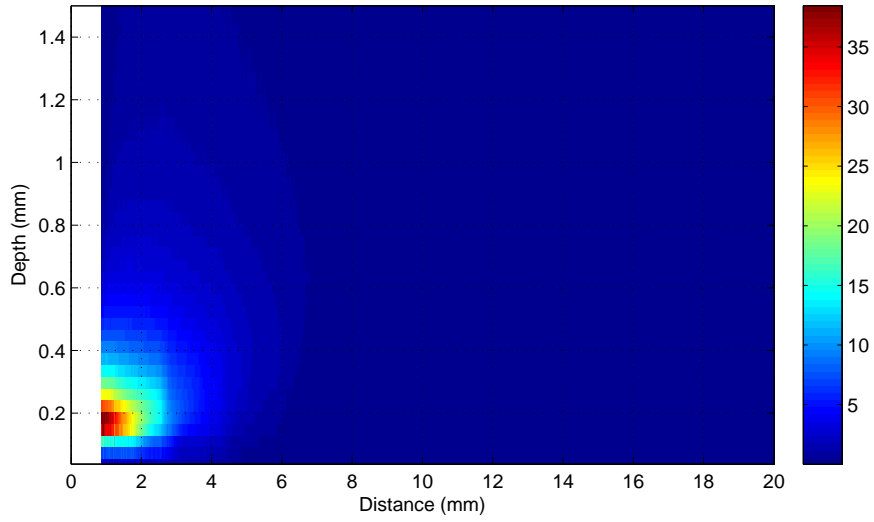
As for multi-pixel events, sub-pixel sensing can help to obtain very precise weighting potential crosstalk. Figure 5.16 shows the measured weighting potential crosstalk with and without sub-pixel sensing. As shown, measured the sub-pixel crosstalk is much finer than that without sub-pixel sensing.

5.8 Conclusion

The purpose of this article is to introduce and justify a sub-pixel calculation algorithm based on the digital readout of the induced signal on the charge collecting pixel and its 8 neighbors. Without such a method, the lateral position resolution of pixelated, 3-D position sensitive, CdZnTe detectors is limited by their pixel pitch. This barrier introduces a significant limitation on the Compton imaging angular resolution. To improve lateral position resolution to the sub-pixel scale, algorithms based on signals induced on pixels that neighbor a charge collecting pixel are used. The opposing-neighboring ratio method is shown to be capable of providing accurate estimates of sub-pixel electron cloud centroid position. A detailed system simulation predicted 180- μm FWHM position resolution at 662 keV with 4-keV electronic noise. A collimator experiment resulted in a 360 μm position fluctuation for a 662 keV ^{137}Cs source. After subtracting the uncertainty caused by the collimator beam width and the electron cloud size, the experimental sub-pixel position resolution for measuring



(a) Without sub-pixel sensing



(b) With sub-pixel sensing

Figure 5.16: The measured weighting potential crosstalk as a function of distance and depth. The blank region is because the distance is too close that no crosstalk data can be obtained. The unit of the crosstalk amplitude is keV. This data is obtained from detector # 4E3 with the cathode biased at -3000V and the grid biased at -40V. This detector is a $20 \times 20 \times 15$ mm³ CdZnTe detector made by eV product.

the electron cloud centroid of a recoil electron is found to be about $230\text{ }\mu\text{m}$. The uncertainty of measured gamma-ray interaction position would then be $330\text{ }\mu\text{m}$ at 662 keV if we assume the secondary electrons are emitted isotropically.

Besides the opposing-neighboring ratio, two additional methods (neighbor-to-center ratio and corner-neighbor ratio) are discussed for the more difficult case of multi-pixel charge collection events. It is demonstrated that neighbor-to-center ratio method is effective in estimating the sub-pixel interaction position for two-pixel events.

Some benefits of sub-pixel position sensing are demonstrated. Generally speaking, the energy resolution can be improved using sub-pixel position correction and Compton imaging quality can be better because of more precise determination of interaction location. There are other benefits such as diagnosis of material properties, correction of sub-pixel material property change in those non-uniform detectors and so on, which could be a direction for further study.

CHAPTER VI

Energy and Depth Reconstruction with UM-VAD System

6.1 Introduction

The UM_VAD ASIC is a unique ASIC, which provides the signal waveform instead of only signal amplitude and timing for radiation interactions. The rich information each signal waveform carries can help to better determine the energy, position and even category of the interaction. This chapter describes the traditional way to use filters to perform the data processing to demonstrate the ASIC performance. The next chapter will discuss a new method based on the concept of system response function to explore the new capability of the ASIC.

6.2 Signal Processing

6.2.1 Energy Determination

In chapter II, for charge collecting anode pixels, the performance of various types of traditional filters as well as two fitting methods is investigated and summarized in figure 6.1. The trapezoid filter is found to have the best performance among the traditional filters. The matched-model fitting method has better performance but it

requires the knowledge of the waveform profile, which is unavailable unless the system response function is calculated. Therefore, we choose the trapezoid filter to calculate the signal amplitude.

For cathode signals, figure 6.1 shows the performance of various traditional filters with the measured electronic noise and waveform profile. The electronic noise and the waveform profile are measured separately and then added together to imitate real waveforms as described in chapter II. Those imitated waveforms are used for the cathode filter performance evaluation. As shown the trapezoid filter still has the best performance.

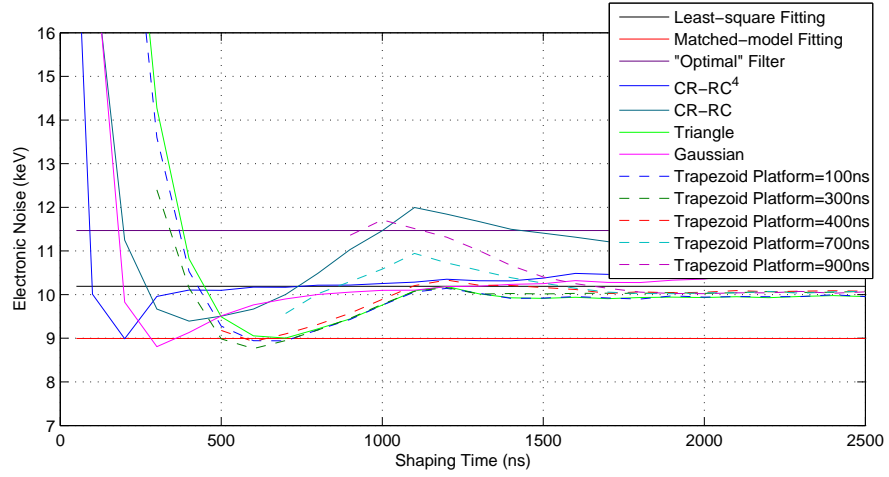


Figure 6.1: Filter performance for cathode signals. The noise and waveform profile is obtained on detector # 3E2 with cathode biased at -2500V and grid biased at -30V.

6.2.2 Timing Determination

Experimentally, the drift time of an electron cloud is obtained through the difference of the trigger time between the cathode signal and the anode signal. It should be noticed that this drift time is different from the true electron cloud drift time because anode signals rise and generate triggers before the electrons reach the anode surface. Drift time is used to reconstruct interaction energy and depth for multi-pixel-triggered

events as discussed in chapter I.

The filters of small shaping time (or fast shaper as we call it) are usually employed for drift time determination. The trigger time of the cathode and anode signals is determined by the moment when the filtered signal passes the threshold. If the threshold is a constant value, the obtained trigger time changes with signal amplitude, which is called time amplitude walk or TAW.

The BNL ASIC uses the time when the filtered anode signal reaches maximum as the anode trigger time, which helps to avoid the anode TAW. We employ this maximum trigger time method in this article to investigate the performance. For cathode trigger time, we assume the electric field inside the detector is uniform and the cathode signals rise linearly so that we can use linear fitting to find out the rising start time of the cathode signals. Additionally, we also have implemented the fast filter method. However, instead of using a constant value as the threshold, we use certain percentage of the maximum of the filtered signal as the dynamic threshold, which is also widely used to avoid TAW [26].

Figure 6.2 shows the best percentage threshold for the fast shaper method for anode signals. Figure 6.3 shows the timing performance of various filters. The electronic noise is added to the waveform profile and then fed into the filters to calculate the filter performance as described in chapter II. As shown, the fast shaper method has better performance than the maximum trigger time method. As for the best filter, figure 6.3 shows there isn't too much difference in anode timing resolution from one filter to another when the fast shaper method is utilized. In addition, all anode timing resolution is in the range of several nano second, which is roughly equivalent to 100 μm or even less. The depth resolution in a pixellated CdZnTe detector is usually measured at about 0.5 mm [24]. Therefore, anode isn't the major contributor to depth uncertainty. The choice of anode fast filter isn't critical. There is no need to choose anode fast filter very carefully. From figure 6.3, 50-ns shaping time should be

good enough for any anode fast filter.

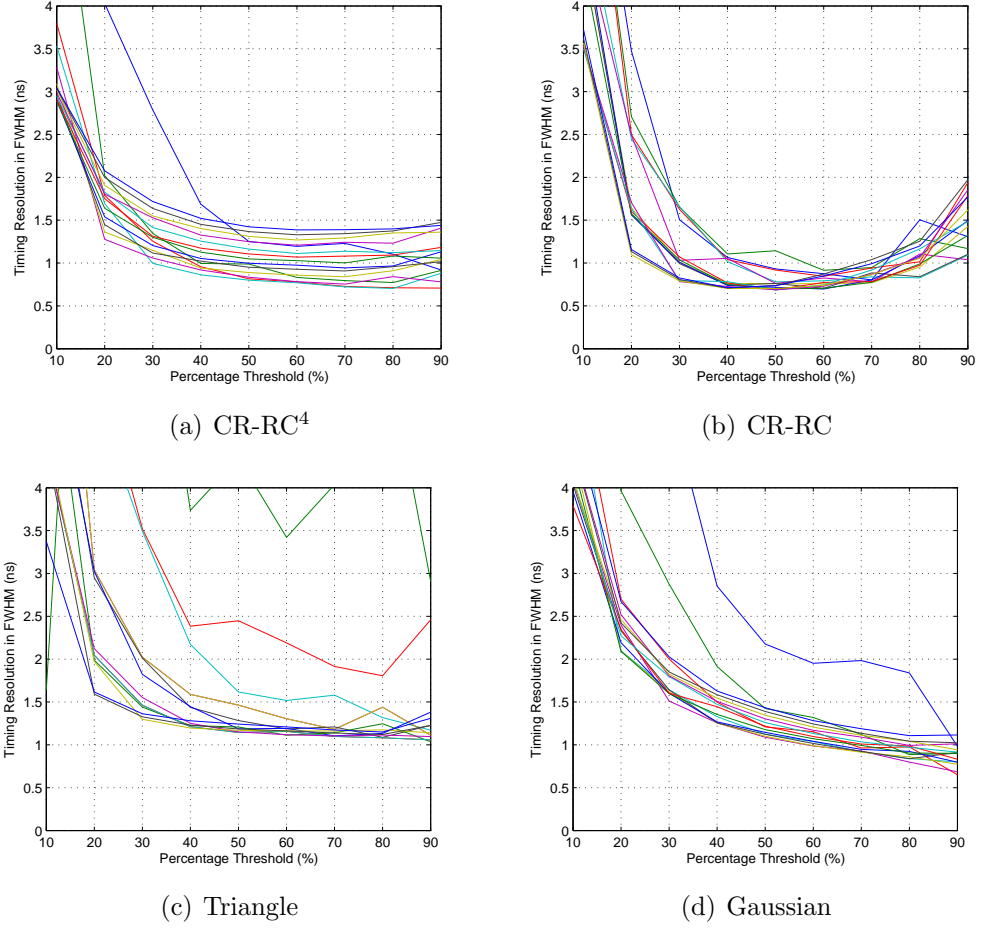


Figure 6.2: The timing resolution versus the percentage threshold. The different color represents different shaping time. The noise and waveform profile is obtained on detector # 3E2 with cathode biased at -2500V and grid biased at -30V. The energy deposition is assumed to be 662 keV.

Cathode signals are usually much noisier than anode signals because of larger electrode capacitance and leakage current. Figure 6.4 plots the trigger time uncertainty obtained by various types of filters. As shown the best cathode trigger time uncertainty is about 20 ns, which is much higher than the best anode trigger time uncertainty as shown in Figure 6.3. Therefore, the uncertainty of drift time and the resolution of depth which is calculated from the drift time, are dominated by the cathode noise. Ultimately, timing filters are chosen to optimize the depth un-

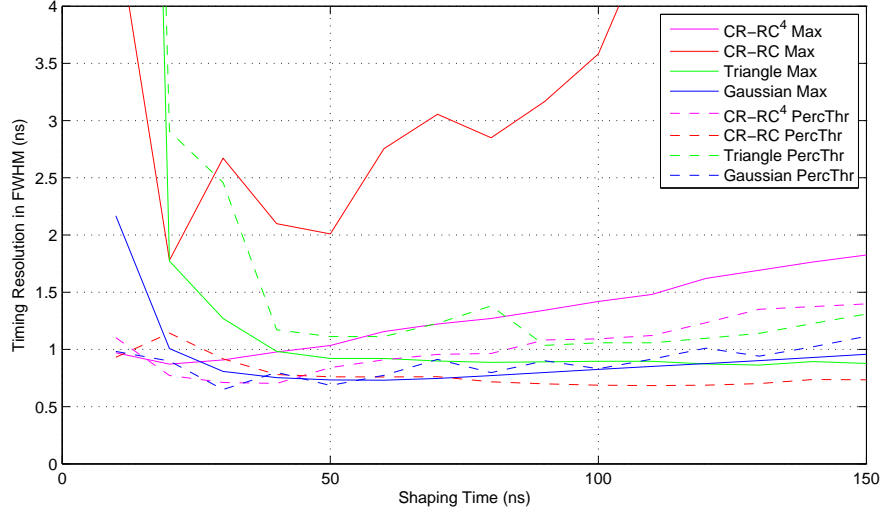


Figure 6.3: The timing performance of various filters for anode signals. The percentage threshold is set to be 50%. The noise and waveform profile is obtained on detector # 3E2 with cathode biased at -2500V and grid biased at -30V. The energy deposition is assumed to be 662 keV.

certainty. Therefore, depth resolution is taken as a reference to search for the best cathode timing filter.

In fact, the cathode signal is a function of interaction depth. As a result, the range of drift time, or the difference of drift time between the anode side interactions to the cathode side interactions, varies with the timing filter. For example, when the shaping time of a CR-RC⁴ filter changes from 100 ns to 1000 ns, the drift time range can vary from 600 ns to 400 ns. The interaction depth can be estimated through drift time by the equation

$$d = \frac{T - T_A}{T_C - T_A} \times D = \frac{T - T_A}{T_{range}} \times D \quad (6.1)$$

Where, T_A and T_C are drift time for anode and cathode side interactions respectively, T_{range} is the drift time range and D is detector thickness. If drift time range is small, even if the cathode trigger time resolution is excellent, the depth resolution is not necessarily to be good. Therefore, the depth resolution is a better standard to judge the performance of the cathode timing filters.

Figure 6.5 shows how the depth resolution varies with the percentage threshold. Figure 6.6 presents the depth resolution for various types of filters when the best percentage threshold is chosen, including the linear fitting method. As shown, the linear fitting method has the worst performance.

The percentage threshold is a function of energy deposition. When the energy is too low, the percentage threshold may fall below the noise. There is a energy limit for each percentage threshold. If we require the percentage threshold to be greater than 3-times noise variance, the energy limit can be calculated, which is plotted in figure 6.7 as a function of shaping time. The energy limit should be as low as possible to ensure the effectiveness of the percentage threshold at low energy range.

Taking into account both depth resolution and energy limit, the Gaussian filter with a shaping time of 150 ns is chosen as the cathode fast shaper and the percentage threshold is chosen to be 50%.

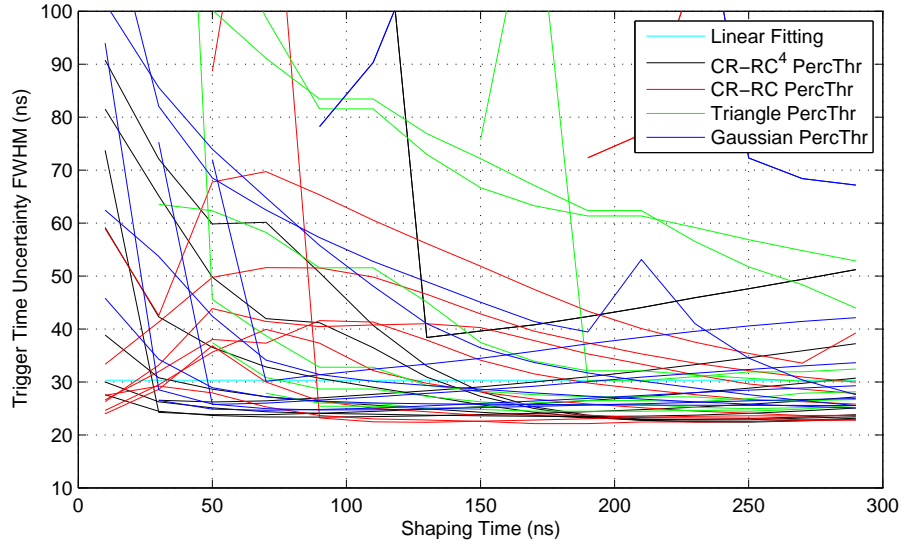
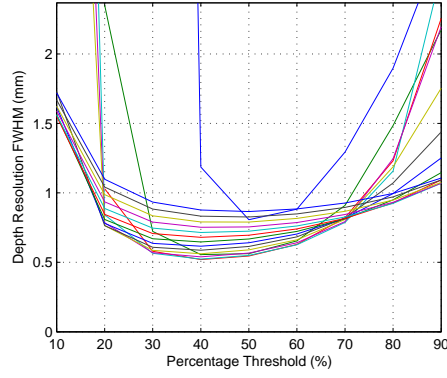
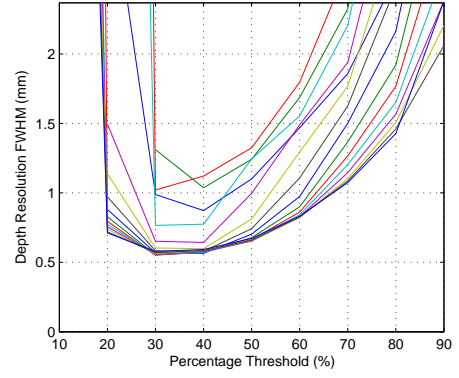


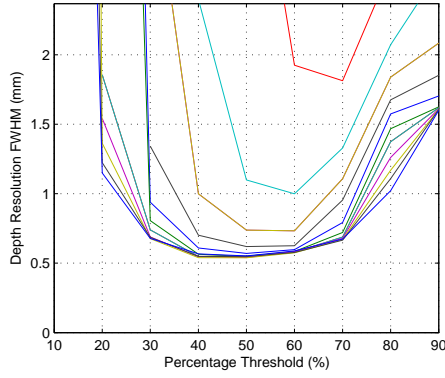
Figure 6.4: The trigger time resolution obtained through various types of filters for cathode signals. Different lines of the same color are for those cathode waveforms from different depth. The noise and waveform profile is obtained on detector # 3E2 with cathode biased at -2500V and grid biased at -30V. The energy deposition is assumed to be 662 keV.



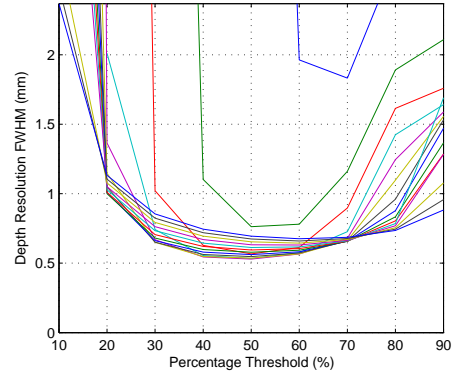
(a) CR-RC⁴



(b) CR-RC



(c) Triangle



(d) Gaussian

Figure 6.5: The depth resolution versus the percentage threshold. The noise and waveform profile is obtained on detector # 3E2 with cathode biased at -2500V and grid biased at -30V. The energy deposition is assumed to be 662 keV.

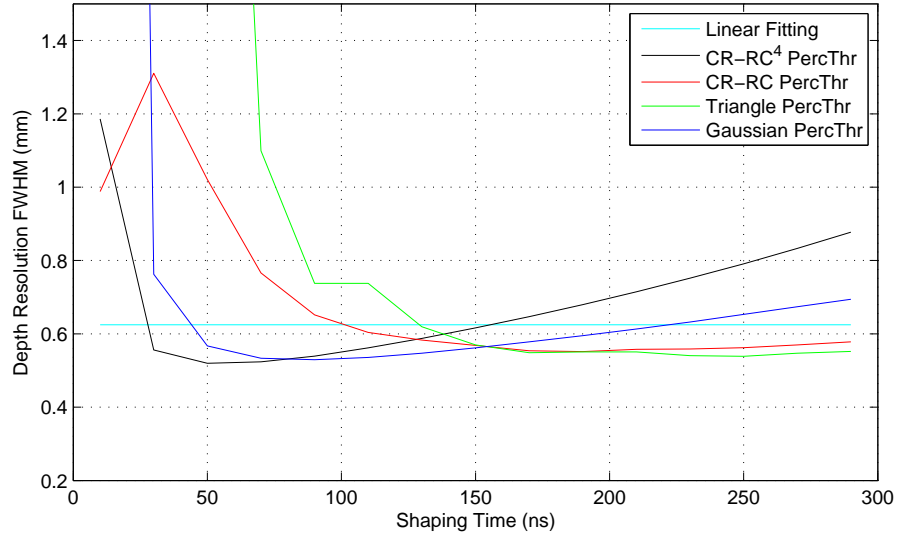


Figure 6.6: The performance of various types of filters for cathode signals. The noise and waveform profile is obtained on detector # 3E2 with cathode biased at -2500V and grid biased at -30V. The energy deposition is assumed to be 662 keV.

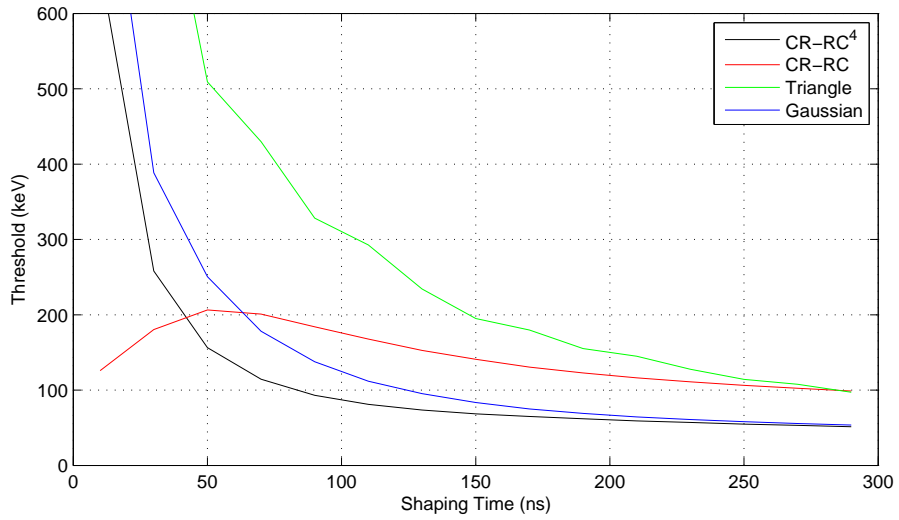


Figure 6.7: The energy limit of the fast shaper method using percentage threshold. The minimum percentage threshold is 3-times noise variance. The cathode side signals are used. The noise and waveform profile is obtained on detector # 3E2 with cathode biased at -2500V and grid biased at -30V. The energy deposition is assumed to be 662 keV.

6.3 Experimental Results

6.3.1 Single-pixel Events

6.3.1.1 Energy Resolution

Figure 6.8, figure 6.9 and figure 6.10 shows the reconstructed energy spectrum for single-pixel events without sub-pixel correction for several detectors. Since UM_VAD ASICs can slow down the sampling frequency as talked in Chapter IV, they can be used to measure different types of detectors. Traditional ASICs are only designed for one type of detector such as CdZnTe. If the detector material changes, the electron drift time and leakage will also change and the induced signals and the electronic noise will be different. Therefore, traditional ASIC needs to be designed for each type of detector material. For example, the ASICs designed for HgI₂ detectors can't be used for CdZnTe detectors. However, the UM_VAD ASIC is different. As shown by Figure 6.10, the same UM_VAD ASIC were used for detector # 1C37, a HgI₂ detector and good energy resolution was obtained.

Figure 6.11 gives a comparison of the measured single-pixel spectrum using the old analog VAS_TA ASIC and the UM_VAD ASIC. As discussed in Chapter IV the electronic noise in the UM_VAD ASIC is about 3 keV, which is similar to the VAS_TA ASIC. Therefore, we expect the UM_VAD ASIC to present a similar performance as the VAS_TA ASIC using traditional digital filters without sub-pixel correction. This performance similarity is proved with detector # 4E3 as shown in Figure 6.11. The performance degradation of detector # 3E2 using the UM_VAD ASIC is believed to be because of detector material degradation instead of any ASIC problem. As shown by the resolution map in Figure 6.8, lots pixels have extremely poor resolution. Those poor pixels were good pixels in the measurement using the VAS_TA ASIC, which was performed two years before the the UM_VAD ASIC measurement.

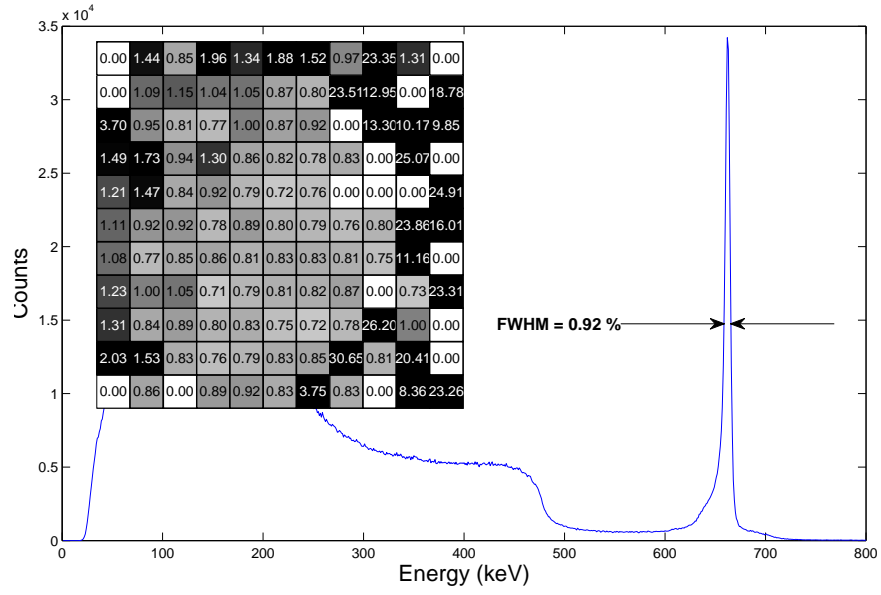


Figure 6.8: The performance of detector # 3E2 measured with the UM_VAD ASIC. The energy resolution for each pixel is shown by the resolution map located above the spectrum. Energy resolution equal to 0 means bad pixel or poor photopeak. The detector has its cathode biased at -2500 V and its grid at -30 V.

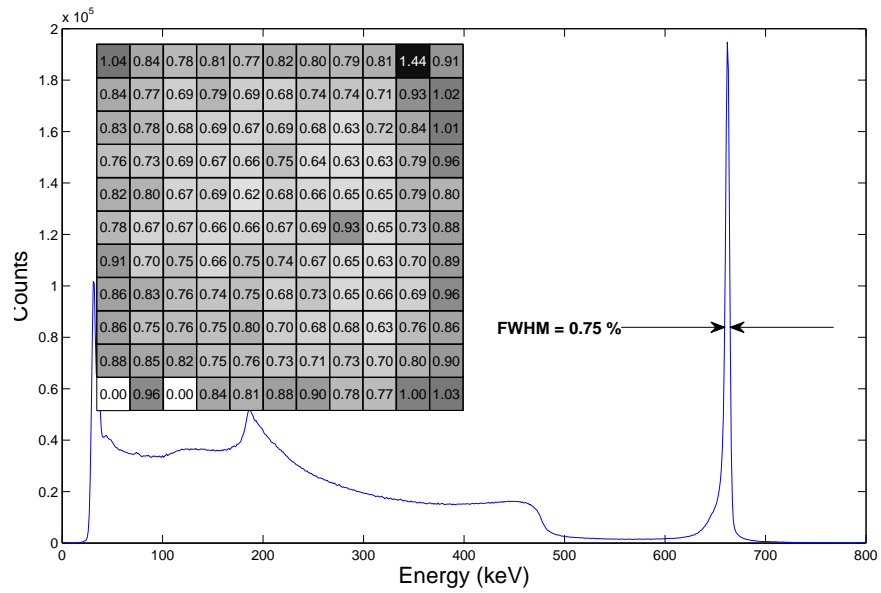


Figure 6.9: The performance of detector # 4E3 measured with the UM_VAD ASIC. The detector has its cathode biased at -3000 V and grid at -40 V.

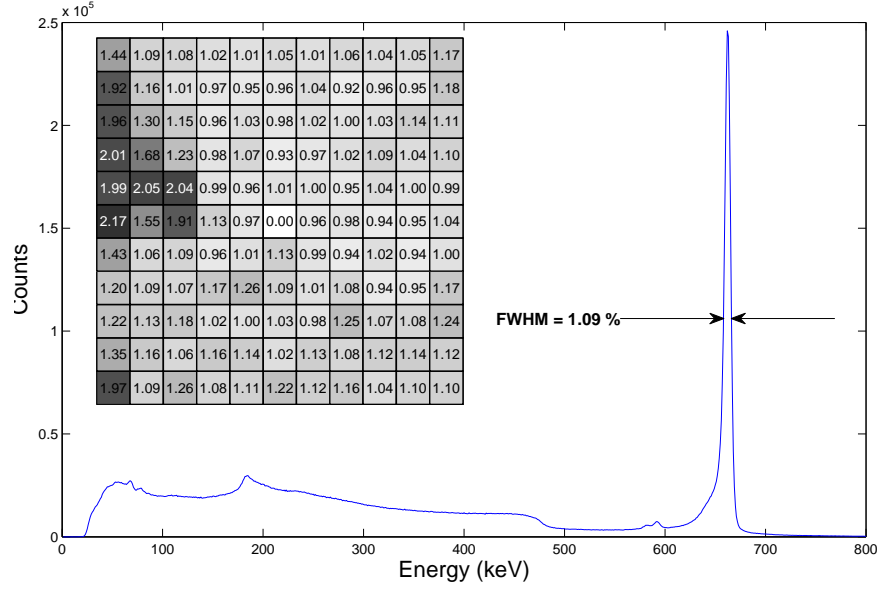
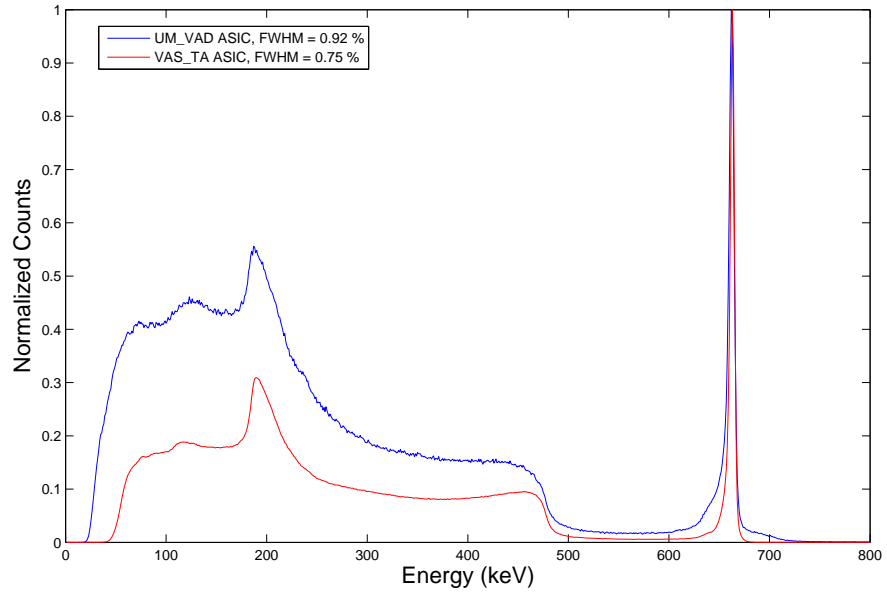


Figure 6.10: The performance of detector # 1C37 measured with the UM_VAD ASIC. The detector has its cathode biased at -4000 V and guard ring at 0 V. Instead of room-temperature, this result was obtained at 10°C.

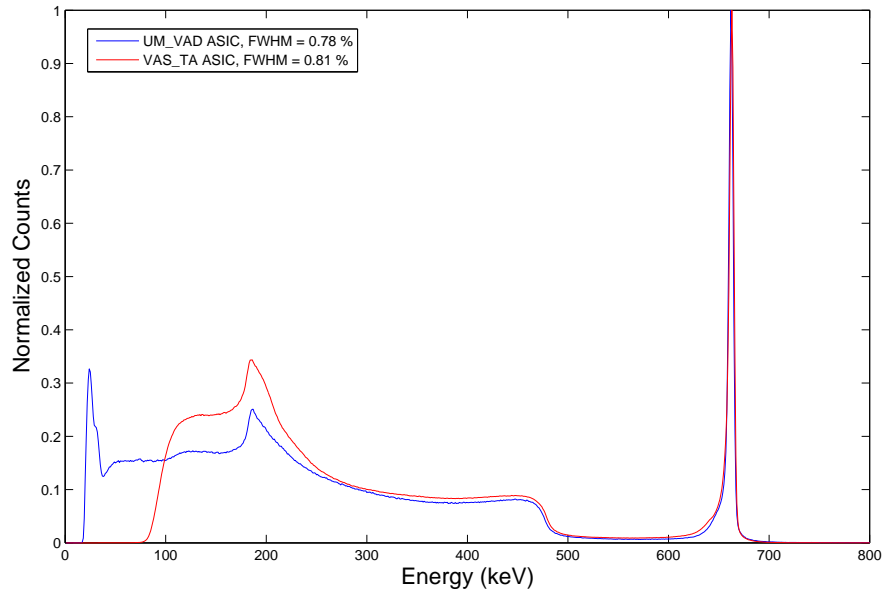
6.3.1.2 Drift Time

As discussed, we use percentage threshold to remove the TAW from the anode and cathode trigger time. To examine if the time amplitude walk has been truly removed, drift time distribution of single-pixel events from the same depth is plotted as a function of energy deposition in Figure 6.12. As can be seen, the drift time isn't a function of energy, showing that TAW has been removed with percentage threshold. In Figure 6.12, we can also observe that below 60 keV, the drift time uncertainty becomes very large. This is because the percentage threshold is very small at such low energy and it is close to the electronic noise.

The accurately drift time uncertainty has to be measured with collimator. However, we can estimate the uncertainty using the data we already have. As we know, there are two methods to determine interaction depth: C/A ratio and drift time. For both methods, the cathode noise is the major contributor to the depth uncertainty. If we investigate the distribution of drift time for a certain depth, the uncertainty of

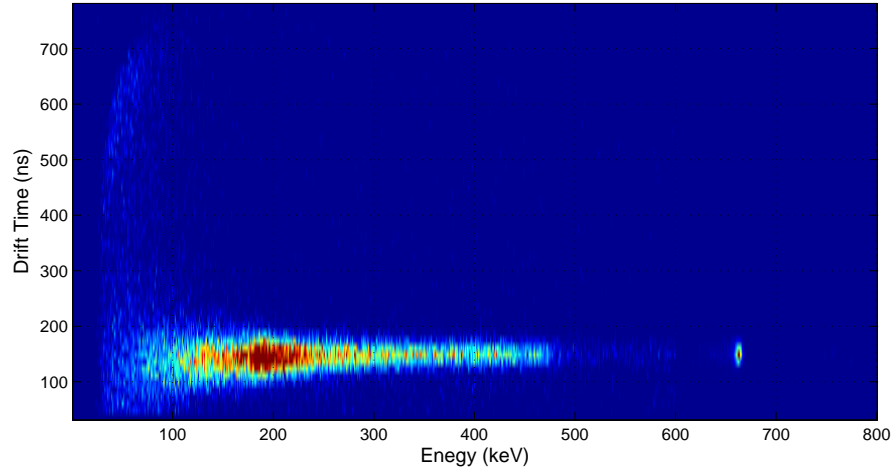


(a) 3E2

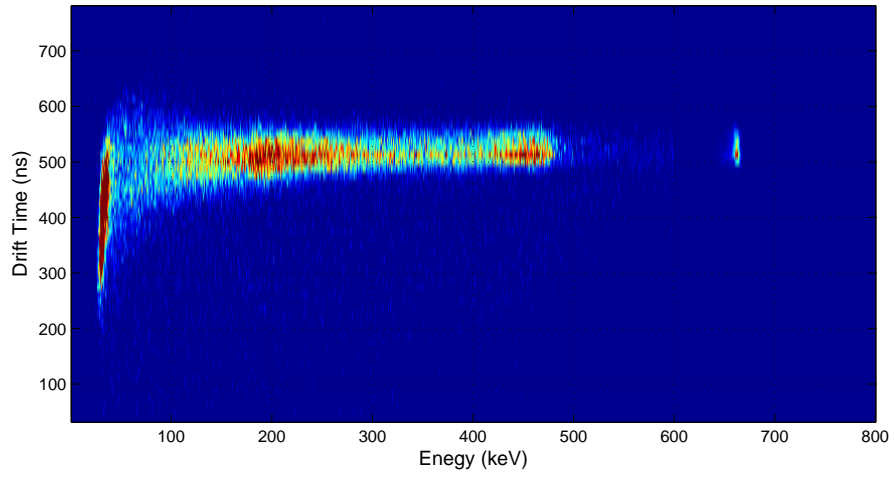


(b) 4E3

Figure 6.11: Comparison of the detector performance measured with the VAS_TA ASIC and the UM_VAD ASIC. Detector # 3E2 has its cathode biased at -2500 V and grid at -30 V. Detector # 4E3 has its cathode biased at -3000 V and grid at -40 V.



(a) 3.9 mm from the anode surface



(b) 13.8 mm from the anode surface

Figure 6.12: the drift time distribution as a function of energy deposition for single-pixel events. The data is obtained with detector # 4E3 with its cathode biased at -3000 V and grid at -40 V. The detector thickness is 15 mm.

this distribution, or sum uncertainty as we call it, includes C/A ratio uncertainty and drift time uncertainty. However, since for each measurement the electronic noise that causes the fluctuation of the C/A ratio and the drift time is actually the same, the sum uncertainty should be smaller than the quadratic sum of the depth uncertainty and the drift time uncertainty. For detector # 4E3, the sum uncertainty is measured to be 0.6 mm FWHM at 662 keV, indicating the depth uncertainty is better than 0.6 mm. As a comparison, the sum uncertainties measured on detector # 3E2 and detector # 4E3 using the VAS_TA ASIC are both around 0.9 mm, showing that cathode filters used in the VAS_TA ASIC is not optimized.

6.3.2 Multi-pixel Events

For multi-pixel events, the performance of the UM_VAD ASIC is presented in table 6.1. No sub-pixel correction is included in this result. Comparing to the VAS_TA ASIC, the UM_VAD ASIC performs better for multi-pixel events. As shown in the table, the degradation of the multi-pixel events energy resolution measured with the UM_VAD ASIC is slower than that with the VAS_TA ASIC: the ratio of the energy resolution is 1.00, 1.44, 1.85 and 2.13 from 1-pixel to 4-pixel events for the UM_VAD ASIC, while it is 1.00, 1.52, 2.13 and 2.59 for the the VAS_TA ASIC. Ideally, for multi-pixel events, the energy resolution should degrade only due to the increment of the electronic noise. Therefore, the energy resolution ratio should increase in a rate of 1, 1.44, 1.73 and 2. It is not the case for either ASICs. There are lots of factors that can be blamed of. For example, in the VAS_TA ASIC, it was found that the peak-hold circuit for the shaper has severe nonlinearity problem and it contributes a lot to the energy resolution degradation [24]. This example shows that the shaper and the timing picking circuit that follows the pre-amplifier can cause problems. The more complicated the ASIC circuit is, the more possible problems may occur. In this sense, the UM_VAD ASIC has an advantage. It only has pre-amplifiers, which

makes the UM_VAD ASIC more promising in the future to completely address the multi-pixel energy resolution degradation problem and reach the expected limit of the multi-pixel energy resolution.

Table 6.1: The energy resolution FWHM of detector # 3E2 for 1-pixel, 2-pixel, 3-pixel and 4-pixel events.

ASIC	1-pix	2-pix	3-pix	4-pix
UM_VAD	0.96%	1.38%	1.78%	2.04%
VAS_TA	0.75%	1.14%	1.60%	1.94%

6.4 Conclusion

This chapter uses the traditional filter method to investigate the performance of the UM_VAD ASIC. Because of the flexibility of choosing filter, the UM_VAD ASIC can produce better result comparing to old analog ASICs if the electronic noise is the same. It is also demonstrated that the UM_VAD ASIC can work for different types of detectors. Good performance has been achieved in a HgI₂ detector, whose induced signals are ten times slower than the signals in CdZnTe detectors.

CHAPTER VII

System Response Function and its Applications

7.1 Introduction

UM_VAD system provides a unique capability to obtain maximum amount of information of each radiation interactions through the induced signal waveforms. With those waveforms, energy deposition, interaction position and interaction types can be identified. Chapter VI has demonstrated one way to extract the energy deposition and interaction position using digital filters. This chapter shows an alternate way, which utilizing the concept of system response function.

System response function generally describes what kinds of output signal should be observed if an impulse input of a delta function is fed into the system. In our case, it tells the induced signal profile and amplitude when a single electron-hole pair is generated at a certain location in the detector and the electron and hole get collected by cathode and anode respectively. In fact, holes can only move limited distance in CdZnTe and their induced signal can be ignored as a first-order approximation. Therefore, the system response function of CdZnTe detectors is dominated by the electron component and can be treated as the induced signal of a single electron. Then, the total induced signal of an interaction is the sum of the signals produced by every electron of the electron cloud generated in this interaction, if we assume the formation of the total induced signal is a linear process:

$$S(t, E_1, \vec{X}_1, E_2, \vec{X}_2, \dots, E_n, \vec{X}_n) = \sum_{i=1}^n \sum_{j=1} m_i H(t, \vec{P}_{ij}) \quad (7.1)$$

Here, t is time, representing that the induced signal is a function of time. n is the number of interactions. E_1, E_2 until E_n are energy deposition of each interaction. \vec{X}_1, \vec{X}_2 until \vec{X}_n are the interaction locations. m_i is the number of the electrons in the i -th electron cloud generated by each interaction. \vec{P}_{ij} is the location of i -th electron in the j -th electron cloud. It can be also considered as the distribution of electron cloud. $H(\vec{P}_{ij})$ is the system response function, namely, the signal produced by an electron located at \vec{P}_{ij} . If $H(\vec{P}_{ij})$ is known, this equation can be used to find out what is the most probable distribution of electron cloud (\vec{P}_{ij}) that best matches the measurement $S(t, E_1, \vec{X}_1, E_2, \vec{X}_2, \dots, E_n, \vec{X}_n)$. The distribution of an electron cloud is a very useful piece of information. However, it requires lots of computation power to solve the equation and sometimes it isn't necessary. The total charge and center location of the electron cloud for a interaction are adequate enough in terms of readout information for many applications. If we ignore the change of induced signal due to the electron cloud shape variation as a first-order approximation, the system response function can be written in a simpler form as $H(t, \vec{X}, E)$, where \vec{X} is the center location of a electron cloud and E is the energy deposition. In addition, if we further assume that in the range of energy deposition of our interest, the size of any electron cloud is small enough so that the change of induced signal can be treated as a linear function of location. The linearity gives an advantage that no matter how large is the electron cloud, the total induced signal is only a function of the electron cloud location, which means the system response function can be written as $H(t, \vec{X}, E) = E \cdot H(t, \vec{X})$.

If we have a measured signal $S(t)$ and we have obtained the system response function $H(t, \vec{X})$, how to calculate the location and energy of this interaction? One

answer is to use least-square fitting, namely, to minimize the error function:

$$e = \int (S(t) - E \cdot H(t, \vec{X}))^2 dt \quad (7.2)$$

By making $de/dE = 0$ and $de/d\vec{X} = 0$, we can form a group of equations to solve. However, the derivative of the system response function $H(t, \vec{X})$ can't be expressed analytically and therefore equation 7.2 can't be solved directly. There is a function minimization method called Levenberg-Marquardt algorithm that can be used to find fitting solutions. In this algorithm, the numeric value of the derivative of $H(t, \vec{X})$ can be used and the solution to equation 7.2 can then be calculated.

7.2 Generation of System Response Function

The system response function $H(\vec{P}_{ij})$ is defined as the induced signal produced by a single electron, in other words, a point response function. In reality it is very difficult to directly measure such system response function. In fact, if an electron cloud is small enough, it should have very similar induced signal profile as a single electron. To determine if an electron cloud is small enough, one can compare its size with the size of the interested electrode, which in our case is the size of anode pixels. If an electron cloud is much smaller than the pixel size, we can expect

1. The variation of induced signal along lateral location inside the electron cloud is small so that the induced signal can be considered as a linear function of position. As a result, the total induced signal is only related to the center position of the electron cloud and isn't correlated to the electron cloud size.
2. When electrons drift to the anode surface, the collection delay time of some electrons because of the size of the electron cloud is much smaller than the signal rise time and for this reason it won't cause significant change of signal

profile. It should be mentioned that the induced signal on an anode pixel rises only when the electron cloud is about one-pixel away from the anode surface. Therefore, the condition that electron cloud size is much smaller than the pixel size can ensure the signal rise time much bigger than the collection delay time.

In this case, the measured induced signal should resemble the system response function of the original definition. As for the simplified system response function $H(t, \vec{X})$, since it is obtained under the small electron cloud assumption, it is obviously the same as the induced signal measured with small electron clouds.

Chapter V provides a method to sense the geometrical center of electron clouds in sub-pixel resolution. Base on this method, a matrix of system response inside a 3-dimensional mesh (x,y for lateral position and z for depth) can be forged.

To measure the system response function, several factors should be considered: how large the ionized electron cloud would be, how high the signal to noise ratio is, how convenient and how efficient the measurement can be performed. As discussed, the size of electron cloud needs to be small to make sure the measured system response function is close to the point response function. For example, muon can't be used to measure the system response because its track can be as large as the size of the whole detector. There are two lab sources that can be considered: 662-keV ^{137}Cs gamma-ray source and 5.64-MeV ^{241}Am alpha source. The advantages of ^{241}Am source are it has very high signal to noise ratio and its ionized electron cloud size is very small. However, 5.54-MeV alpha has very short range, which is about tens of micrometers in CdZnTe [46]. It will only interaction at the detector surface and won't be able to generate signals in detector bulk. Additionally, ^{241}Am alpha source can't be placed outside of the detector enclosure.

It will be totally blocked by the detector enclosure. Therefore, using ^{241}Am to measure the system response function requires complete disassembling of the detector system, which is not convenient in practical operation. Alpha also can be easily

blocked by any objects on the cathode surface such as detector name tag, conducting paste of the high voltage wire and so on. As a result, some pixels may have no alpha signals and as a result the system response function measured with alpha can be incomplete. As a comparison, 662-keV photons don't have the range problem. However, the signal-to-noise ratio of the induced signals of 662-keV photons is much poorer than those produced by 5.64-MeV alphas. In addition, the detection efficiency of photons is much smaller than alphas. However, those disadvantages won't lead to crucial problems such as missing of the system response function for several pixels. Therefore, 662-keV photon source is the better choice.

The system response function is measured on a 3-dimensional mesh and linearly interpolated to any arbitrary location inside the detector. This data mesh has to be fine enough to make sure the accuracy of the linear interpolation. Along the depth, traditionally we divide the whole detector thickness to 40 depth, which has been proven to be precise enough [50]. Along lateral direction, the sub-pixel resolution is anticipated to be around $300\text{ }\mu\text{m}$ with about 3 keV electronic noise as demonstrated in chapter V. Taking into account that in the future the UM_VAD system targets at 2 keV electronic noise, we choose to separate each pixel into 9 divisions. The total divisions or voxels in this mesh is close to 400,000.

To solve the problem of low signal-to-noise ratio of the induced signal for 662-keV photons, we collect many waveforms inside one voxel and average them. The number of events inside each voxel needs to be large enough to ensure the removal of electronic noise. In addition, it should be noticed that the induced signal actually changes inside each voxel. Our interest is the response at the center of each voxel. This also needs to be achieved by averaging induced signals in one voxel. Therefore, even with very good signal-to-noise ratio, enough number of events in each voxel is still required. For 40 depths and 9 sub-pixels in each pixel, 400,000 voxels need to be filled, which is a significantly huge number. For example, if we only require 100

photopeak events in each voxel to generate the system response, the total photopeak events we would need is about 40 million. The photopeak efficiency is about 10% in CdZnTe. Therefore, it is required to acquire totally 400 million events. This number of events will not only require a lot of time to collect but also tremendous amount of disk space to store. The first version UM_VAD system has high common mode noise and it can only work in full-readout mode, which has a maximum count rate of 200 counts per second. Therefore, it will take 20 days to acquire 400 millions events. As for disk space, the waveforms of this much events will consume about 3 Tera-Byte which is unrealistic to store. In order to obtain the system response function for the whole detector with reasonable number of events, we have to use approximations to reduce the number of voxels in the mesh.

In this section, we talk about how to obtain system response function with the 662-keV ^{137}Cs source. The techniques to reduce the number of voxels in the mesh and overcome the problem of low signal-to-noise ratio and low efficiency is the focus of this section.

7.2.1 Charge-collecting Pixels and Cathode

As we discussed in chapter V, the induced signal changes laterally inside the charge-collecting pixel. However, this change is small especially in the bulk of the detector as shown in section 5.7.2 in chapter V. In addition, we have achieved significant energy resolution of 0.48% FWHM at 662 keV on the best detector we have [52] using the BNL ASIC without any correction of sub-pixel variation, indicating the poorer energy resolution of around 1 % measured in other detectors or using other ASICs isn't caused by the sub-pixel variation of induced signals. This statement is correct at least for good CdZnTe crystals. Therefore, the system response function of charge-collecting pixels can be generated without considering sub-pixel variation and the number of divisions in the mesh can be reduced from 400,000 to less than 5,000.

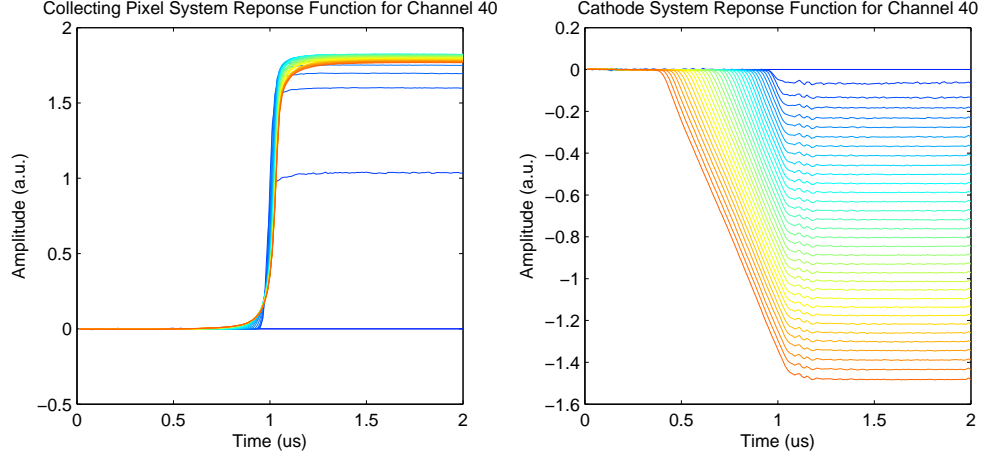


Figure 7.1: An example of the system response function measured for collecting pixel and cathode. Channel 40 is picked for this example. With the color changes from blue to yellow and then to red, the depth varies from the anode side to the cathode side.

Figure 7.1 presents an example of calculated system response function for the charge-collecting pixels and the cathode. From anode to cathode, the amplitude of the cathode waveform increases almost linearly except for those depths very close to the anode surface. For a charge-collecting pixel, from anode to cathode, its signal waveform first gets bigger because of the increment of weighting potential and then starts to decrease when the interaction is in the detector bulk because of electron trapping. Those observations are expected. There are several other interesting features existing in those plots, which are going to be discussed later.

7.2.2 Neighboring Pixels

Different from the charge collecting and cathode signals, the induced signals on the neighboring pixels are quite sensitive to the lateral location of the interaction inside the charge-collecting pixel, which is the basis of the sub-pixel sensing. To reduce the number of divisions of the mesh for neighboring pixel signals, we investigate the possibility to ignore or compensate the difference of the neighboring pixel signals for those interactions located in the same depth and the same relative sub-pixel location

but under different collecting pixels. If the signal difference can be either ignored or compensated, the system response function mesh then becomes a function of depth and relative sub-pixel location instead of global location and the size of the mesh can be reduced significantly to about 3,000.

There are several factors that can contribute to the variation of the neighboring pixel signals as the collecting pixel changes. Those factors include weighting potential, trapping, electric field and electronic gain. Some of the factors have the influence that can be corrected easily. For example, the different electronic gain among pixels can be measured with test pulse and corrected by simply multiply each channel by a constant. For other factors, we need to investigate one by one to determine if their influence can be compensated or not.

First, let's take a look at weighting potential. Since the detector is not infinitely large, the weighting potential between any two collecting pixels or neighboring pixels aren't exactly the same, especially if we compare the center pixels with the edge and corner pixels. Figure 7.2 shows the weighting potential of those left neighboring pixels calculated by Maxwell v12. As shown, the weighting potential curves of the inner-layer pixels are very similar. However, for the edge and corner pixels, their weighting potential can vary as much as two times from the weighting potential of the inner layer pixels. Apparently, the edge and corner pixels should be excluded in the pixel-combining method. After the system response function for the inner-layer pixels has been determined, one can combine with simulation to estimate the system response function for those corner and edge pixels.

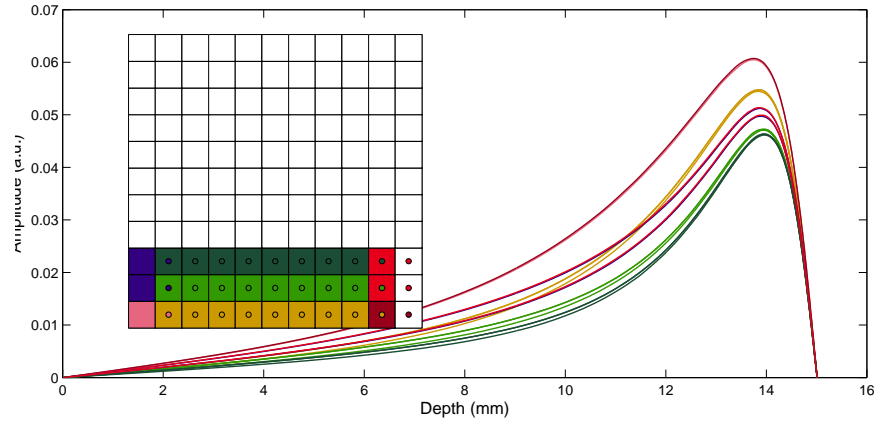
There is one important feature that should be noticed: if the neighbor is far away from the interaction location, whether this neighbor is a corner, edge or inner-layer pixel has significant impact on the weighting potential; on the other hand, if the neighbor is close to the interaction location, the identity of this neighbor will influence much less significant. This feature makes the sub-pixel position calculation

algorithm is insensitive to the identity of the neighbors if the collecting pixel belongs to inner 9 by 9 pixels and all 8 neighbors exist.

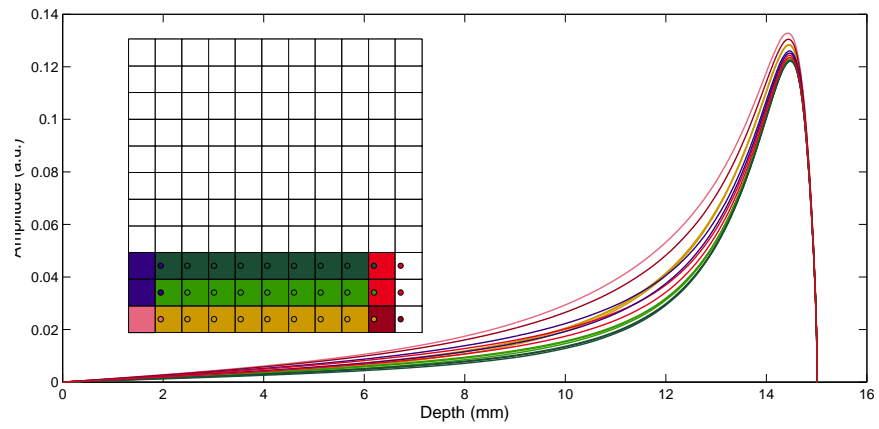
The trapping of electrons can change the induced signal waveform. For example, trapping defines how curved the cathode signal waveforms are. If there is severe trapping, the cathode signal waveform would be very curved instead of a linear function as observed in many moderate and low trapping detectors if the electric field is uniform. However, the induced signals on the neighboring pixels are very small in the detector bulk. It rises when the electron cloud reaches the anode vicinity. Since trapping takes place mostly in detector bulk, the influence of trapping to the induced signal on the neighboring pixels can be approximately treated only as amplitude change instead of the variation of the waveform shape. By applying a simple gain correction, the influence of the trapping is expected to be almost totally removed. Figure 7.3 shows an example. As can be seen, when the total trapping changes from 5% to 10%, the change of the signal waveform is negligible. Usually, for good CdZnTe detectors, the change of trapping from pixel to pixel is smaller than 5%. Therefore, trapping isn't expected to be a problem to apply the pixel-combing method.

Lastly, the electric field can be different from pixel to pixel. We have observed such a case in some Redlen CdZnTe detectors [24]. The electron drift velocity is a function of electric field. Therefore, the change of electric field can change the signal waveform profile. If the difference is significant, the width of the measured neighboring pixel waveforms would be different. Figure 7.4 shows the neighboring pixel waveforms for all inner-layer pixels, there is no visible difference in signal profile that is more prominent than the electronic noise. In fact, the cathode signal contains the electron velocity and therefore the electric field difference can be fully corrected if it is required.

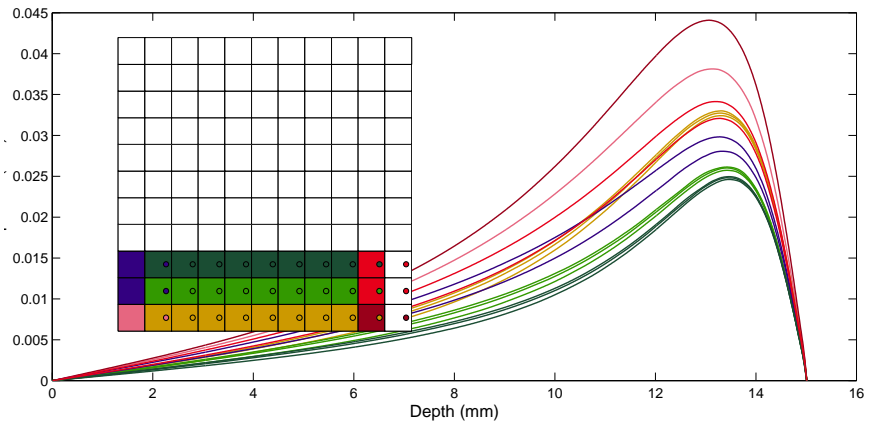
Therefore, we apply the pixel-combining method to obtain the system response function for inner-layer pixels. Figure 7.5 presents an example of the measured system



(a) At the center of the pixel



(b) Near the left edge of the pixel



(c) Near the right edge of the pixel

Figure 7.2: The calculated weighting potential difference for various interaction locations. Each colored line is the weighting potential for the pixel of the same color. Each colored circle marks the interaction location of the pixel with the same color.

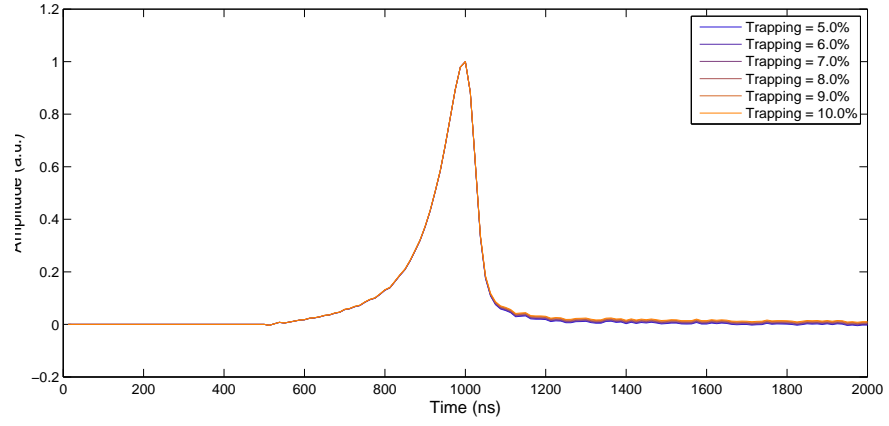


Figure 7.3: The influence of trapping on the neighboring pixels. The signal waveform is obtained from experimental data. The trapping is added artificially. The final waveforms are normalized to have the same maximum value.

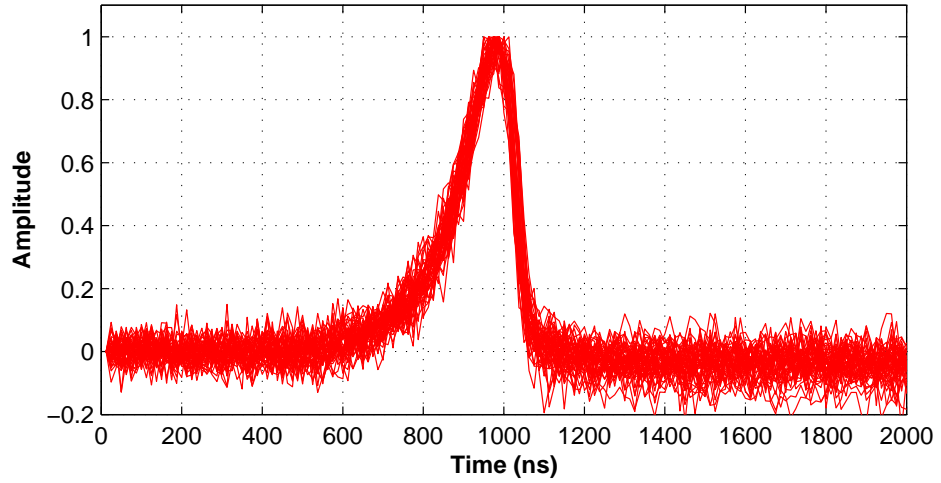


Figure 7.4: Comparison of the normalized induced signal on the right side neighbor when the electron cloud is located at different collecting pixels.

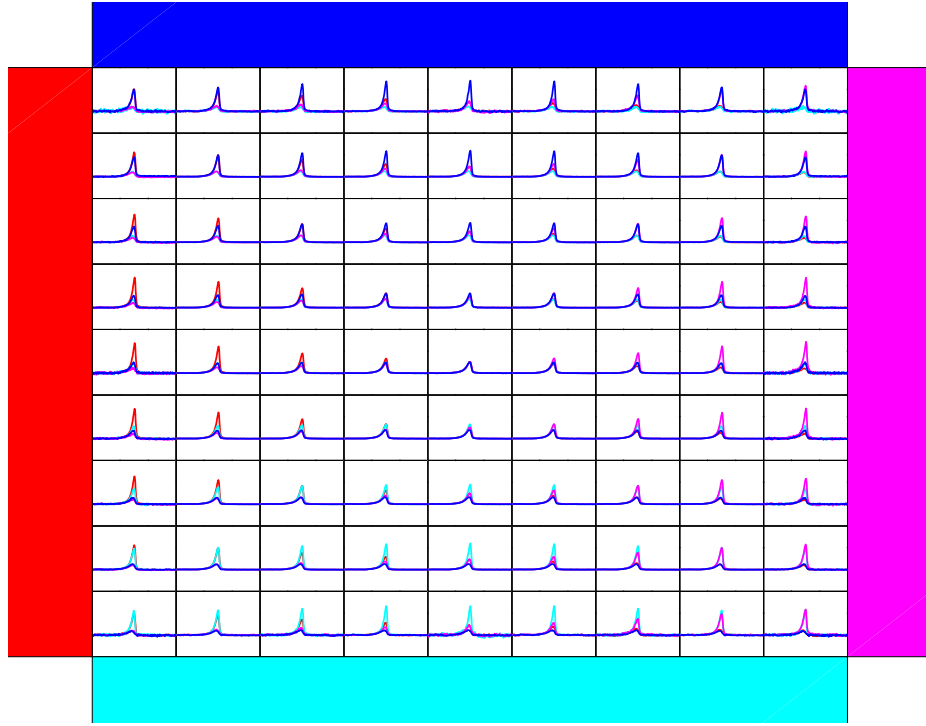
response function for the neighboring pixels.

7.2.3 Charge Leak Correction and SRFSF Method

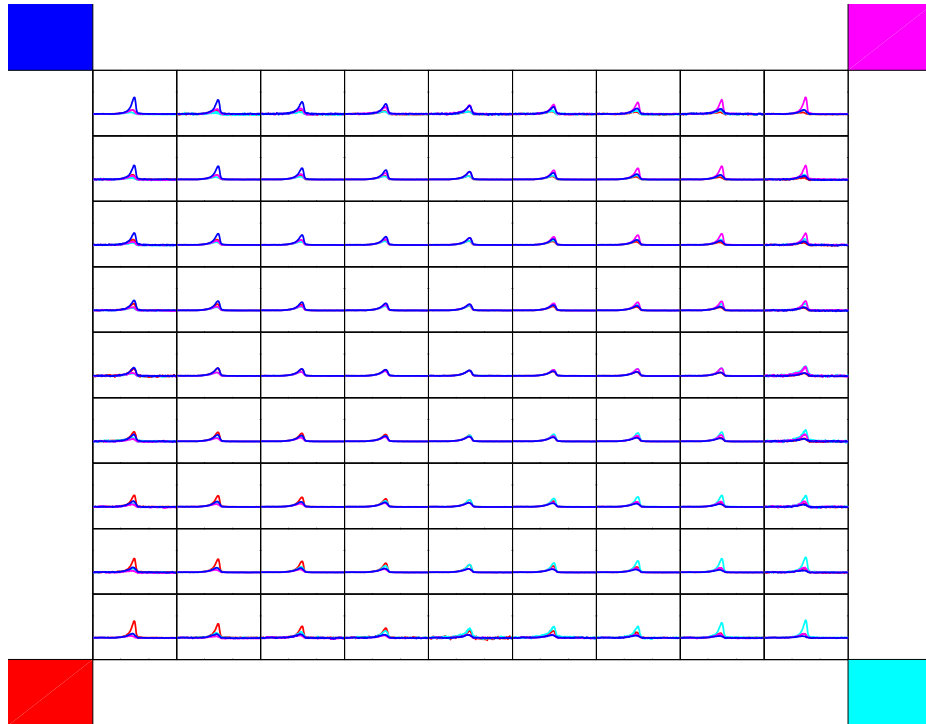
As we know, if the interaction location is very close to the edge of the pixel, some charge will be leaked to one or even several neighboring pixels. A 662-keV electron cloud produced by a fast electron is about 200 to 300 μm . When using this electron cloud to generate the system response function for the neighboring pixels, charge leak can happen in the edge and corner sub-pixel voxels. Figure 7.6 shows a example of the charge leak observed in the measured system response function. The tail amplitude of the induced signal on the the neighboring pixel tells how much charge is collected on this pixel. It can be seen in this figure that 7 neighbors share the same tail amplitude while the other has a bigger tail. The same tail amplitude of the 7 neighbors tells that for the depth of this example, the tail amplitude is not a sensitive function of the sub-pixel location. Therefore, the true tail amplitude without charge leak can be known. Then obviously, the neighbor that has bigger tail amplitude is because of charge leak. The amount of leaked charge can be calculated and it can be used to correct the measured system response. Figure 7.6 shows the corrected system response for those 8 neighbors.

However, the 8 neighbors are not necessarily to have the same tail amplitude for all depths. Figure 7.7 gives an example of the system response for the 8 neighbors when the interaction depth is close to the anode surface. It can be clearly seen that the tail amplitude for those neighbors varies significantly. To figure out how much charge is leaked for those anode side system response, a method called system response function self-fitting (SRFSF) is invented.

The idea of SRFSF is to use the cathode surface system response to deduce the system response of the other depths based on waveform fitting. As we know, when there is no trapping, the induced signal is just a function of weighting potential. If we



(a) Side neighbors



(b) Diagonal neighbors

Figure 7.5: The measured system response function of the neighboring pixels for 9×9 at depth 30, which is about 3.2 mm away from the cathode surface. The different colored lines are the induced signals from the neighboring pixel of the same color.

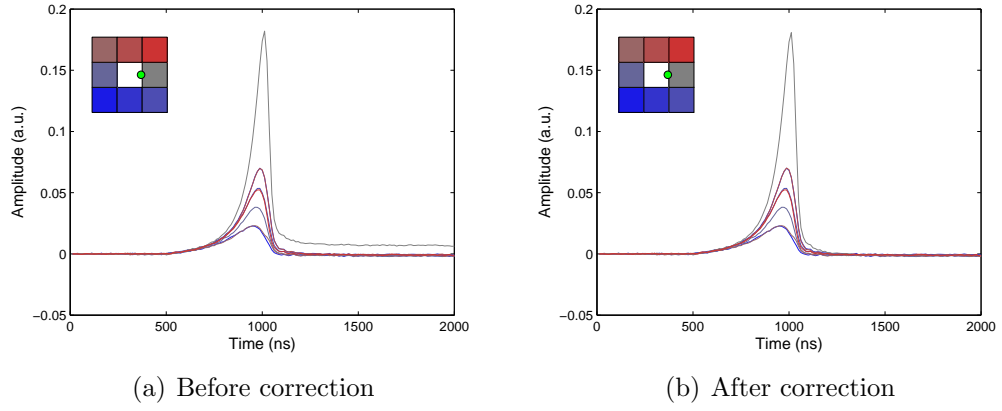


Figure 7.6: The measured system response function for 8 neighbors at depth 30, which is about 3.2 mm away from the cathode surface. The different colored lines are the induced signals from the neighboring pixel of the same color. The green dot marks the interaction location.

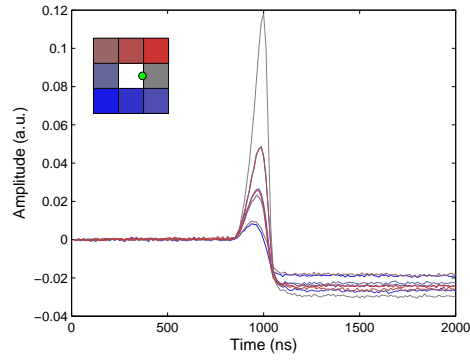


Figure 7.7: The measured system response function for 8 neighbors at depth 10, which is about 3.9 mm away from the anode surface. The different colored lines are the induced signals from the neighboring pixel of the same color. The green dot marks the interaction location.

fix the lateral interaction location and only let the depth vary, it is easy to find that the induced signal of any depth is just a part of the induced signal of the cathode surface. This statement is true even if there is trapping. We can reach this conclusion with the derivation below.

The induced signal at the cathode surface can be written as

$$w(t) = - \int_0^t n_0 e^{-\frac{t}{\tau}} E(x(\vec{t}')) v(x(\vec{t}')) dt' \quad (7.3)$$

Here, $w(t)$ is the induced signal. τ is electron life time. $x(\vec{t})$ is the position of the electron cloud at time t . $E(\vec{x})$ is the electric field strength along depth direction at position \vec{x} and $v(\vec{x})$ is the electron drift velocity. $E(\vec{x})$ and $v(\vec{x})$ are only a function of position. $w(t)$ can be related to the induced signal from an interaction at an arbitrary position $\vec{x}_0 = x(\vec{t}_0)$ as

$$\begin{aligned} w(t) &= - \int_0^t n_0 e^{-\frac{t'}{\tau}} E(x(\vec{t}')) v(x(\vec{t}')) dt' \\ &= - \int_0^{t_0} n_0 e^{-\frac{t'}{\tau}} E(x(\vec{t}')) v(x(\vec{t}')) dt' - \int_{t_0}^t n_0 e^{-\frac{t'}{\tau}} E(x(\vec{t}')) v(x(\vec{t}')) dt' \\ &= C - \int_0^{t-t_0} n_0 e^{-\frac{t'+t_0}{\tau}} E(x(t' + \vec{t}_0)) v(x(t' + \vec{t}_0)) dt' \\ &= C + e^{-\frac{t_0}{\tau}} \cdot \left[- \int_0^{t-t_0} n_0 e^{-\frac{t'}{\tau}} E(x(t' + \vec{t}_0)) v(x(t' + \vec{t}_0)) dt' \right] \end{aligned} \quad (7.4)$$

Since E and v are both only a function of position, $-\int_0^{t-t_0} n_0 e^{-\frac{t'}{\tau}} E(x(t' + \vec{t}_0)) v(x(t' + \vec{t}_0)) dt'$ actually gives the induced signal at time $t - t_0$ of an interaction happened at position

\vec{x}_0 , which is in the path of the $w(t)$ electron cloud drifting to the anode.

$$\begin{aligned}
w(t) &= C + e^{-\frac{t_0}{\tau}} \cdot \left[- \int_0^{t-t_0} n_0 e^{-\frac{t'}{\tau}} E(x(t' + t_0)) v(x(t' + t_0)) dt' \right] \\
&= C + e^{-\frac{t_0}{\tau}} \cdot w_{\vec{x}_0}(t - t_0) \\
&= C + K \cdot w_{\vec{x}_0}(t - t_0)
\end{aligned} \tag{7.5}$$

$w_{\vec{x}_0}(t)$ is the induced signal when the interaction happens at position \vec{x}_0 . K is electron trapping ratio and C is the expected induced signal when the electron cloud drifts from the cathode to the interaction position. Both K and C aren't a function of time. Therefore, even with trapping, the induced signal from any interaction depth can be deduced by the induced signal on the cathode surface with simple transformation and SRFSF is expected to work. De-trapping isn't considered here. Its effect will be discussed in section 7.4.2.

SRFSF can provide the expected signal profile for any interaction depth based on the cathode surface system response function. By comparing the expected neighboring signal waveform with the measured one, the amount of charge leak can be found out. As a summary, after the system response function is measured for the neighboring pixel events, three additional procedures can be applied to correct the charge leak for those sub-pixel locations near the pixel edge:

1. Applying the charge leak correction based on signal tail comparing for those the cathode side system responses.
2. Using the system response in the center of the pixel to calculate the parameter C and K for each depth.
3. Use the calculated C and K and charge-leak-corrected cathode-surface system response to obtain the response function of the other depths and all charge leak will be removed.

It should be noticed that C and K are both insensitive to the sub-pixel location, so that C and K calculated using the pixel-center system response function can be applied to the pixel-edge system response function.

7.3 Numeric System Response Function Fitting

Numeric system response function fitting follows the procedure of Levenberg-Marquardt algorithm and uses linear interpolation to obtain the Jacob matrix. Figure 7.8 shows the flow chart of the fitting procedure. Figure 7.9 gives an example of this fitting method for a single-pixel event. As seen, the anode and pixel waveforms can be fitted pretty well. Every detail of the measured waveform matches the fitted system response function. However, for neighboring pixel waveforms, there is still some small disagreement. Relative high noise can be responsible, but the approximations we have made to calculate the neighboring pixel system response function should also contribute.

7.4 Application of System Response Function

There could be numerous applications of the system response function. In this section, we discuss two of them.

7.4.1 Charge Leak Correction for single-pixel events

As discussed, some charge can leak to the neighbor pixels when the interaction is near the pixel edge. With accurate system response function, this loss of charge can be recovered. As shown in Figure 7.10, after the charge leak correction, the photopeak becomes more symmetric and the low energy tail becomes much smaller. For multi-pixel events and high energy events, the low energy tail of photopeak is more severe. It is expected that the charge leak correction can help more in improving the

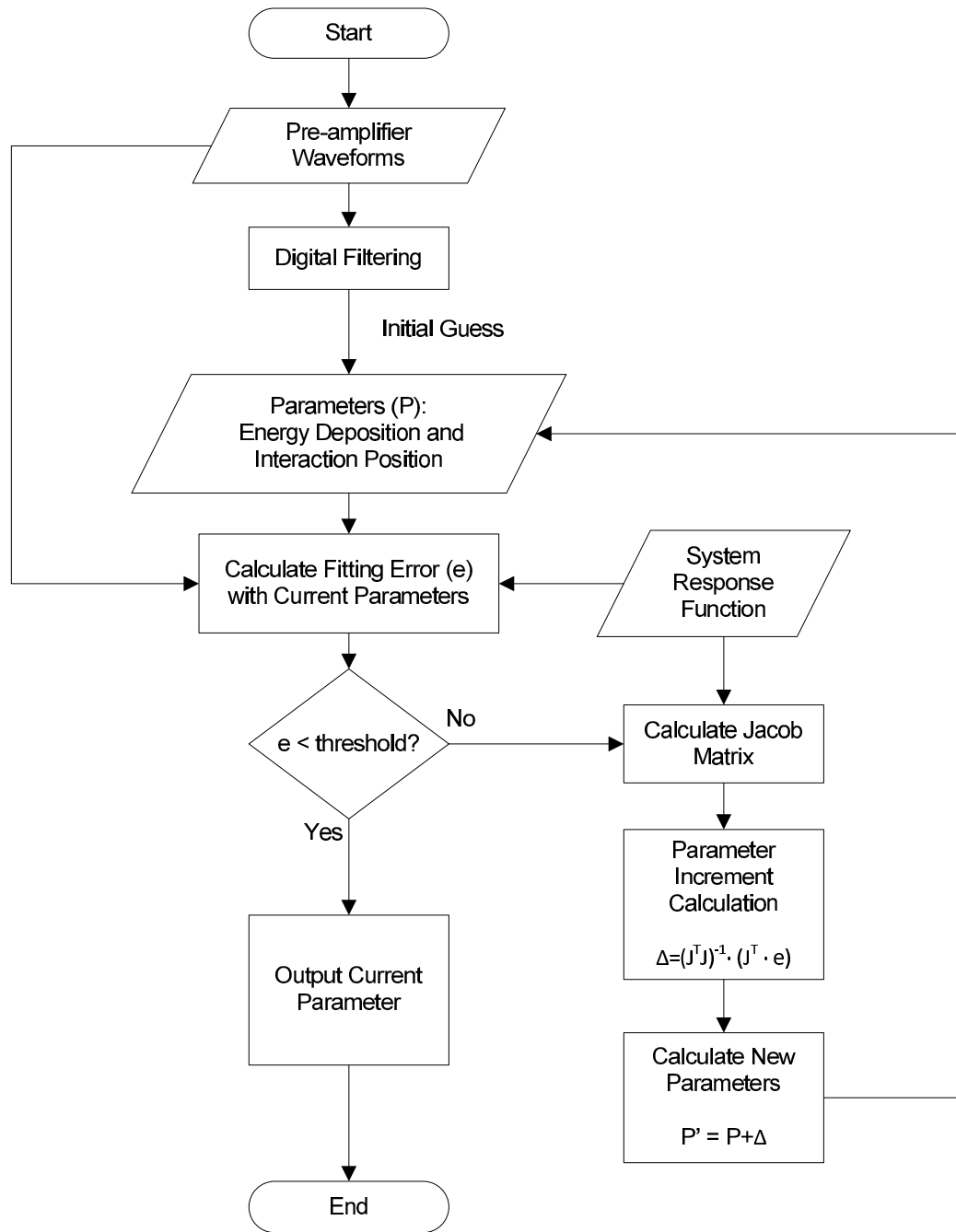


Figure 7.8: The flow chart of the system response function fitting algorithm.

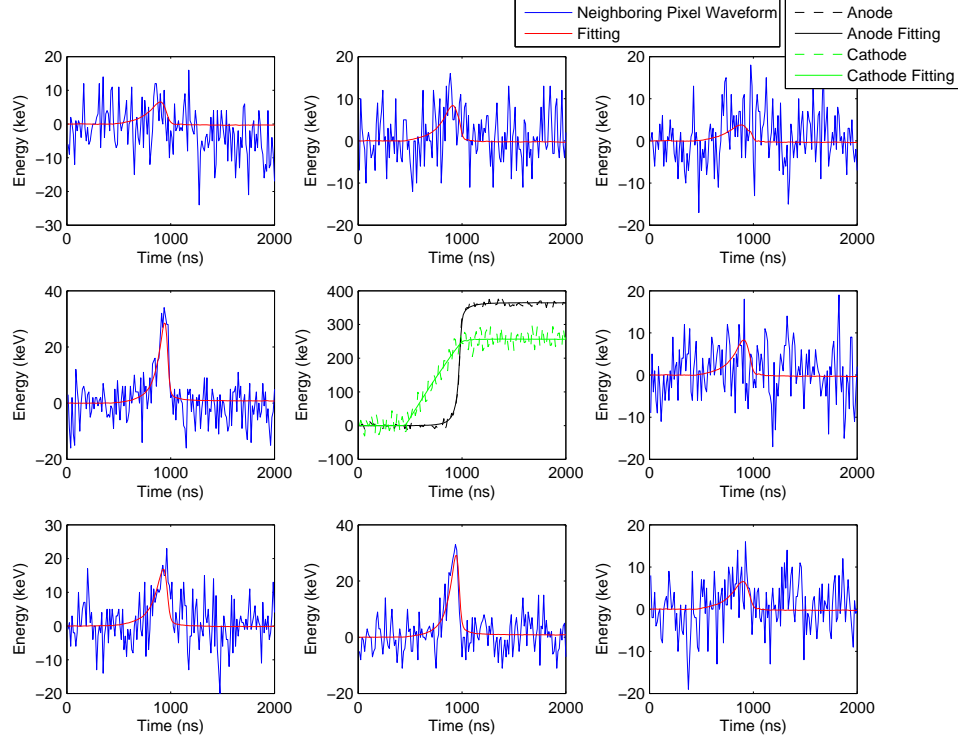


Figure 7.9: An example of SRF fitting method applied to a single-pixel event.

photopeak shape and energy resolution for those events.

7.4.2 Electron De-trapping Time Measurement

When we apply the SRF method, it is found that the cathode surface system response can't perfectly match the system response from the other depths. Figure 7.11 shows an example. The best fitting has a clear difference at the turning part of the waveform when the charge is being collected by the pixel. The fitted waveform, which is in fact the system response at the cathode surface, turns slower than that of the anode waveform. If we calculate the area of the difference of the two curves and plot the change of this area as a function of the interaction depth, it can be found that from the cathode to the anode side the turning difference always exists as shown in figure 7.12. This observation shows that the holes can't be responsible because their contribution to the anode signals is very small in the detector bulk. The de-trapping

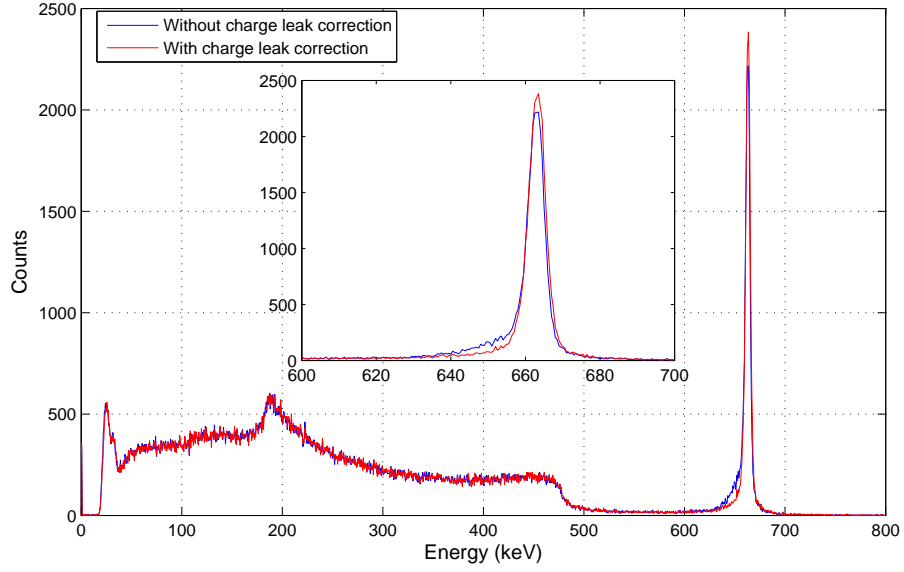


Figure 7.10: The single-pixel event spectrum before and after the charge leak correction. The data is obtained from detector # 4E3. The cathode is biased at -3000 V and the grid is at -40 V. The energy resolution is slightly improved from 0.81% to 0.80%.

of the trapped electrons could be the reason. The trapping and de-trapping process can delay electrons and eventually make the electron cloud elongated. The electron cloud that drifts more distance will experience more trapping de-trapping process and its size will become bigger. As a result, cathode side electron clouds need more time to be fully collected and then the turning part of their induced signal will last longer, which is exactly what we observed in figure 7.11.

Equations can be derived to estimate the trapping time and de-trapping time based on the SRFSF fitting difference. Here, we roughly estimate their values. Figure 7.13 illustrates the method. As plotted in the figure, the total delay of the collection time is about 200 ns. Usually electrons needs about 5-time de-trapping time to be fully de-trapped. Therefore, the de-trapping time should be around 40 ns. As for the trapping time, we know that every time there is trapping, the electrons will be delayed. The electrons remains in the leading edge of the electron cloud are those un-trapped electrons. The fast rising of the anode signal then can be found as caused by those

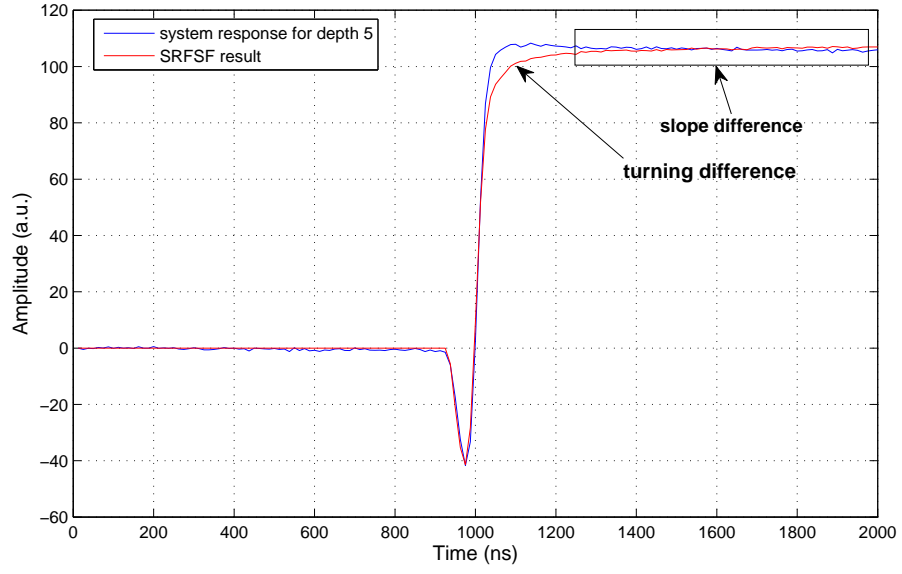


Figure 7.11: An example of the SRFSF method for the system response of a neighboring pixel. The turning difference indicates fast electron trapping and de-trapping. Depth 5 is about 5 mm away from the anode surface.

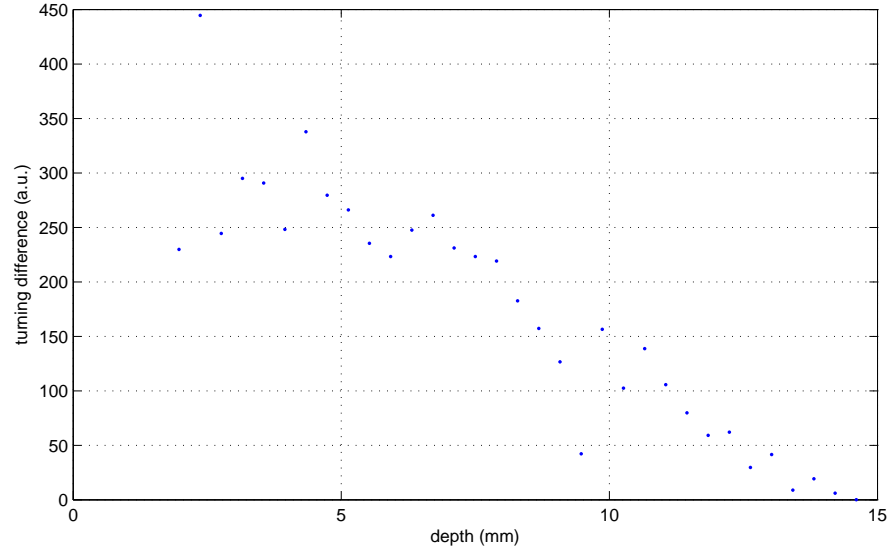


Figure 7.12: The area of the turning difference as a function of the interaction depth.

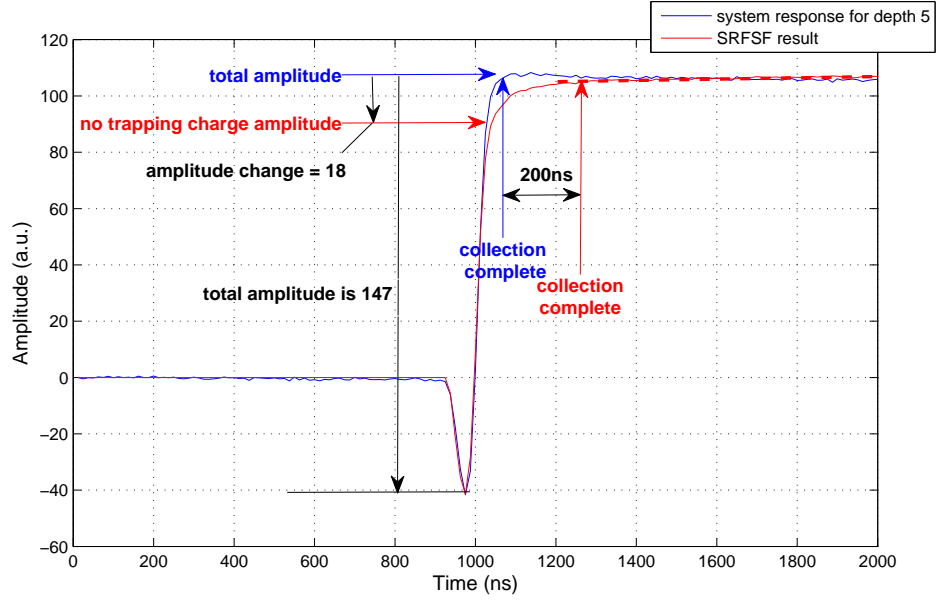


Figure 7.13: An example of the SRFSF method. The turning difference indicates fast electron trapping and de-trapping. Depth 5 is about 5 mm away from the anode surface.

un-trapped electrons. Therefore, the quantity of those electrons can be measured by the amplitude where the fast rising of the anode signal stops. From Figure 7.13, we can determine that the trapping time is about $5 \mu\text{s}$. Here, a puzzle emerges. The 40-ns de-trapping time should ensure all electrons to be de-trapped if they are trapped with the $5 \mu\text{s}$ trapping time. However, in this detector, the waveform amplitude as a function of depth clearly shows the existence of the trapping of electrons. It is suspected that in this detector, there are two trapping centers: one is shallow and the other is deep. The shallow trapping center has the 40-ns de-trapping time and contributes to the round turning of the induced signal while the the deep one has very long de-trapping time and is responsible of the observed electron trapping.

7.5 Conclusion

This chapter presents a new method called system response function fitting to obtain the energy and position information from the digital waveforms from the

UM_VAD ASIC. The method to generate the system response function is discussed. The biggest difficulty is the huge mesh size of the system response function if sub-pixel precision is included. To overcome this problem, we treat charge-collecting pixels and neighboring pixels differently. For charge-collecting pixels, the sub-pixel variation of the induced signal is ignored and the data is focused on capture the energy deposition variation from pixel to pixel. For the neighboring pixels, the variance of the neighboring induced signals for the same relative sub-pixel location and depth but different charge collecting pixels is ignored or compensated. The focus is put on the signal change because of the relative sub-pixel position variation. Additionally, the method to correct the pollution of the charge leak on the neighboring pixel system responses is provided. The charge leak correction is tested with single-pixel events and is proven to be effective.

The best place to use system response function reconstruction is for high energy events or neighboring pixel events. In fact, when the energy deposition is high, the neighboring pixel events will have severe crosstalk, which can be confused with the small charge leak or trigger the timing incorrectly in traditionally ASICs such as the VAS_TA ASIC. [24]. However, with system response function, those crosstalk can be identified and removed easily.

CHAPTER VIII

Electron Cloud Distribution

8.1 Introduction

In previous several chapters, the position measurement we have done was to find out the centroid of electron cloud. The distribution of electron cloud was ignored. However, the electron cloud distribution carries lots of information which would be very useful if known. For example, the Compton imaging that have implemented for many years in semiconductor devices has no information of electron recoil direction and therefore it relies on the crossing of many cones to tell the source location. This method generates lots of background counts in the image. If the electron cloud distribution which in this case is the recoil electron track is known, the possible incoming gamma-ray direction would be limited to a fragment of the cone or just a point if the measured recoil direction is very precise. As a result, the image background would be dramatically reduced and the signal-to-noise ratio would be improved. Additionally, electron cloud distribution shows the process of ionization. It is different between electrons and other heavy charged particles. Therefore, if the electron cloud distribution can be known particle ID can be performed.

This chapter discusses a method to de-convolve the electron cloud distribution from a careful system response function based on Maximum-Likelihood Expectation Maximization (MLEM) algorithm. The preliminary simulation result is presented.

8.2 Electron Cloud Distribution Calculation algorithm

8.2.1 Problem Model

Let's use $m(t)$ to present the total induced signal on an electrode, $p(x, y, z, t)$ as the system response function for this electrode, namely the induced signal by an electron starting drift from the location (x, y, z) and $c(x, y, z)$ as the distribution of electron cloud, or energy deposition at position (x, y, z) . Since the signal inducing is a linear process, $m(t)$ can be easily written as a integration of $c(x, y, z)$ and $p(x, y, z, t)$

$$m(t) = \int_v c(x, y, z) p(x, y, z, t) d\vec{v} \quad (8.1)$$

If we assume the electron cloud is completely under one pixel and divide this pixel into $I \times J \times K$ sub-voxels along x, y (in anode plane) and z (in depth) direction respectively, equation 8.1 can be written discretely as

$$m(t) = \sum_{i,j,k} c(i, j, k) p(i, j, k, t) \quad (8.2)$$

Where (i, j, k) is the coordination of the sub-voxel and $t = 1, 2, 3, \dots, T$ is the number of samples. If let $b = i + j \times I + k \times J \times K$ and $B = I \times J \times K$, equation 8.2 can be rewritten to a even simpler form

$$m(t) = \sum_b c(b) p(b, t) \quad (8.3)$$

In real measurement, we have noise in the system, so that equation 8.3 becomes

$$m(t) = \sum_b c(b) p(b, t) + n(t) \Rightarrow n(t) = \sum_b c(b) p(b, t) - m(t) \quad (8.4)$$

Or in forms of vector and matrix, it turns into

$$\vec{n} = P\vec{c} - \vec{m} \quad (8.5)$$

Therefore, if we know the system response function $p(b, t)$ and the measured signal on the electrode $m(t)$, the problem is to find $c(b)$ to best fit the measurement.

8.2.2 Solution

8.2.2.1 Solving with Inverse Matrix

As discussed in chapter II, the electronic noise is correlated, so that least-square fitting isn't the best fitting method. We need to employ the matched-model fitting, which uses the joint distribution function of noise

$$f(\vec{n}) = K \cdot e^{-\frac{1}{2}\vec{n}'A\vec{n}} \quad (8.6)$$

Here A is the covariance matrix. With equation 8.5, we can obtain probability for electron cloud distribution \vec{c}

$$f(\vec{c}) = K' \cdot e^{-\frac{1}{2}(P\vec{c}-\vec{m})'A(P\vec{c}-\vec{m})} \quad (8.7)$$

The most probably \vec{c} should happen when

$$\frac{df(\vec{c})}{d\vec{c}} = 0 \quad (8.8)$$

Namely

$$\begin{aligned}
& \frac{d[(P\vec{c} - \vec{m})'A(P\vec{c} - \vec{m})]}{d\vec{c}} = 0 \\
\Rightarrow & P'A(P\vec{c} - \vec{m}) = 0 \\
\Rightarrow & (P'AP)\vec{c} = P'A\vec{m}
\end{aligned} \tag{8.9}$$

It's to solve a linear equation. The solution seems very easy to be obtained. However, \vec{c} is electron cloud distribution or the energy deposition at each sub-voxel so that it cannot be negative. Apparently, the solution in equation 8.9 doesn't guarantee \vec{c} to be positive. In fact, since the dimension of \vec{c} is huge, there is very high possibility that negative solutions can be obtained through equation 8.9. Therefore, we need another method that can add the confinement to the solution. Here we choose MLEM [42].

8.2.2.2 Solving with EM Method

To obtain MLEM solution, first we artificially split the noise into several variables and make each one of them connected to a voxel.

$$n(t) = \sum_b n(b, t) \tag{8.10}$$

For simplicity, we ignore the correlation of noise and assume $n(b, t)$ to be time independent and Gaussian shaped with the variance as σ_n . Then the signal amplitude at time t induced by those ionized electrons in voxel b is

$$s(b, t) = c(b)p(b, t) + n(b, t) \tag{8.11}$$

So that $s(b, t)$ has a Gaussian distribution. Its mean value is $c(b)p(b, t)$ and the variance is σ_n . We require $\sum_b s(b, t) = m(t)$ to connect the model to the measurement. The likelihood that energy deposition of a electron cloud $c(b)$ to produce the measured

signal $m(t)$ can be written as

$$L(\vec{c}) = P(\vec{m}|\vec{c}) = \prod_{b,t} K \cdot e^{-\frac{1}{2} \left[\frac{s(b,t) - c(b,t)}{\sigma_n} \right]^2} \quad (8.12)$$

To maximize $L(\vec{c})$, we can get

$$\frac{\partial L(\vec{c})}{\partial c(b)} = 0 \Rightarrow c(b) = \frac{\sum_t s(b,t)p(b,t)}{\sum_t p^2(b,t)} \quad (8.13)$$

The expectation of $s(b,t)$ if we know the measured signal $m(t)$ and electron cloud distribution $c(b)$, $E[s(b,t)|\vec{m}, \vec{c}]$ can be calculated as following. First we consider the noise is time independent, so that $s(b,t)$ is irrelevant of $m(t')$, $t' \neq t$, so that

$$E[s(b,t)|\vec{m}, \vec{c}] = E[s(b,t)|m(t), \vec{c}] \quad (8.14)$$

Next, we use the relation $m(t) = \sum_b s(b,t) = s(b,t) + \sum_{b' \neq b} s(b',t)$. Let $X = s(b,t)$ and then X has a mean value of $c(b)p(b,t) = X_0$ and a variance as $\sigma_n = \sigma_X$. Let $Y = \sum_{b' \neq b} s(b',t)$ and then Y has a mean of $\sum_{b' \neq b} c(b')p(b',t) = Y_0$ and a variance of $\sqrt{B-1}\sigma_n = \sigma_Y$. The total possibility to observe X when $X + Y = m(t)$ is

$$\begin{aligned} f(X|X+Y=m(t)) &= C \cdot e^{-\frac{1}{2} \left[\frac{(X-X_0)^2}{\sigma_X^2} + \frac{(m(t)-X-Y_0)^2}{\sigma_Y^2} \right]} \\ &= C' \cdot e^{-\frac{1}{2} \left[\left(\frac{1}{\sigma_X^2} + \frac{1}{\sigma_Y^2} \right) X^2 - 2 \left(\frac{X_0}{\sigma_X^2} + \frac{m(t)-Y_0}{\sigma_Y^2} \right) X \right]} \end{aligned} \quad (8.15)$$

Where C and C' are constants. This equation tells us that the mean value of X is

$$\begin{aligned} E[X|X+Y=m(t)] &= \frac{\frac{X_0}{\sigma_X^2} + \frac{m(t)-Y_0}{\sigma_Y^2}}{\frac{1}{\sigma_X^2} + \frac{1}{\sigma_Y^2}} \\ &= \frac{X_0 \cdot \sigma_Y^2 + (m(t) - Y_0) \cdot \sigma_X^2}{\sigma_X^2 + \sigma_Y^2} \end{aligned} \quad (8.16)$$

Substitute X_0 , Y_0 , σ_X and σ_Y to obtain

$$\begin{aligned}
E[s(b, t) | \vec{m}, \vec{c}] &= \frac{c(b)p(b, t) \cdot (B-1)\sigma_n^2 + (m(t) - \sum_{b' \neq b} c(b')p(b', t)) \cdot \sigma_n^2}{(B-1)\sigma_n^2 + \sigma_n^2} \\
&= \frac{B \cdot c(b)p(b, t) - c(b)p(b, t) + m(t) - \sum_{b' \neq b} c(b')p(b', t)}{B} \\
&= c(b)p(b, t) + \frac{m(t) - \sum_{b'} c(b')p(b', t)}{B}
\end{aligned} \tag{8.17}$$

Substitute $s(b, t)$ in equation 8.13 with its expectation, we can obtain the MLEM solution in an iteration form

$$c^{(n+1)}(b) = c^{(n)}(b) + \frac{\sum_t m(t)p(b, t)}{B} - \frac{\sum_b p(b, t) \sum_{b'} c^{(n)}(b')p(b', t)}{B} \tag{8.18}$$

In each iteration, we require $c^{(n)}(b)$ to be positive to make the solution reasonable. Figure 8.1 the convergence of the MLEM method. As seen, it requires lots of iterations to reach acceptable solution, so that MLEM method is expected to be very slow.

8.3 Simulation Result

The induced signal change from one voxel to another is expected to be very small. Therefore, it is required to have low electronic noise to de-convolve the precise distribution of electron clouds. To evaluate how low the noise should be, we made a simulation with 1 keV, 2 keV, 3 keV electronic noise and no electric noise with the recoil electrons at the energy 1243 keV, which is shown in figure 8.3. As can be seen, until 2 keV, the simulated result doesn't differ too much from the one without noise. Therefore fortunately, the electron cloud distribution solution obtained by MLEM method is not very sensitive to the electronic noise of the system.

Figure 8.4 presents a comparison of the calculated electron cloud distribution with the real distribution using simulation data. Theses two plots have similar distribu-

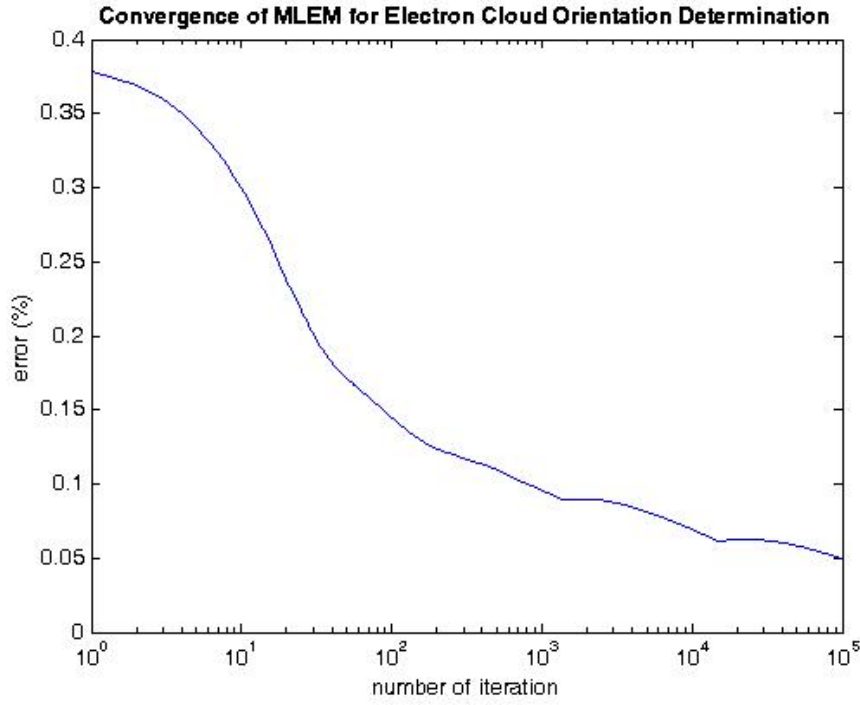


Figure 8.1: The convergence of the MLEM method for electron cloud distribution calculation.

tions. However, it can be clearly seen that the calculation electron cloud distribution is much more diffused. To obtain the emitting angle, the most precise way is to have a measurement which can show distinct initial path of the electron track. Apparently, our electron cloud distribution calculation algorithm won't provide that capability.

Though the measured electron cloud distribution is very vague, the orientation of the distribution may stay the same. To test this hypothesis and check if electron cloud orientation is correlated with the initial electron emitting direction, we compare separation angle between two directions for real electron cloud distribution and calculated distribution using the simulation data. The electron energy is assumed to be 1243 keV and it is emitted isotropically. Figure 8.5 shows the result. The inverse matrix method is also tried and the electron cloud orientation calculated using this method is also plotted in the figure. As can be seen, the calculated electron cloud distribution agree well with the real distribution, indicating the electron cloud distribution calculation algorithm is effective. As a comparison the inverse matrix method

doesn't work. The correlation between the electron cloud orientation and the electron initial emitting direction is noticeable but it isn't strong. For other energies, we investigate the fraction of events whose electron cloud orientation separated less than 30 degree from the initial electron emitting direction and plot the result in figure 8.2. We add a case when the electron cloud orientation is totally irrelevant to the initial electron emitting direction in the plot as a comparison. As shown, this fraction defers very little from the irrelevant case from 0 to 2 MeV, indicating that electron cloud orientation won't be an effective parameter to determine the recoil electron direction. However, though the correlation is weak, it exists. In the future, it can be made a try to investigate how can this weak correlation be used to improve Compton imaging.

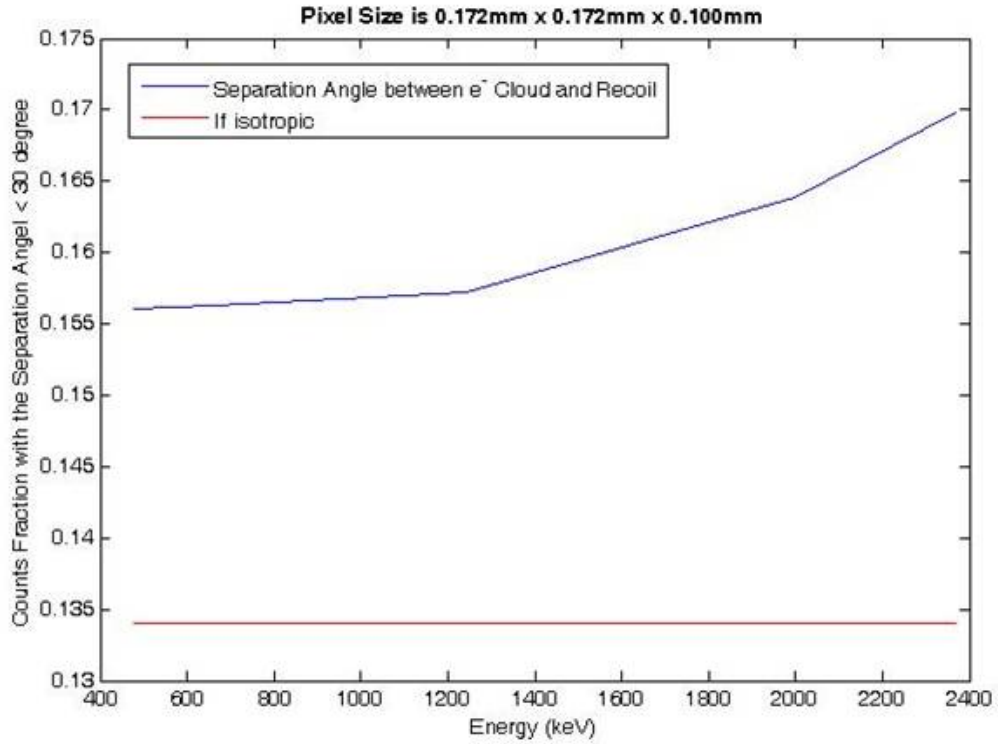


Figure 8.2: fraction of the events whose electron cloud orientation separated less than 30 degree from the electron emitting direction. The isotropic line shows the case when the electron cloud orientation is totally irrelevant to the initial electron emitting direction. Each pixel is divided into 10×10 sub-pixels.

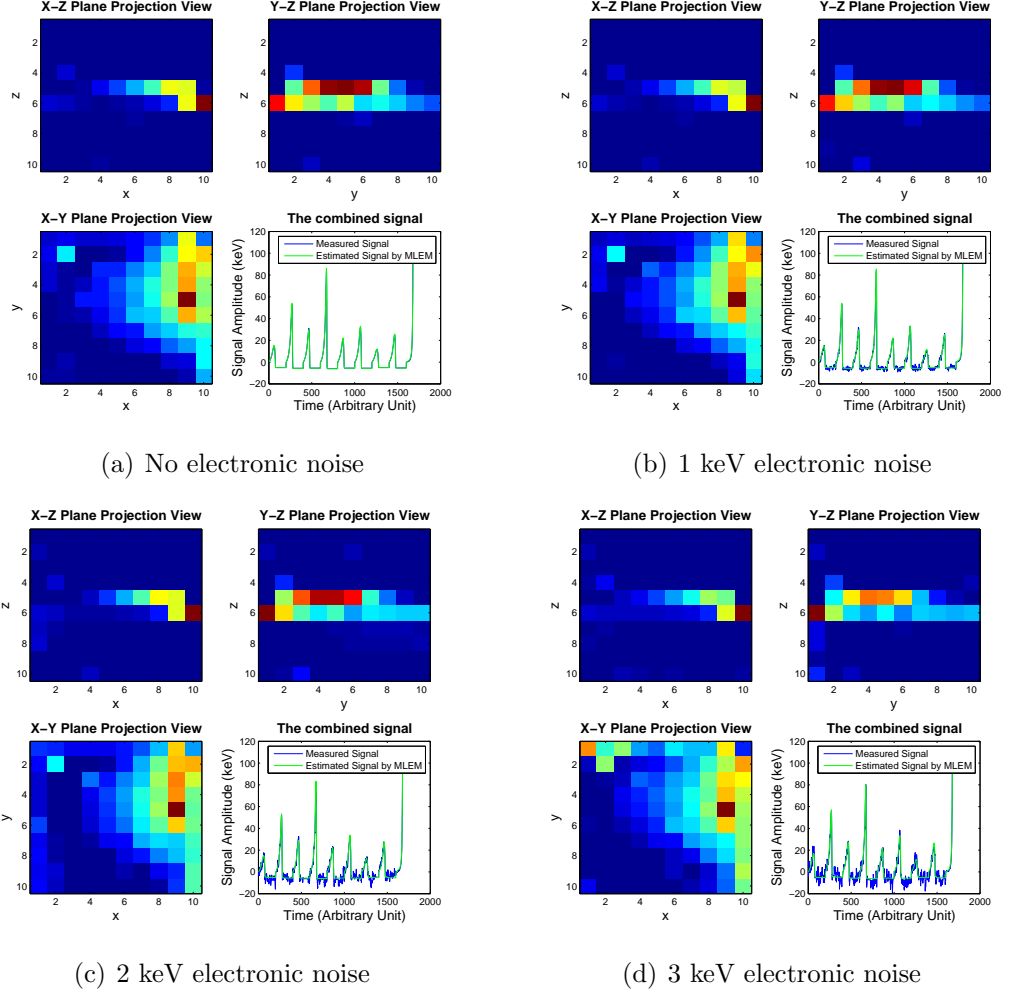
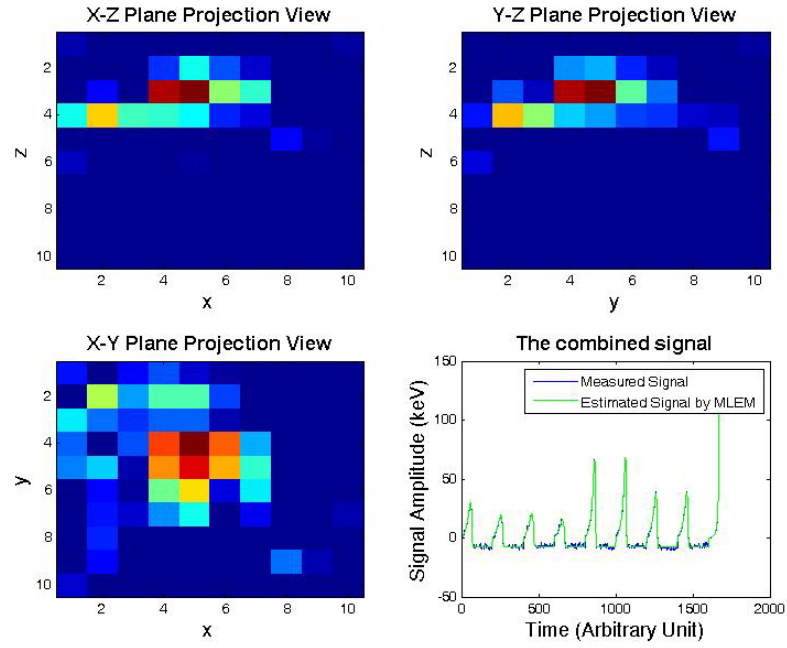
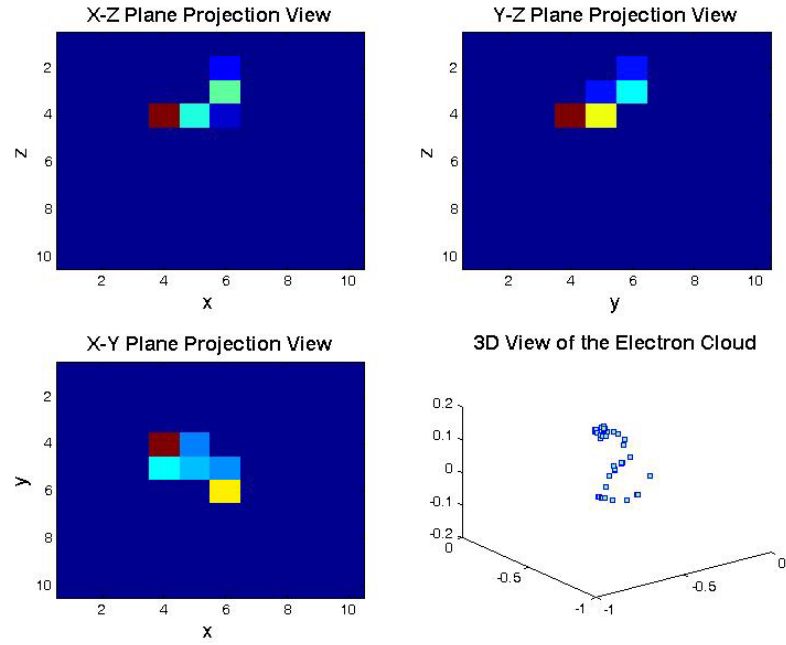


Figure 8.3: The calculated electron cloud distribution using MLEM method with different electronic noise. The electron used in this simulation is 1243 keV. Each pixel is divided into 10×10 sub-pixels. The depth is divided into totally 30 depths. This plot only shows 10 depths where the cloud is located.



(a) The calculation electron cloud distribution



(b) The real electron cloud distribution

Figure 8.4: The simulation result of the electron cloud distribution calculation algorithm using MLEM. The electronic noise is assumed to be 1 keV and the recoil electron energy is 1243 keV.

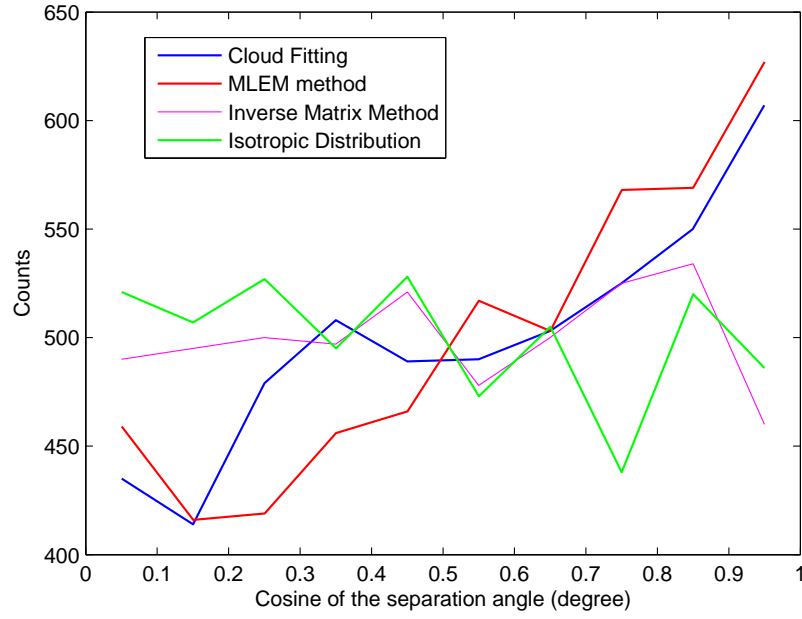


Figure 8.5: The separation angle between the original electron emitting direction and the electron cloud orientation. The electron cloud orientation is obtained from the real electron cloud distribution and the calculated distribution using MLEM method.

8.4 Conclusion

In this chapter, a MLEM algorithm was developed to calculate the electron cloud distribution. The algorithm was found effective. An effort was to make to investigate the possibility of using electron cloud orientation calculated from electron cloud distribution to estimate the initial electron emitting direction. The result shows that electron emitting direction is weakly correlated with the electron cloud orientation.

APPENDICES

APPENDIX A

Model-matched Fitting

For any Gaussian-distributed random variables, with correlation the j.p.d.f. can be generally written as

$$f(\vec{x}) = K \cdot e^{-\vec{x} A \vec{x}'} \quad (\text{A.1})$$

Here, K is normalization factor and \vec{x} is a vector of random variables, A is the covariance matrix. If we express this equation with scalars,

$$f(x_1, x_2, x_3, \dots, x_n) = K \cdot e^{-\sum_{ij} A_{ij} x_i x_j} \quad (\text{A.2})$$

Equation 2.48 we derived in Chapter II says

$$f(x_1, x_2, x_3, \dots, x_n) = \int_{-\infty}^{\infty} K \cdot e^{-\frac{1}{2\sigma_a^2} \left[(x_1 - B)^2 + \sum_{i=2}^n (x_i - B - \sum_{j=1}^{i-1} b_j)^2 + \frac{B^2}{\alpha_B^2} + \sum_{i=1}^{n-1} \frac{b_i^2}{\alpha^2} \right]} dB \cdot db_1 \cdot db_2 \cdot db_3 \dots \cdot db_{n-1} \quad (\text{A.3})$$

Usually the baseline or common mode noise can be determined. Then B term can be removed from the integration, then

$$f(x_1, x_2, x_3, \dots, x_n|B) = \int_{-\infty}^{\infty} K \cdot e^{-\frac{1}{2\sigma_a^2} \left[(x_1-B)^2 + \sum_{i=2}^n (x_i-B - \sum_{j=1}^{i-1} b_j)^2 + \sum_{i=1}^{n-1} \frac{b_i^2}{\alpha^2} \right]} db_1 \cdot db_2 \cdot db_3 \dots \cdot db_{n-1} \quad (\text{A.4})$$

B is a constant now. Let's put $x_i - B$ together to form a serial of new random variables x'_i , then

$$f(x'_1, x'_2, x'_3, \dots, x'_n|B) = \int_{-\infty}^{\infty} K \cdot e^{-\frac{1}{2\sigma_a^2} \left[(x'_1)^2 + \sum_{i=2}^n (x'_i - \sum_{j=1}^{i-1} b_j)^2 + \sum_{i=1}^{n-1} \frac{b_i^2}{\alpha^2} \right]} db_1 \cdot db_2 \cdot db_3 \dots \cdot db_{n-1} \quad (\text{A.5})$$

Then, Comparing Equation A.4 and Equation A.2, A_{ij} can be calculated iteratively by a function written with Matlab, which is provided in this appendix. The input parameters are the number of samples n and the ratio α between the serial noise variance σ_a and the parallel noise variance σ_b .

```
function ef = Calculate_CorrelatedNoise_jpdf_coeff(n, alpha)
ef_d2 = (n:-1:1)';
ef_dd = zeros(n,n);
ef_xx = eye(n,n);

for k=1:n
    for m=1:k-1
        ef_dd(k,m) = n-k+1;
    end
    for m=k:n
```

```

        ef_dd(k,m) = -1;
    end
end
k=n;
for integration=1:n
    c = ef_d2(k)+(1/alpha^2);
    for l=1:k-1
        ef_d2(l) = ef_d2(l) - ef_dd(k,l)^2/c;
    end
    for l=k:n
        ef_xx(l,l) = ef_xx(l,l) - ef_dd(k,l)^2/c;
    end
    for l=k-1:-1:1
        ef_dd(l,1:l-1) = ef_dd(l,1:l-1) ...
            - ef_dd(k,1:l-1)*ef_dd(k,l)/c;
        ef_dd(l,n:-1:k) = ef_dd(l,n:-1:k) ...
            - ef_dd(k,n:-1:k)*ef_dd(k,l)/c;
    end
    for l=k+1:n
        ef_xx(l, k:l-1) = ef_xx(l, k:l-1)...
            - ef_dd(k, k:l-1) * ef_dd(k,l)/c;
        ef_xx(k:l-1, l) = ef_xx(k:l-1, l)...
            - (ef_dd(k, k:l-1) * ef_dd(k,l))'/c;
    end
    k=k-1;
end

```

```
ef = ef_xx;
```

APPENDIX B

Detector Symbols

Detector	Material	Fabricated By	Cross Sec- tion (mm ²)	Thickness (mm)	Anode Grid
3E2	CdZnTe	eV Product	15 × 15	10	Yes
4E3	CdZnTe	eV Product	20 × 20	15	Yes
1C37	HgI ₂	Constellation	20 × 20	10	No ^a
4R169	CdZnTe	Redlen	20 × 20	15	Yes

^aThis detector only a guard ring surrounding all pixels

BIBLIOGRAPHY

BIBLIOGRAPHY

- [1] M. Amman, J.S. Lee, and P.N. Luke. Temperature study of CdZnTe coplanar-grid detectors. *IEEE Trans. on Nucl. Sci.*, 53(5):3035–3040, 2006.
- [2] G. Bale, A. Holland, P. Seller, and B. Lowe. Cooled CdZnTe detectors for X-ray astronomy. *Nucl. Instr. and Meth. A*, 436:150–154, 1999.
- [3] L. Bardelli and G. Poggi. Digital-sampling systems in high-resolution and wide dynamic-range energy measurements: Finite time window, baseline effects, and experimental tests. *Nucl. Instr. and Meth. A*, 560:524–538, 2006.
- [4] H. H. Barrett, J. D. Eskin, and H. B. Barber. Charge transport in arrays of semiconductor gamma-ray detectors. *Phys. Rev. Lett.*, 75:156–159, Jul 1995.
- [5] M. Bertolaccini, C. Bussolati, and E. Gatti. On the problem of optimum signal to noise ratio in amplitude measurements. *Nucl. Instr. and Meth.*, 41(1):173, 1966.
- [6] G. Bertuccio and S. Caccia. Noise minimization of mosfet input charge amplifiers based on $\delta\mu$ and δn models. *IEEE Trans. on Nucl. Sci.*, 56(3):1511–1519, 2009.
- [7] M. Burks, E. Jordan, E. Hull, L. Mihailescu, and K. Vetter. Signal interpolation in germanium detectors for improved 3-D position resolution. In *Nuclear Science Symposium Conference Record (NSS/MIC), 2004 IEEE*, pages 309–394, Rome, Italy, October 2004.
- [8] J. F. Butler, C. L. Lingren, and F. P. Doty. $\text{Cd}_{1-x}\text{Zn}_x\text{Te}$ gamma ray detectors. *IEEE Tran. On Nucl. Sci.*, 39(4):605–609, 1992.
- [9] Z. Y. Change and W. M. Sansen. *Low-noise wide-band amplifiers in bipolar and CMOS technologies*. Kluwer Academic Publishers, Norwell, Massachusetts 02061 USA, 1991.
- [10] P. Dutta and P. M. Horn. Low-frequency fluctuations in solids: $1/f$ noise. *Rev. of Mod. Phys.*, 53(3):497–516, 1981.
- [11] L.A. Hamel, O. Tousignant, M. Couillard, J.F. Courville, V.T. Jordanov, J.R. Macri, K. Larson, M. Mayer, M.L. McConnell, and J.M. Ryan. An imaging CdZnTe detector with coplanar orthogonal anode strips. In *Semiconductors for Room-Temperature Radiation Detector Applications II*, volume 487 of *Materials*

- Research Society Symposium Proceedings*, pages 211–216, Warrendale, PA, USA, 1997.
- [12] Z. He. Review of the Shockley-Ramo theorem and its application in semiconductor gamma-ray detectors. *Nucl. Instr. and Meth. A*, 463:250–267, 2001.
 - [13] Z. He, G.F. Knoll, D.K. Wehe, and J. Miyamoto. Position-sensitive single carrier CdZnTe detectors. *Nucl. Instr. and Meth. A*, 388:180–185, 1997.
 - [14] Z. He, W. Li, G. F. Knoll, D. K. Wehe, J. Berry, and C. M. Stahle. 3-d position sensitive cdznte gamma-ray spectrometers. *Nucl. Instr. and Meth. A*, 422:173–178, 1999.
 - [15] Z. He, W. Li, G.F. Knoll, D.K. Wehe, and C.M. Stahle. Measurement of material uniformity using 3-d position sensitive CdZnTe gamma-ray spectrometers. *Nucl. Instr. and Meth. A*, 441:459–467, 1999.
 - [16] Z. He and B. W. Sturm. Characteristics of depth-sensing coplanar grid CdZnTe detectors. *Nucl. Instr. and Meth. A*, 554:291–299, 2005.
 - [17] H.H.Barrett, J.D.Eskin, and H.B.Barber. Charge transport in arrays of semiconductor gamma-ray detectors. *Phys. Rev. Lett.*, 75(1):156–159, 1995.
 - [18] K. Hitomi, T. Tada, S.Y. Kim, Y. Wu, T. Tanaka, T. Shoji, H. Yamazaki, and K. Ishii. Recent development of TlBr gamma-ray detectors. *IEEE Tran. On Nucl. Sci.*, 58(4):1987–1991, 2011.
 - [19] Paul Horowitz and Winfield Hill. *The Art of Electronics, 2nd edition*. Cambridge (UK): Cambridge University Press, 1989.
 - [20] J. Jakubek and J. Uher. Fast neutron detector based on TimePix pixel device with micrometer spatial resolution. In *Nuclear Science Symposium Conference Record (NSS/MIC), 2009 IEEE*, pages 1113–1116, Orlando, FL, USA, October 2009.
 - [21] J. B. Johnson. Thermal agitation of electricity in conductors. *Phys. Rev.*, 32(1):97–109, 1928.
 - [22] S.J. Kaye, W.R. Kaye, and Z. He. Experimental demonstration of coded aperture imaging using thick 3D-position-sensitive CdZnTe detectors. In *Nuclear Science Symposium Conference Record (NSS/MIC), 2009 IEEE*, pages 1902–1906, Orlando, FL, USA, October 2009.
 - [23] W. Kaye, Y.A. Boucher, F. Zhang, and Z. He. Calibration and operation of the polaris 18-detector CdZnTe array. In *Nuclear Science Symposium Conference Record (NSS/MIC), 2010 IEEE*, pages 3821–3824, Knoxville, TN, USA, October 2010.

- [24] Willy Kaye. *Energy and Position Reconstruction in Pixelated CdZnTe Detectors*. PhD thesis, University of Michigan, 2012.
- [25] J. C. Kim, S. E. Anderson, W. Kaye, S. J. Kaye, Y. Zhu, F. Zhang, and Z. He. Study on effect of charge sharing events in common-grid pixelated CdZnTe detectors. In *Nuclear Science Symposium Conference Record (NSS/MIC), 2009 IEEE*, pages 1640–1646, Orlando, FL, USA, October 2009.
- [26] G. F. Knoll. *Radiation Detection and Measurement, Third Edition*. John Wiley & Sons, Inc., Hoboken, NJ, 1999.
- [27] P.N. Luke. Unipolar charge sensing with coplanar electrodes-application to semiconductor detectors. *IEEE Trans. on Nucl. Sci.*, 42(4):207–213, 1995.
- [28] P.N. Luke and M. Amman. Room-temperature replacement for Ge detectors-are we there yet? *IEEE Trans. on Nucl. Sci.*, 54(4):834–842, 2007.
- [29] J.R. Macri, B.A. Apotovsky, J.F. Butler, M.L. Cherry, B.K. Dann, A. Drake, F.P. Doty, T.G. Guzik, K. Larson, M. Mayer, M.L. McConnell, and J.M. Ryan. Development of an orthogonal-stripe CdZnTe gamma radiation imaging spectrometer. In *Nuclear Science Symposium Conference Record (NSS/MIC), 1996 IEEE*, pages 1458–1462, San Francisco, CA, USA, October 1996.
- [30] D.G. Marks, H.B. Barber, H.H. Barrett, J. Tueller, and J.M. Woolfenden. Improving performance of a CdZnTe imaging array by mapping the detector with gamma rays. *Nucl. Instr. and Meth.*, 428(1):102–112, 1999.
- [31] D. S. McGregor and H. Hermon. Room-temperature compound semiconductor radiation detectors. *Nucl. Instr. and Meth. A*, 395:101–124, 1997.
- [32] T. Narita, J. E. Grindlay, J. Hong, and F. C. Niestemski. Anode readout for pixellated CZT detector. In *Proceedings SPIE*, volume 5165, pages 542–547, 2004.
- [33] A. Niemela and H. Sipila. Evaluation of CdZnTe detractors for soft-X-ray applications. *IEEE Trans. on Nucl. Sci.*, 41(4):1054–1057, 1994.
- [34] H. Nyquist. Certain topics in telegraph transmission theory. *Trans. AIEE*, 47:617–644, 1928.
- [35] H. Nyquist. Thermal agitation of electric charge in conductors. *Phys. Rev.*, 32(1):110–113, 1928.
- [36] Alan V. Oppenheim and Ronald W. Schaffer. *Discrete-Time Signal Processing, 2nd Edition*. Prentice Hall, Upper Saddle River, NJ, 1999.
- [37] A. Owens, M. Bavdaz, H. Andersson, T. Gagliardi, M. Krumrey, S. Nenonen, A. Peacock, I. Taylor, and L. Troger. The X-ray response of CdZnTe. *Nucl. Instr. and Meth. A*, 484:242–250, 2002.

- [38] B. E. Patt, J.S. Iwanczyk, G. Vilkelis, and Y.J. Wang. New gamma-ray detector structures for electron only charge carrier collection utilizing high-Z compound semiconductors. *Nucl. Instr. and Meth. A*, 380:276–281, 1996.
- [39] A. Pullia and S. Riboldi. Time-domain simulation of electronic noises. *IEEE Trans. on Nucl. Sci.*, 51(4):1817, 2004.
- [40] V. Radeka. Least-square-error amplitude measurement of pulse signals in presence of noise. *Nucl. Instr. and Meth.*, 52(1):86, 1967.
- [41] C. E. Shannon. Communication in the presence of noise. *Proc. Institute of Radio Engineers*, 37(1):10–21, 1949.
- [42] L. A. Shepp and Y. Vardi. Maximum likelihood reconstruction for emission tomography. *IEEE Tran. on Med. Img.*, MI-1(2):113–122, 1982.
- [43] P. Siffert. Cadmium telluride detectors and applications. *MRS Proc.*, 16:87–114, 1983.
- [44] R. Sudharsanan, C.C. Stenstrom, P. Bennett, and G.D. Vakerlis. Performance of P-I-N CdZnTe radiation detectors and their unique advantages. In *Semiconductors for Room-Temperature Radiation Detector Applications II*, volume 487 of *Materials Research Society Symposium Proceedings*, pages 245–255, Warrendale, PA, USA, 1997.
- [45] J. S. Vickersa and S. Chakrabarti. Silicon-anode detector with integrated electronics for microchannel-plate imaging detectors. *Rev. of Sci. Instr.*, 70(7):2912–2916, 1999.
- [46] S. M. Vincent, P. H. Regan, K. E. Owen, C. J. Pearson, and A. S. Clough. In-beam performance of CdZnTe detectors for proton and alpha-particle measurement. *Nucl. Instr. and Meth. A*, 483(3):758–763, 2002.
- [47] W. K. Warburton. An approach to sub-pixel spatial resolution in room temperature X-ray detector arrays with good energy resolution. *Mat. Res. Symp. Proc.*, 487:531–535, 1998.
- [48] C. S. Williams, W. P. Baker, L. W. Burggraf, P. E. Adamson, and J. C. Petrosky. Toward simultaneous 2D ACAR and 2D DBAR: Sub-pixel spatial characterization of a segmented HPGe detector using transient charges. *IEEE Trans. on Nucl. Sci.*, 57(2):860–869, 2010.
- [49] D. Xu, Z. He, C. E. Lehner, and F. Zhang. 4-pi compton imaging with single 3D position sensitive CdZnTe detector. *Proceedings SPIE*, 5540:144–155, 2004.
- [50] F. Zhang. *Events reconstruction in 3-D position sensitive CdZnTe gamma-ray spectrometers*. PhD thesis, University of Michigan, 2005.

- [51] F. Zhang, Z. He, and C. E. Seifert. Prototype three-dimensional position sensitive CdZnTe detector array. *IEEE Tran. On Nucl. Sci.*, 54(4):843–848, 2007.
- [52] F. Zhang, W. R. Kaye, and Z. He. Performance of 3-D position sensitive CdZnTe detectors for gamma-ray energies above 1 MeV. In *Nuclear Science Symposium Conference Record (NSS/MIC), 2009 IEEE*, pages 2012–2016, Orlando, FL, USA, October 2009.